

Spring 5-2016

Fluidic Jet Turbulence Generators for Deflagration to Detonation Transition in Pulsed Detonation Combustors

Jarrett E. Lowe
Embry-Riddle Aeronautical University

Follow this and additional works at: <https://commons.erau.edu/edt>



Part of the [Aerodynamics and Fluid Mechanics Commons](#)

Scholarly Commons Citation

Lowe, Jarrett E., "Fluidic Jet Turbulence Generators for Deflagration to Detonation Transition in Pulsed Detonation Combustors" (2016). *Doctoral Dissertations and Master's Theses*. 224.
<https://commons.erau.edu/edt/224>

This Thesis - Open Access is brought to you for free and open access by Scholarly Commons. It has been accepted for inclusion in Doctoral Dissertations and Master's Theses by an authorized administrator of Scholarly Commons. For more information, please contact commons@erau.edu.

**FLUIDIC JET TURBULENCE GENERATORS FOR DEFLAGRATION TO DETONATION
TRANSITION IN PULSED DETONATION COMBUSTORS**

A Thesis

Submitted to the Faculty

Of

Embry-Riddle Aeronautical University

by

Jarrett E. Lowe

In Partial Fulfillment of the

Requirements for the Degree

of

Master of Science in Aerospace Engineering

May 2016

Embry-Riddle Aeronautical University

Daytona Beach, Florida

**FLUIDIC JET TURBULENCE GENERATORS FOR DEFLAGRATION TO DETONATION
TRANSITION IN PULSED DETONATION COMBUSTORS**

by

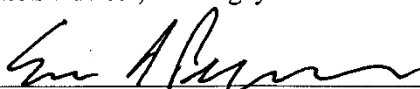
Jarrett E. Lowe

A Thesis prepared under the direction of the candidates' committee chairman, Dr. Magdy S. Attia, Department of Aerospace Engineering, and has been approved by the members of the thesis committee. It was submitted to the school of Graduate Studies and Research and was accepted in partial fulfillment of the requirements for the degree of Master of Science in Aerospace Engineering.

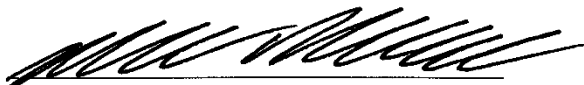
THESIS COMMITTEE



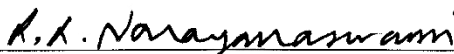
Thesis Advisor, Dr. Magdy S. Attia



Member, Dr. Eric R. Perrell



Member, Dr. Mark A. Ricklick



Member, Dr. Lakshmanan L. Narayanaswami



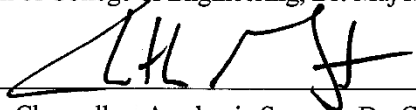
Department Chair, Dr. Anastasios Lyrintzis
or Graduate Program Coordinator, Dr. Eric Perrell

24 May 2016
Date



Dean of College of Engineering, Dr. Maj Mirmirani

6/2/2016
Date



Vice Chancellor, Academic Support, Dr. Christopher Grant

6/14/16
Date

Acknowledgements

I would sincerely like to thank Dr. Magdy Attia for his guidance and support through the process and my committee members for their feedback and questioning pointing me in the right direction for my investigation.

A special thanks goes out to my lab mates, Christopher Tate, Nicole Gagnon, Alexander Roosendaal, Daniel Port and Darrell Stevens for their help, feedback, and assistance throughout the project as well as Bill Russo in the machine shop.

Finally, my family and friends back home giving me support throughout the past year and a half.

Thank you all very much, it has been deeply appreciated.

Sincerely

Jarrett E. Lowe

Table of Contents

1	Motivation	1
2	Theory and Background	3
2.1	Deflagration vs. Detonation	3
2.2	Pulse Detonation Engine Cycle and Description	5
2.3	Potential Benefits and Application Considerations.....	7
2.4	Deflagration to Detonation Transition	8
2.5	The Fluidic Technique	10
3	Experiment and Design	14
3.1	Objectives.....	14
3.2	Experimental Plan and Structure.....	15
3.2.1	Phase #1: Physical Obstacle Configurations.....	15
3.2.2	Phase #2: Single Orifice.....	15
3.2.3	Phase #3: JICF Turbulence Generator	15
3.2.4	Phase #4: Bluff body and JICF	16
3.3	Pulse Detonation Combustor Design	17
3.3.1	Fuel Injection Design.....	18
3.3.2	Jet In Cross Flow	27
3.3.3	Electrical System	34
3.3.4	Data Acquisition	35
3.3.5	Bulk Air Delivery	39
3.3.6	Venturi Flowmeter	41
4	Results and Discussion	51
4.1	Phase 1: Physical Obstacle Testing	51
4.1.1	Full Stack Representative Raw Data.....	52
4.1.2	Full Stack Condensed Information	53
4.1.3	General Electric Trial Reproduction.....	63
4.2	Phase 2: Single Orifice Tests	64
4.2.1	Representative Raw Data	65
4.2.2	Equivalence 2 Compiled Data	66
4.3	Phase 3: JICF Testing.....	71
4.3.1	Representative Raw Data	71

4.3.2	JICF Sweep Condensed Data.....	74
4.3.3	Effect of varying jet strength	79
4.3.4	Equivalence Ratio Influence	82
4.3.5	Bulk Flow Effects	84
4.4	Phase 4: Bluff Body and JICF.....	87
4.4.1	Representative Raw Data	87
4.4.2	Hybrid JICF Sweep.....	88
4.5	Comparisons of Selected Physical and Fluidic Cases	93
4.6	JICF Orientation Summary	95
5	Conclusion	98
6	Future Work.....	99
6.1	Test Rig Improvements	99
6.2	Suggested Areas of Investigation.....	101
6.3	Fluid Jet Technique	101
7	References	102
A.	Hardware Information.....	1
A.1	PX329	1
A.2	PCB 111A24.....	2
A.3	PCB 482C05	3
A.4	10Vdc Precision Power Supply	4
B.	Condensed Test Information.....	5
B.1	Phase #1	5
B.2	Phase #2	5
B.3	Phase #3	6
B.4	Phase #4	9
C.	Part Drawings.....	11

List of Figures

Figure 1 Thermodynamic Cycles of the Brayton and Humphrey ³²	4
Figure 2 Valveless PDE using a fluid diode ¹⁶	6
Figure 3 Shchelkin Spiral after testing PDE Mark 1 for a few seconds ¹⁴ and Naval Postgraduate Swept Ramp Obstacle ⁶	8
Figure 4 Detonation Wave Structure ¹⁴	10
Figure 5 Effect of Varying Flame Equivalence Ratio on Obstacle Interaction. Left Fluidic MR 0.3 Φ 0.7, MR 0.3 Φ 1.0, Right Physical Blockage BR 0.2 Φ 0.7 and BR 0.2 Φ 1.0 ²⁴	11
Figure 6 NPGS Swept Ramp Vortices ⁵	13
Figure 7 Bluff Body 1.250" Throat.....	16
Figure 8 PDE Test Section.....	17
Figure 9 Dimensioned Test Section, Axial Positions in meters.....	18
Figure 10 Fuel Injection Manifold.....	21
Figure 11 Fuel Manifold Plenum Chamber with $4x \alpha 22.5^\circ \beta 90^\circ$	22
Figure 12 Finalized Fuel Injection Setup.....	23
Figure 13 Fuel Injection Calibration.....	23
Figure 14 Fuel Injection Calibration of Pressure vs. Volumetric Flow Rate.....	24
Figure 15 Fuel Manifold Calibration Curves.....	25
Figure 16 Jet Orientation Definitions, $\alpha 25^\circ, \beta 45^\circ$	27
Figure 17 JICF Clamp on Air Manifold in the aft position	27
Figure 18 Jet Selection with Clamp-on Manifold.....	28
Figure 19 JICF Air Supply.....	29
Figure 20 JICF Supply Pressure Response	30
Figure 21 JICF Mass Flow Rate Calibration Curve	32
Figure 22 JICF Flow Rate Calibrations	33
Figure 23 National Instruments USB-6351 DAQ and accompanying busses and power distribution	34
Figure 24 Test Rig Analogue Inputs, Dynamic Pressure, Ion and Static Pressure.....	35
Figure 25 JICF20 at 60psi mass flow 0.0764 kg/s and an average Φ of 1.25, 4xPort 22.5° Injection	38
Figure 26 Bulk Air Supply.....	39
Figure 27 Porous Pressure Surface	40
Figure 28 Venturi Flowmeter Installed.....	41
Figure 29 Venturi Flowmeter at 0.156 kg/s mass flow rate contour plots.....	43
Figure 30 Venturi Flowmeter 0.156 kg/s Y plus	44
Figure 31 Venturi Flowmeter 0.156 kg/s wall shear stress.....	45
Figure 32 Unstructured Mesh with a mass flow rate of 0.052 kg/s examining the pressure and velocity at the throat tap location.....	46

Figure 33 Venturi Flowmeter Inlet Pressure Recovery	49
Figure 34 Venturi Flowmeter mass flow rate predictions	50
Figure 35 Phase 1 Physical DDT Stacks, Cross Section of 0.0 is wall and 0.5 is centerline	51
Figure 36 Representative Raw Data of Stacks 1, 4 at station #7	52
Figure 37 Nondimensional Velocity of Physical DDT Stacks $M_{air} 0.0539 \text{ kg/s}$	53
Figure 38 Nondimensional Pressure of Physical DDT Stacks $M_{air} 0.0539 \text{ kg/s}$	54
Figure 39 Flame Detection Time of Physical DDT Stacks 0.0539 kg/s	55
Figure 40 Flame Detection Improvement over Baseline, Physical DDT Stacks $M_{air} 0.0539 \text{ kg/s}$	56
Figure 41 Post Pressure of Physical DDT Stacks 0.0539 kg/s	58
Figure 42 Refill Method Comparisons, Post Shock Pressure	59
Figure 43 Refill Method Comparisons, Wave Pressure	60
Figure 44 Refill Method Comparisons, Flame Velocity	61
Figure 45 DDT Success for Physical DDT Stacks	62
Figure 46 Phase 2 Testing Configurations	64
Figure 47 Raw Data of Combined BR03 at $\Phi 1.2516$ Mass Air 0.0539 kg/s	65
Figure 48 Ion Velocity of Single and Combined BRs at $\Phi 1.25$ Mass Air 0.0543 kg/s	66
Figure 49 Max Pressure of Single and Combined BRs at $\Phi 1.2516$ Mass Air 0.0543 kg/s	67
Figure 50 Flame Detection Time of Single and Combined BRs at $\Phi 1.2516$ Mass Air 0.0543 kg/s	68
Figure 51 Improvement of Flame Detection Time of Single and Combined BRs at $\Phi 1.2516$ Mass Air 0.0543 kg/s . Referenced to BR00	69
Figure 52 JICF03 ($\alpha 25^\circ \beta 135^\circ$) $M_{air} 0.054 \text{ kg/s}$ $\Phi 1.2808 0.9877$ Pressure Sweep	71
Figure 53 JICF03 ($\alpha 25^\circ \beta 135^\circ$) $M_{air} 0.0539 \text{ kg/s}$ $\Phi 1.2808 0.9886$ Paired 567	72
Figure 54 JICF03 ($\alpha 25^\circ \beta 135^\circ$) $M_{air} 0.0539 \text{ kg/s}$ $\Phi 1.2808 0.9886$	73
Figure 55 Ion Velocity JICF Sweep, $\Phi 1.28$, MR 3.855	74
Figure 56 Max Pressure JICF Sweep, $\Phi 1.28$, MR 3.855	75
Figure 57 Pressure Increase over Baseline JICF Sweep, $\Phi 1.28$, MR 3.855	76
Figure 58 Ion Detection Time JICF Sweep, $M_{air} 0.0539 \text{ kg/s}$, $\Phi 1.28$, MR 3.855	77
Figure 59 Ion Detection Time Improvement JICF Sweep, $M_{air} 0.0539 \text{ kg/s}$, $\Phi 1.28$, MR 3.855	78
Figure 60 Visualization of Instantaneous flow field of a Normal JICF, MR 3.3, Re 2100, Bulk Flow M 0.2 ³¹	78
Figure 61 Ion Velocity JICF20 ($\alpha 25^\circ \beta 135^\circ$ and 180°) MR Sweep, initial $\Phi 0.98$	79
Figure 62 Max Pressure JICF20 ($\alpha 25^\circ \beta 180^\circ$) MR Sweep, initial $\Phi 0.98$	80
Figure 63 Ion Detection Time JICF20 and 30 ($\alpha 25^\circ \beta 180^\circ 135^\circ$) MR Sweep, initial $\Phi 0.98$	81
Figure 64 JICF 02, 03, 04, 20, 30, 40 $M_{air} 0.0539 \text{ kg/s}$ MR3.855 $\Phi 1.00$ and 1.28	82
Figure 65 JICF 02, 03, 04, 20, 30, 40 $M_{air} 0.0539 \text{ kg/s}$ MR3.855 $\Phi 1.00$ and 1.28	83
Figure 66 Effect of Flow Rate on JICF Flame Velocity	84
Figure 67 Effect of Flow rate on JICF Max Pressure	85
Figure 68 Bulk flow Variation on Blowdown Time	86

Figure 69 Hybrid Trial JICF03 (α 25° β 135°) M_{air} 0.0539kg/s MR3.85 Φ 1.307 1.008 Station 567 paired.....	87
Figure 70 Hybrid Trial M_{air} 0.0539kg/s MR3.85 Φ 1.28 Flame Velocity	88
Figure 71 Hybrid Max Pressure M_{air} 0.0539kg/s MR3.85 Φ 1.28.....	89
Figure 72 Hybrid Trial M_{air} 0.0539kg/s Φ 1.28 Pressure Improvement over baseline.....	90
Figure 73 Hybrid Trial M_{air} 0.0539kg/s Φ 1.28 Ion Blowdown Time.....	91
Figure 74 Hybrid Trial M_{air} 0.0539kg/s 1.28 Ion Blowdown Improvement	92
Figure 75 Pressure and Ion Data from 4 comparable configurations in station 7, velocities from stations 5, 6 and 7.....	93
Figure 76 JICF Summarized Plots of Improvements by X/D 21.4, M_{air} 0.0539 kg/	95
Figure 77 Hybrid Summarized Plots of Improvements by X/D 21.4, M_{air} 0.0539 kg/s	96
Figure 78 AD587 10VDC Precision Power Supply, Information provided by Analogue Devices 4	

List of Tables

Table 1. Detonation vs. Deflagration properties products/reactant ^{8,9}	4
<i>Table 2 Fuel Manifold Curve Fit Constants</i>	26
Table 3 4 Port Fuel Injection Information	26
Table 4 JICF Location and Orientation	28
Table 5 Scan patterns and sample rate per configuration	35
Table 6 DDT Stack Pressure Loss	57
Table 7 Physical Differences between GE and Reproduction Trial	63
Table 8 Phase 2 Filling Losses for Each Configuration	70
Table 9 PX329 Factory Calibration Information	1
Table 10 DDT Configurations M_{air} 0.0539, RE 25455 fill air	5
Table 11 Phase 2 Orifice M_{air} 0.0539 kg/s	5
Table 12 Phase 2 Orifice M_{air} 0.0763 kg/s	6
Table 13 JICF M_{air} 0.0539 kg/s, Re 25400 fill air	6
Table 14 JICF M_{air} 0.0764 kg/s, Re 35756 fill air	7
Table 15 JICF M_{air} 0.0539 kg/s, Re 25400 fill air	8
Table 16 JICF M_{air} 0.0764 kg/s, Re 35756 fill air	8
Table 17 Hybrid M_{air} 0.0539 kg/s, Re 25344 fill air	9

Nomenclature

A_j	=	Cross section area of j
a_i	=	Speed of sound of gas i
BR	=	Blockage Ratio
$C_{\#\#}$	=	Constant for calibration
CJ	=	Upper Chapman-Jouguet point
C_p	=	Constant pressure specific heat capacity kJ/kg-K
CFM	=	Cubic Feet per Minute
DDT	=	Deflagration to Detonation
JICF	=	Jet in Crossflow
NPT	=	National Pipe Taper thread, additional character M = Male, F = Female
MR	=	Momentum Ratio, used for Momentum of Jet over Bulk Flow Momentum
M_{CJ}	=	Chapman-Jouguet state Mach number, $V_{CJ}/a_{\text{reactants}}$
Re	=	Reynolds Number
SFC	=	Specific Fuel Consumption
SHCS	=	Socket Head Cap Screw
x/D	=	Non-Dimensional Axial Distance From Ignition Location
\dot{m}	=	mass flow rate
P_i	=	Pressure of item i
q	=	Heat addition kJ/kg
\tilde{q}	=	Nondimensional heat addition, $q/C_p T$
T_i	=	Temperature in Kelvin of i
v_i	=	Velocity in m/s of i
α	=	Angle of jet in degrees from normal
β	=	Yaw of jet in degrees referenced to downstream flow
γ	=	Ratio of Specific Heats
η	=	Thermal Efficiency
ρ_i	=	Density in kg/m ³ of i
Φ	=	Equivalence Ratio, 1.00 Stoichiometric

Abstract

The goal of this study is to establish the dominant flow structure required to effectively accelerate the turbulent deflagration flame front to detonation velocity in the shortest possible distance while using a single Jet in Cross Flow (JICF). Jets in crossflow, depending on orientation and momentum ratio, can induce two types of flow structures that propagate downstream; vortex filaments and turbulent eddies. Vortex flow structures are coherent rotating columns that can persist for a considerable distance before diffusing. Turbulent eddies are characterized as random fluctuations in flow velocity or small pockets of rotation. The test rig used for this study consists of a valveless pulse detonation combustor operating at near-ambient conditions supplying air at a rate of (0.05-0.1) kg/s and equivalence ratios of 1.0 to 1.3 using Ethylene fuel. Experimental studies comprised of four phases of testing: full obstacle configurations, single orifice, fluidic jet, and hybrid. Overall, the initial fluidic tests reveal the primary effect is an increase in peak pressure (13%-120%) and a decrease in the ion detection time by up to 19% favoring upward facing jets while velocity displayed no discernable change from the baseline. A study was also conducted with physical transition geometry comparing both valve and valveless configurations. Findings indicate frequent obstacles leading the DDT section both improves flame acceleration and mitigate the backflow due to a porous thrust surface with insufficient supply pressures and furthermore verifies excessive obstacles are detrimental towards later flame acceleration and transition to detonation.

1 Motivation

Pulse detonation if achieved successfully can lead to significant efficiency improvements over the Brayton cycle in air breathing engines. However, several difficulties exist in achieving detonations, refreshing reactants as well as thermal management.

The method of using fluid impinging jets and air slots in recent studies has displayed admirable features in generating turbulence, which accelerates the flame front significantly compared to using physical blockages¹⁻⁴. It can also be noted, that the drag penalty of using physical turbulence generators is not insignificant and can negate the benefit of the pressure rise combustion in hybrid engines¹⁻³. In recent studies conducted by the Naval Post Graduate School investigation of low loss swept ramps that promote turbulence and strong stream-wise vortices has displayed its ability to promote DDT^{5,6}. The coherent vortex structure present in the flow tends to fold the flame's contact surface more so than small scale turbulence due to the length scale. It may be of importance to explore this phenomena as a Jet in Crossflow can induce coherent vortices and turbulence with varying levels of intensity⁷.

By using fluidic turbulence generators, such as planar and circumferential slot jets, several benefits exist over their physical orifice counterparts. Increased effectiveness in flame front acceleration⁴, significant reductions in pressure loss due to form drag¹⁻³, improvements in cooling as no physical geometry is present, and the ability to actively adjust operation of the fluid jets.

Previous research has focused on using fluid impingement slots for turbulence generators to accelerate the flame front to a critical value needed to achieve DDT; however, turbulence is not the only mechanism needed for transition. It may be a requirement to use a streamlined obstacle to reflect shocks in order to form a detonation kernel reliably while using air and hydrocarbon fuels. In the most recent studies conducted by McGarry at UCF the research has focused on using

methane air slot injection and correlating the flame front acceleration with turbulence and strain rate using visual studies²⁴. In their findings they have observed the deflagrated flame's acceleration by the fluidic jet in initially static air columns with and without turbulent eddies that increase the energy release rate and turbulence.

The proposed research aimed to establish the dominant flow structure required to accelerate the deflagrated flame in the shortest possible distance using a single JICF as a baseline study.

2 Theory and Background

2.1 Deflagration vs. Detonation

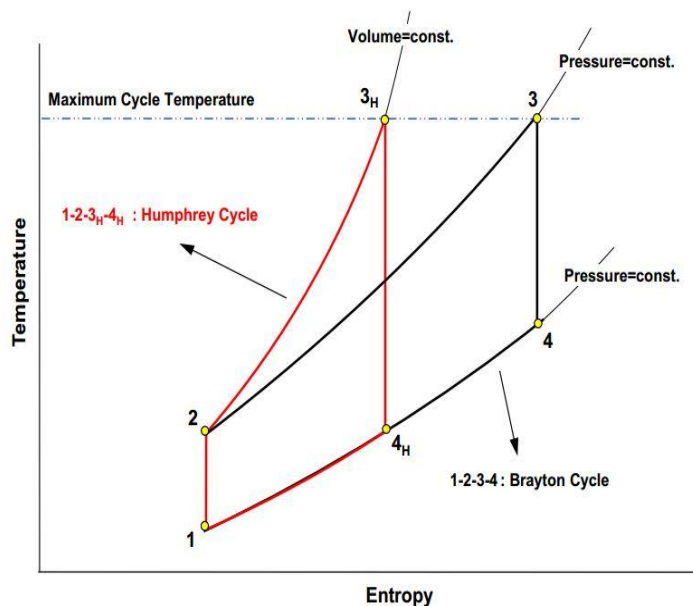
Combustion occurs in two stable modes, Deflagration and Detonation. Deflagration is observed in many engines in current operation. The best examples are those found in boilers, furnaces, automobiles and gas turbine engines where combustion can be approximated as isobaric⁸. The reaction rate of deflagration is driven by the diffusion of radicals, temperature, turbulent mixing, and chemical kinetics⁸. The average flame speed for laminar diffusion burning is on the order of a few meters per second whereas detonations can travel well beyond the speed of sound on the order of thousands of meters per second. The structure of a detonation wave is three dimensional and oscillatory; however, two simplified theories used to estimate the final state of detonation fairly accurately is the CJ Theory and the ZND model⁸⁻¹⁰. Chapman-Jouguet (CJ) theory balances the energy equations to obtain the final state of the products and simplifies the event to an infinitely thin and one dimensional event^{10, 14}. The ZND model solves the Euler Equations and incorporates chemical kinetics. The structure of the ZND model is a strong shock followed by a thin induction region and a thicker chemical reaction region based upon chemical kinetics. The Von Neumann pressure spike is also captured by the ZND model unlike CJ which also predicts the same final state¹⁰⁻¹⁴.

Table 1. Detonation vs. Deflagration properties products/reactant^{8,9}

Usual magnitude of Ratio		
Ratio	Detonation	Deflagration
U_r/C_r^a	5 to 10	0.0001 to 0.03
U_p/u_r	0.4 to 0.7	4 to 16
P_p/P_r	13 to 55	0.98 to 0.976
T_p/T_r	8 to 21	4 to 16
ρ_p/ρ_r	1.4 to 2.6	0.06 to 0.25

C_r^a is the acoustic velocity in the unburned gasses. U_r/C_r is the Mach number of the wave.

The differences between deflagrations and detonations are summarized in table 1. In essence the thermodynamic cycle of detonation is far more efficient than isobaric deflagration. Given the higher efficiency, energy density, and pressure gain; this cycle would significantly improve the performance of many engine architectures such as gas turbine engines⁹.

Figure 1 Thermodynamic Cycles of the Brayton and Humphrey³²

Comparing the thermodynamic cycles of the Brayton and Humphrey in figure 1, the Humphrey cycle produces far less entropy and the burning of the fuel provides an additional pressure gain. The Humphrey cycle is comparable to the actual Pulse Detonation Cycle as it is a quasi-constant volume combustion process. The Brayton cycle consist of compression 1-2, constant pressure heat addition 2-3, and power extraction 3-4. Humphrey cycle consists of Compression 1-2, constant volume combustion with a pressure rise 2-3_H, and power extraction 3_H-4. The ideal thermal efficiencies below for comparison are functions of temperature, fuel heating value, and the ratio of specific heats^{10, 32, 33}.

$$\eta_{Brayton} = 1 - \frac{T_1}{T_2}$$

$$\eta_{Humphrey} = 1 - \gamma \frac{T_1}{T_2} \left[\frac{\frac{T_3^{\frac{1}{\gamma}}}{T_2} - 1}{\frac{T_3}{T_2} - 1} \right] \text{ or more accurately } 1 - \frac{1}{\tilde{q}} \left[\left(1 + \frac{\gamma \tilde{q} T_1}{T_2} \right)^{1/\gamma} - 1 \right]$$

$$\eta_{Ideal PDE} = 1 - \frac{1}{\tilde{q}} \left[\frac{1}{M_{CJ}^2} \left(\frac{1 + \gamma M_{CJ}^2}{\gamma + 1} \right)^{(\gamma+1)/\gamma} - 1 \right]$$

2.2 Pulse Detonation Engine Cycle and Description

Pulse detonation engines operate with a revolving cycle comprised of four general steps: Fill, Combustion, Blowdown, and Purge. During the filling stage fuel and air are brought into the combustion chamber. Combustion is the ignition which creates an expanding flame kernel that fills the diameter of the PDE tube and then accelerates to form a detonation wave consuming the remaining reactants. Blowdown is the expanding products expelling from the combustion chamber and is frequently modelled by the Taylor expansion fan. The fourth stage, Purging, is optional and used primarily to avoid ignition during refreshment of reactants and thermal management.

Typical PDE's rely on valves for the fuel and oxidizer and prevents backflow during combustion and blowdown. Given the goal of achieving higher frequencies mechanical valves have displayed limitations in achieving higher frequency operation in a robust system; Furthermore, challenges of friction, cyclic wear and warping are concerns of sustained deployment²⁸.

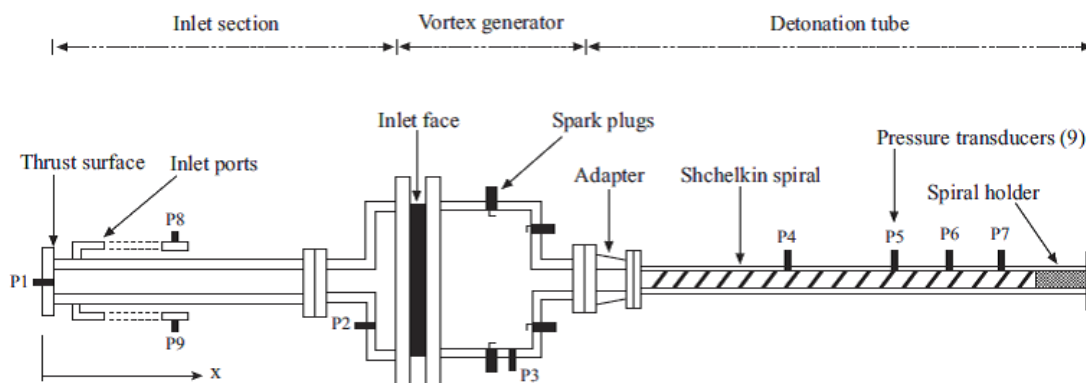


Figure 2 Valveless PDE using a fluid diode¹⁶

Valveless designs incorporate choke points to prevent the pressure waves from propagating upstream or the use of an attenuating “Fluid Diode”. In GE’s multi-tube test rig ensures the total pressure of the air supply is greater than the static pressure during blowdown; however, they have experienced problems with pressure wave interference during filling¹⁹. Other studies have focused on high frequency fuel delivery by using orifices directly exposed to the chamber. The size, shape, and supply pressure dictates the response to the pressure waves inside the PDE tube and have shown their ability to cut off fuel flow without active control¹¹.

The impact of combustion in moving mixtures studied by several including GE indicates several important trends that deviate from static mixtures¹². Except for cases below 15 m/s in a 2” cross-section, the location of DDT is not sensitive to velocity while the blowdown and combustion time displays strong nonlinear trend as fill velocity increases¹². The study also found that 70% of

the time and 20% of the length to achieve DDT is a function of the initial flame kernel growth to fill the diameter and could potentially be the rate limiting process of these engines¹².

2.3 Potential Benefits and Application Considerations

The potential benefit of using pulse detonation instead of isobaric combustion in gas turbine engines shows a theoretical SFC reduction of 2 to 8% depending on pressure ratio and thermal management techniques^{13, 19}. The other potential benefit is the ability of the detonation cycle to burn lean fuels that would normally not combust. This could in fact reduce emissions further in commercial engines, decrease the theoretical SFC as well as create another operating parameter for control¹³.

The thermal load considerations for useful pulse detonation engines and combustors in a hybrid arrangement must be addressed. In analytical studies conducted by Paxson and Perkins, thermal loading must be controlled and managed to avoid mechanical failure due to the stresses and the thermal limits of materials. Their findings suggest that several schemes for stationary tube pulse detonation engines can be addressed with thermal barrier coatings, convective cooling, and in some the need for exemplary lean fuel air mixtures¹³. Two of the most feasible cases are fully purged with cool air, and using bypass air to provide convective cooling on the outside of the combustor. Their studies did not focus on the need to provide cooling for any DDT geometry present, which for the most part, has been the primary focus of research and displays susceptibility to damage.

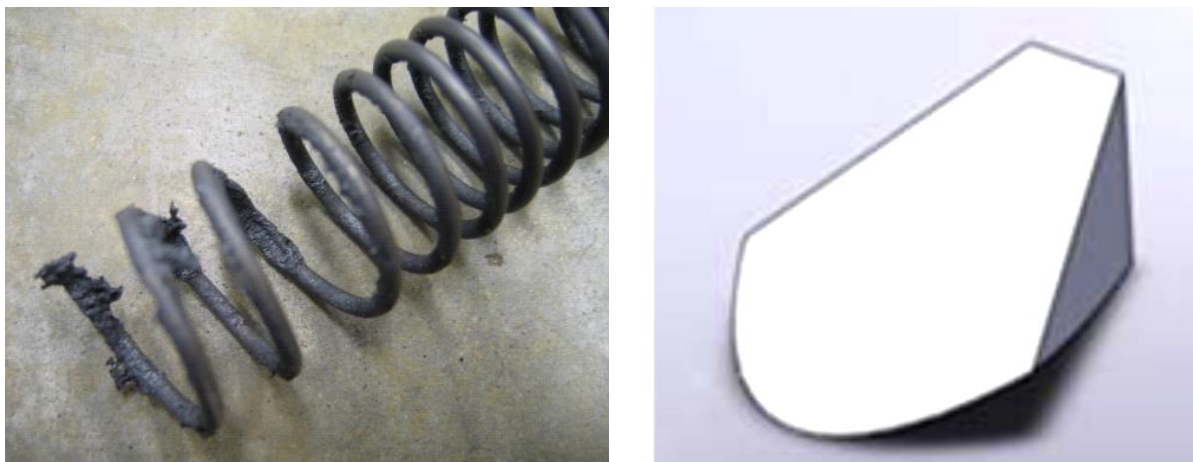


Figure 3 Shchelkin Spiral after testing PDE Mark 1 for a few seconds¹⁴ and Naval Postgraduate Swept Ramp Obstacle⁶

A common obstacle used for DDT is the Shchelkin Spiral that is in essence a helical wire. This form of geometry is very susceptible to the high temperature and pressure gradients as can be observed in the above image by the physical damage and signs of melting. Another obstacle investigated by the Naval Post Graduate School was the swept ramp used to generate vortices and turbulence. Both CFD and high speed imagery display high temperature and pressure gradients that could be of concern^{5, 6, 20}. The use of physical DDT geometry necessitates the need for additional thermal management, and in most cases the short duration of testing has worked well for experimental test rigs. However, limiting the operating time in real applications is not a practical method for cooling, prompting active cooling methods and likely maintaining a certain level of purge within the cycle¹³.

2.4 Deflagration to Detonation Transition

Detonations can be initiated directly at a high cost using detonable mixtures or high initiation energy. For useful hydrocarbon fuels with air, the initiation energy required is on the order of several thousand Joules, given the cyclic nature of these devices the power consumed by ignition may outweigh the gains of detonation¹⁷. It is therefore of interest to focus on low energy initiation (10-250 mJ) techniques and achieve deflagration-to-detonation transition.

The initial stage of the flames' turbulent growth and expansion is dominated by large scale vortices and eddies that stretch and fold the flame surface expanding the area and increase the reaction rate, unless excess mixing quenches the flame. In later stages the heat release rate is sufficiently high where quenching no longer retards the chemical reaction rate and small scale turbulence dominates. The role of the formed pressure wave serves to compress, heat and intensify the turbulence present in the flow field and adds to the fluid instabilities. The actual transition to detonation can involve several paths once a sufficient flame velocity and shock strength have been generated. The local unburned pockets of fuel and air in the products undergo local detonations/explosions forming blast waves that in essence further strengthens the leading shock and increases instabilities. At this point the shockwave has sufficient strength to autoignite the fuel air mixture immediately behind the wave, and is thus detonation. It is also important to note that within this final DDT transition, instabilities in the boundary layer adjacent to the wall and local explosions/detonations, there exist shock reflections and interactions leading to the formation of the triple point structure¹⁸.

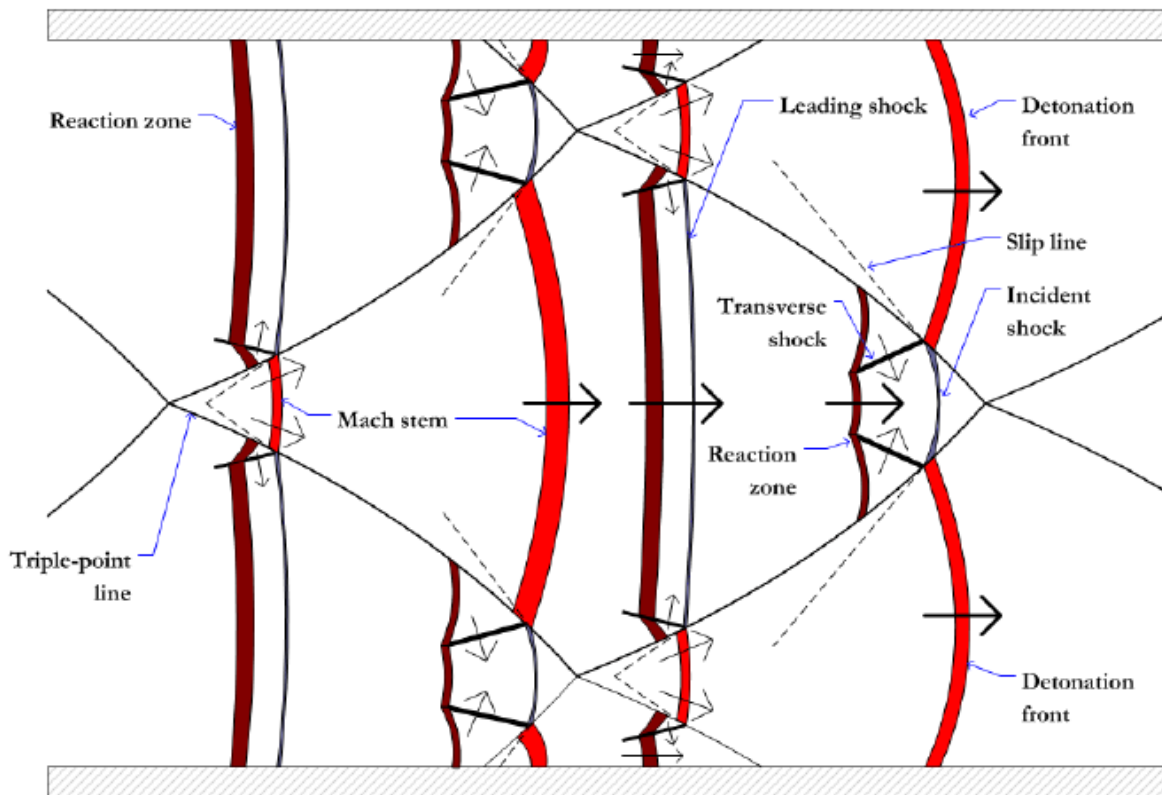


Figure 4 Detonation Wave Structure¹⁴

The above figure is a depiction of the detonation wave structure. Through each reflection and shock, the temperature and pressure increases leading to higher chemical reaction rates. The distance between the shock and chemical reaction region becomes increasingly small and a strong coupling is formed and becomes self-sustaining.

2.5 The Fluidic Technique

The concept of utilizing fluidic jets to simulate physical obstacles and cause flame deflection is fairly new in this application. Results at the Air Force Research Laboratory (AFRL) by Knox, Stevens, Hoke and Schauer show that fluidic impingement slots can decrease the DDT length and improve performance in DDT time and distance along with reductions in flow losses during blowdown^{1, 3}. From their findings the most important parameters are: momentum ratio, effective blockage ratio, and the fluidic jet composition. These studies were conducted with Hydrogen-Air

mixtures and fluidic jets comprised of air, nitrogen and stoichiometric hydrogen-air mixtures for various tests¹⁻³. In later studies conducted by Richter the deflagration wave front acceleration was shown to significantly increase due to the turbulence generated by the fluid obstacle in comparison to a physical counterpart displaying similar flame deflections^{4, 24}.

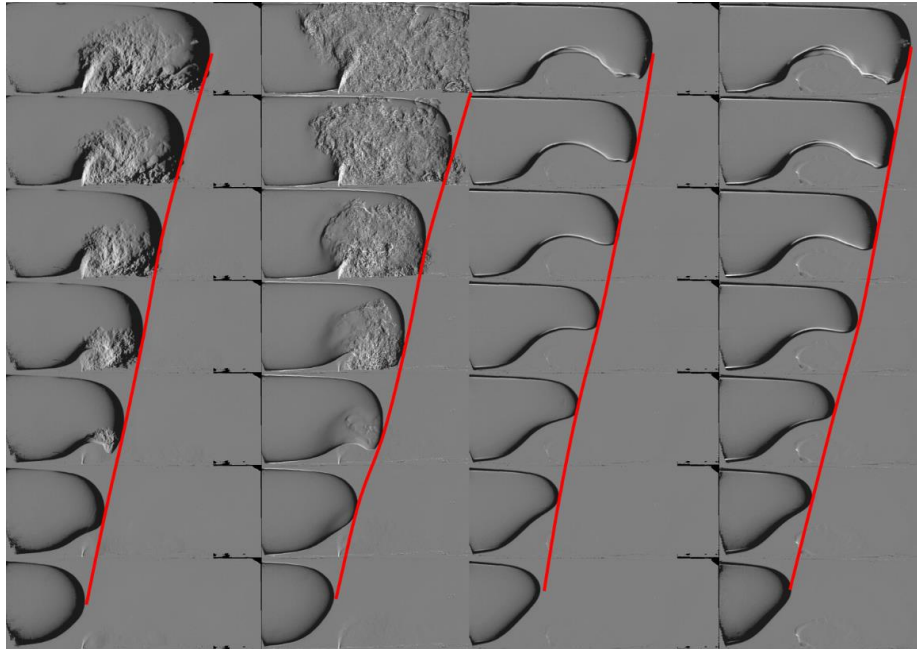


Figure 5 Effect of Varying Flame Equivalence Ratio on Obstacle Interaction. Left Fluidic MR 0.3 Φ 0.7, MR 0.3 Φ 1.0, Right Physical Blockage BR 0.2 Φ 0.7 and BR 0.2 Φ 1.0²⁴

Figure 5 is a side by side comparison of the interaction between a planar slot jet and a comparable physical blockage with time increasing in the Y direction. The downstream flame profile in the fluidic case is significantly more turbulent in comparison to the physical blockage case by observing the plentiful wrinkles in the schlieren images, and furthermore, the flame surface is significantly larger. The mechanism responsible for the performance increase in the slot jets for both laminar and turbulent flame acceleration is the increase in turbulent intensity and fluidic strain rate^{24, 25}.

Other jet geometries display improved penetration, turbulence generation or coherent vortex structures. In studies conducted by Milanovic and Zaman the JICFs were angled and yawed

to improve the jet spread and create long lasting stream-wise vortices⁷. In several cases with pitch and yawed jets the vortex structure was a single filament, not the typical vortex pair expected from JICFs normal to the wall. With this observation, the vortex structure can be controlled and optimized for penetration, vorticity or mixing depending upon the desired parameters⁷. Furthermore, jet geometry also has merit. The previously studied circumferential slot jets by Knox displayed properties similar to their physical counterpart aside from an inability to reflect pressure waves. Different geometries and orientations can display contrasting features. The stream-wise slot jet is an excellent choice for penetration, a typical round jet tends to induce turbulence and a vortex pair whereas the previously tested slot jet displays a generous spread but limited penetration¹⁵. Depending what attributes are desired, other geometries and orientations can be used to improve the production of turbulence over the slot jet. In studies conducted by Myers⁵ the creation of stream wise vortices may be more valuable than the small scale turbulence produced by Knox^{2,3} or those produced by using physical orifices for at least the initial stages of accelerating the flame front. However, the finer scale turbulence is highly beneficial in the later stages.

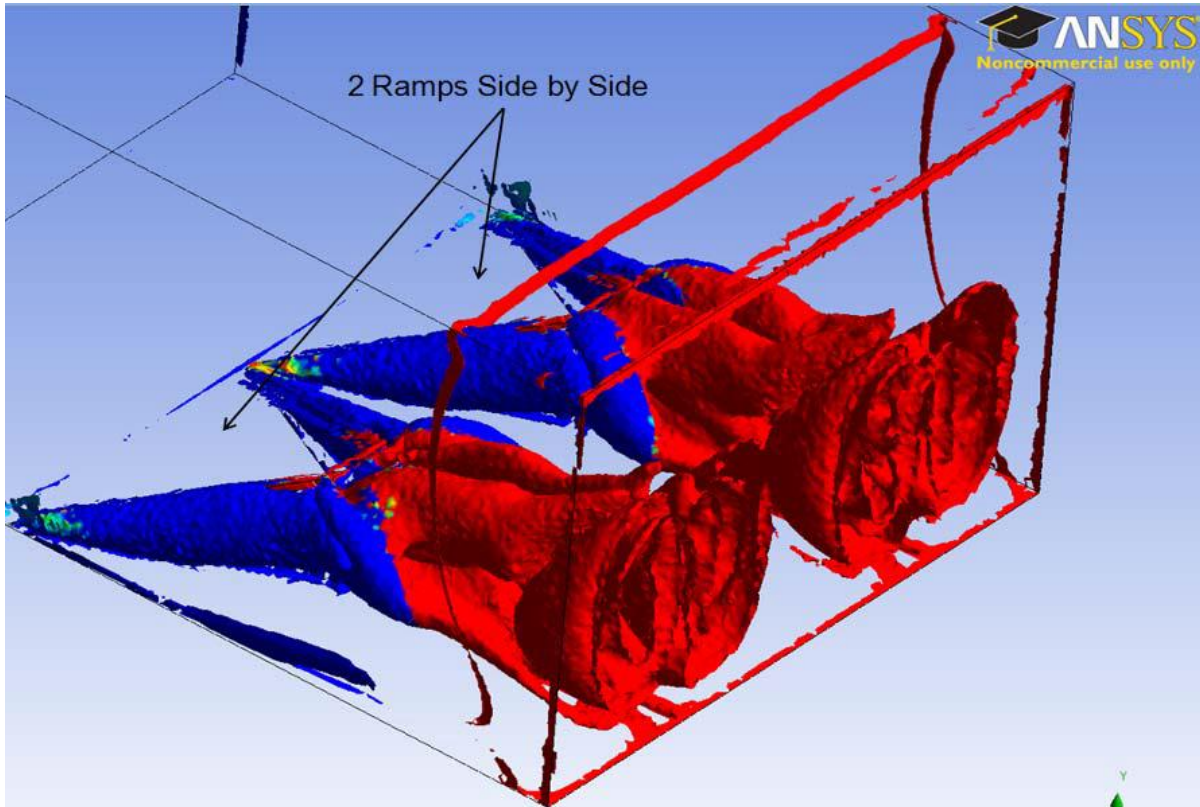


Figure 6 NPGS Swept Ramp Vortices⁵

The swept ramped obstacles developed by the naval postgraduate program create strong streamwise vortices and have displayed the ability to accelerate and expand the flame front. Furthermore, in the later stages of flame development, consistent detonation kernels were formed in the wake of the obstacle due to the pressure and velocity profiles⁵. The interest presented with this finding in the initial stages leads to the concept of using a circular JICF to create a vortex pair as the examined obstacles. However, unlike the swept ramp, the JICF will not introduce geometry needed to reflect pressure waves.

3 Experiment and Design

3.1 Objectives

The first goal of the study is to test and compare the performance of physical DDT obstacles to the previously examined valved fuel and oxidizer studies by Tate and Gagnon^{8, 30}. The information of interest is the pressure and flame history during combustion and flow losses during filling. Focus being placed on flame acceleration, post shock pressure, and flame detection time for the array sensor positions. The fluidic investigation is to determine the dominant flow structures required to effectively accelerate the flame using a single oriented JICF using additional air. Two basic flow structures can be generated; streamwise vortex filaments, and turbulent eddies. Negatives of the fluidic method employed will include leaning the fuel air mixture and quenching. Due to the nature of the study it will only narrow the region of interest for future studies. Given the goal of higher efficiencies, flow losses during filling and blowdown must be addressed. The losses during blowdown can decrease the specific impulse (normalized thrust) by as much as 50% and the use of excess obstacles can impede detonation waves²⁸. A streamlined bluff body will be investigated leading the JICF and single orifice to quickly examine the benefit.

3.2 Experimental Plan and Structure

3.2.1 Phase #1: Physical Obstacle Configurations

Phase 1A of experimental testing was to verify the operation of the valveless pulse detonation combustor and compare the results to trials conducted by Chapmin, Tangirala and Dean in Detonation Initiation in moving Ethylene-air Mixtures at Elevated Temperatures and Pressures¹². The physical obstacles consisted of blockage ratios of 44% separated by an axial spacing of $1 x/D$ and using stoichiometric fuel air mixture.

Phase 1B examines several developed obstacle configurations developed by Christopher Tate's and Nicole Gagnon's studies at The Gas Turbine Lab^{8, 30}. The information of interest is the performance with dynamic filling of varying equivalence ratios and pressure loss during filling. Fill velocities of 28 m/s will be used with equivalence ratios of 1.00 and 1.3.

3.2.2 Phase #2: Single Orifice

The physical reference for the fluidic trials is a single orifice, supplying a uniform blockage. The 3 blockage ratios selected for testing are 24%, 44% and 59%. The metrics of interest include the time histories of the pressure developments, ion sensing and pressure loss. It is important to note that several differences exist between the setups for the orifice cases and JICFs. These differences include the additional leaning of the fuel air mixtures supplied by the JICFs and the use of spacers to maintain orifice position.

3.2.3 Phase #3: JICF Turbulence Generator

The JICF's ability to generate streamwise vortex and/or turbulent eddies is a function of jet strength and orientation. This study is examining the overall effect of the produced flow structure. Other studies have concentrated on the flow structures produced by angled and yawed

JICF's; however, the physical boundaries of this study does not match due to the circular profile and likelihood of JICF interaction with the opposing wall. Therefore, this study is only useful for narrowing regions of interest as a concept screening.

3.2.4 Phase #4: Bluff body and JICF



Figure 7 Bluff Body 1.250" Throat

It became apparent that the pressure development inside the combustor has a strong correlation with the effectiveness and location of a local pressure surface to increase the favorable pressure gradient. Fluid jets in crossflow are unable to act as a pressure surface or reflect shocks, leading to the need for a physical surface, especially since the static pressure during blowdown is greater than the total pressure supplied by the blower. This enables a generous backflow which is not favorable. The location of the upstream pressure surface has an impact on pressure development, and with sufficient chamber volume between fuel injection and the porous thrust surface, it still displayed a weak reflection; however, significantly favorable in comparison to the unrestricted flow path. The idea for inserting a bluff body into the flow is to impose a local pressure surface inside the DDT section. In observations of the single orifice tests at the same axial location of the JICF, the features of the flow field and flame front develop differently as to be discussed.

3.3 Pulse Detonation Combustor Design

The proposed study requires the test section to contain a moving fuel and air column at a moderate range of mass flows in order to create the stream-wise flow structure of interest using the JICF technique. A valveless pulse detonation combustor was designed and assembled in house with the main airflow supplied by an industrial blower and valveless fuel injection manifold using a circular pattern of JICFs. This combination produced a test rig with an ability to supply a large range of flow rates with control of the mixture fraction under roughly ambient conditions.

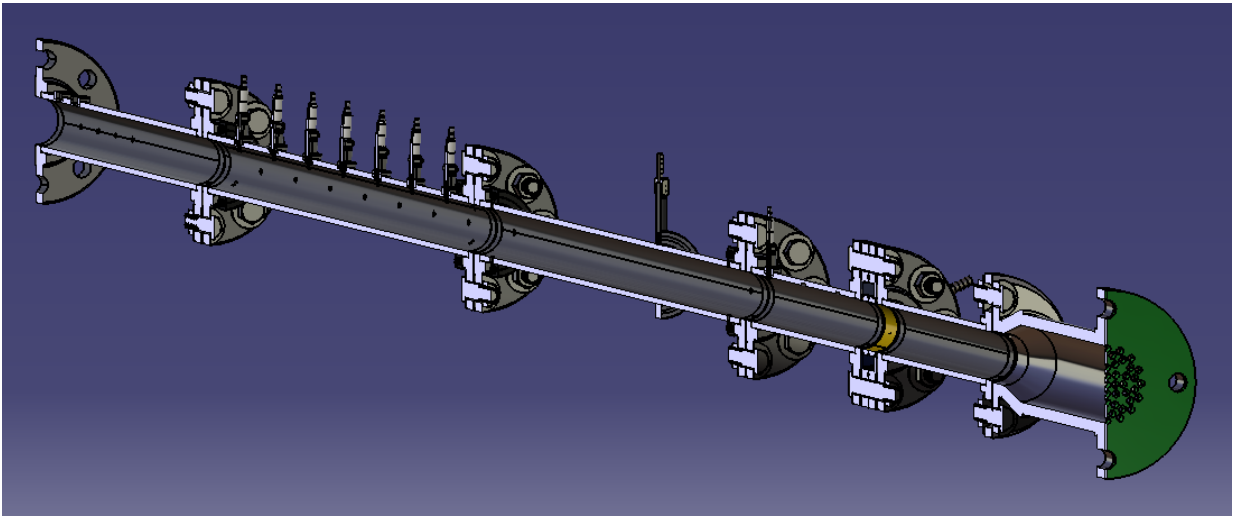


Figure 8 PDE Test Section

The above figure is a section view of the test chamber. The Green plate is the porous thrust surface, and gold is the fuel injection manifold liner. The inner diameter is 49.3 mm with the exception of the flex hose reducer of 76.2 mm.

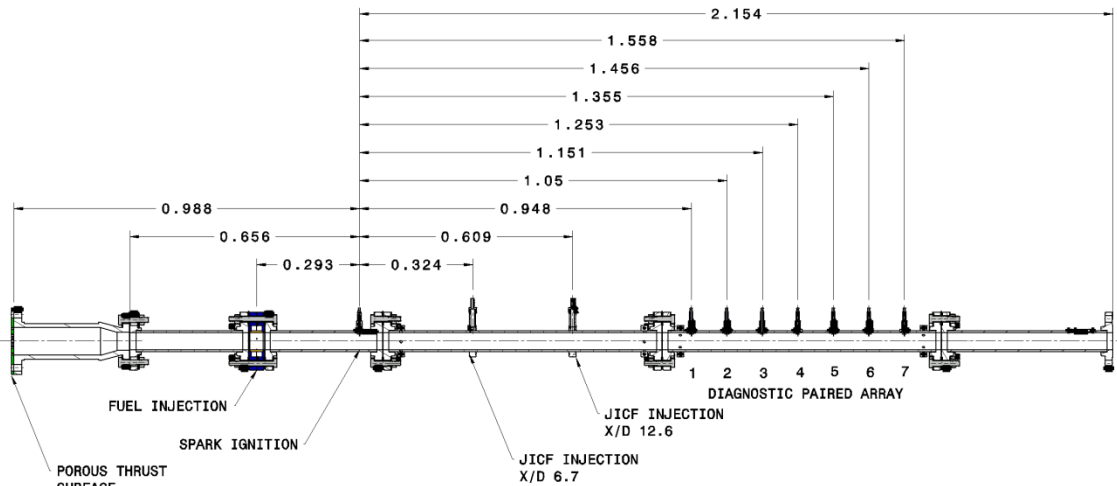


Figure 9 Dimensioned Test Section, Axial Positions in meters

The above figure displays the axial positions in inches of all major components. The Diagnostic array comprises of ion sensors and dynamic pressure transducers. The porous thrust surface is the entry location for the bulk airflow supplied by an industrial blower and will be discussed more in detail.

3.3.1 Fuel Injection Design

The mixture in a pulse detonation combustor has an impact on performance and the likelihood of achieving consistent ignition and DDT. Several CFD studies were conducted for various fuel air mixture schemes using patterns of JICFs of pure fuel into the main air stream. To achieve the desired operating frequency, it was chosen to pursue a valveless air and fuel supply. The design of the fuel injector scheme was based upon studies conducted by Braun, Balcazar, Wilson and Lu from the University of Texas at Arlington on High Frequency Fluidic Valve Fuel Injectors¹¹. Their study indicates the ability JICFs to be used for fuel addition in pulse detonation combustors. Detonation will reach post wave pressures of 6 to 10 atm whereas deflagration cases develop 1 to 3. The actuation of the fluidic fuel injector depends upon supply pressure and the geometry of the jet and plenum chamber. The actuation is driven by the pressure rise in the tube

due to the heat release and expansion in a confined chamber, as the static pressure increases the favorable pressure gradient across the jet decreases causing the flow to stagnate, and possibly affect a slight amount of backflow stopping the addition of fuel. Once the pressure subsides during blowdown the pressure gradient becomes favorable and fuel flow starts once more. By using supply pressures of 2-3 atm, the JICF fuel injection scheme will actuate without active control for deflagration cases. Once the pressure subsides in the PDE tube, the fuel flow will restart and deliver fresh reactants.

For operation frequencies between 10-25Hz a 4 port fuel injector equally spaced and nozzles rotated 22.5° off normal, were found to achieve equivalence ratios between 1.0-1.3 while displaying favorable mixture distribution at the spark plug's location of 11 inches downstream of the fuel manifold. The mixing distributions were analyzed by Fluent using steady state filling parameters as would be observed. It must be noted that the CFD studies were primarily used to screen jet configurations for mixing while information from previous studies¹⁵ was used to determine jet size and number based upon predicted penetration and spread.

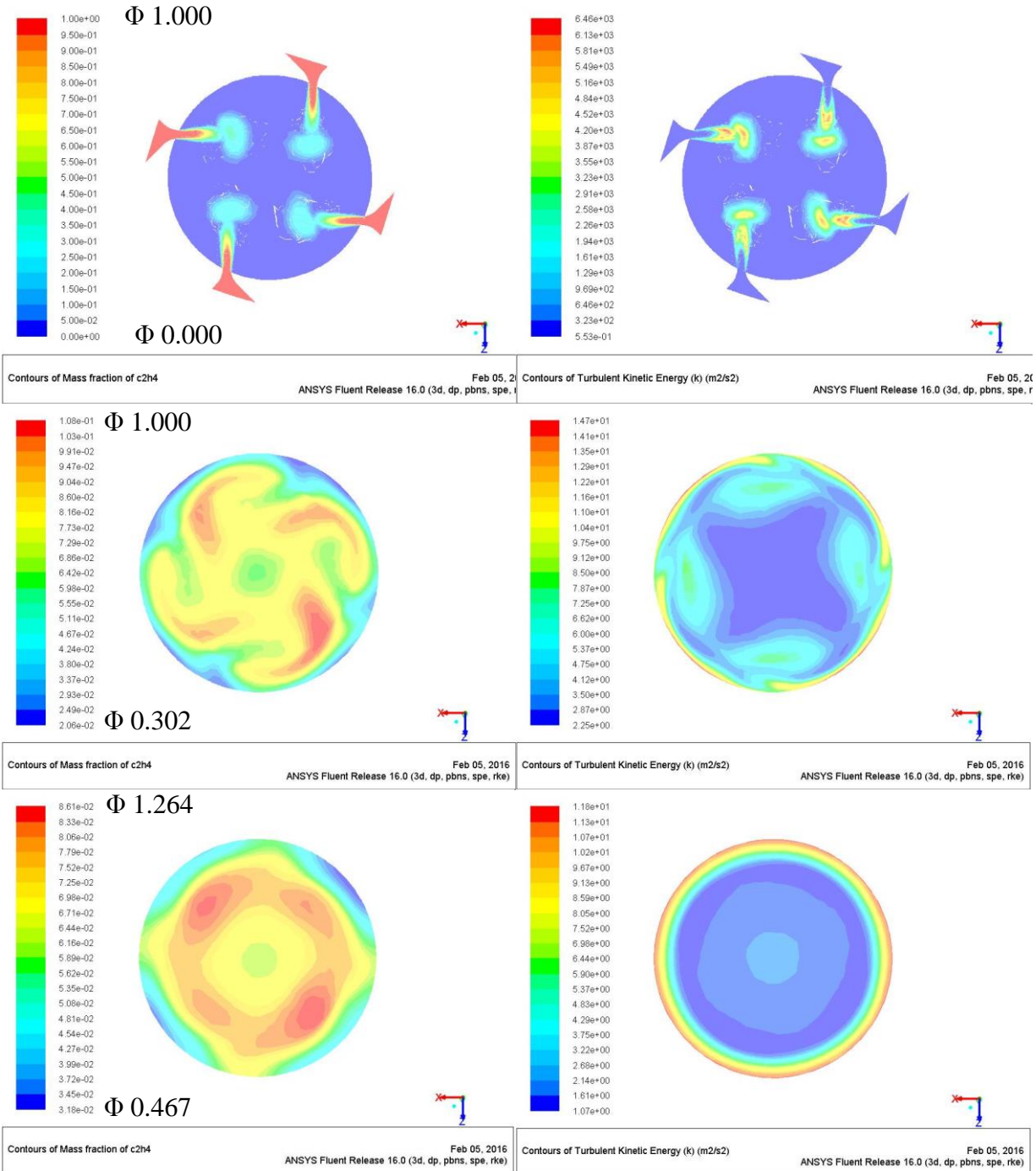


Figure 8 Fuel Injection and turbulence kinetic energy, injection plane, 6 inches downstream and spark plane $M_{air} 0.128\text{kg/s}$

As can be noted from the study, a 4 port angled 22.5° yawed 90° pattern displayed favorable mixing in the 11 inches required to ignite the mixture even at higher than tested flow rates as in the above figure. At 0.0540kg/s and target $\Phi 1.05$ the range at the spark plug is between $\Phi 0.919$

to 1.064. There is a component of rotation and higher levels of turbulent kinetic energy present that will help create a turbulent flame brush as the kernel expands.

3.3.1.1 Fuel Manifold



Figure 10 Fuel Injection Manifold

The design of the fuel injection manifold allows for the replacement of the liners allowing for a multitude of uses and configurations as seen in the above figure. The uses include fuel injection as the current study, but could also be used for testing radial patterns of JICFs. The connections are standard 3/8 NPTF and 4x 3/8-16 SHCS for pre-assembly easing use.

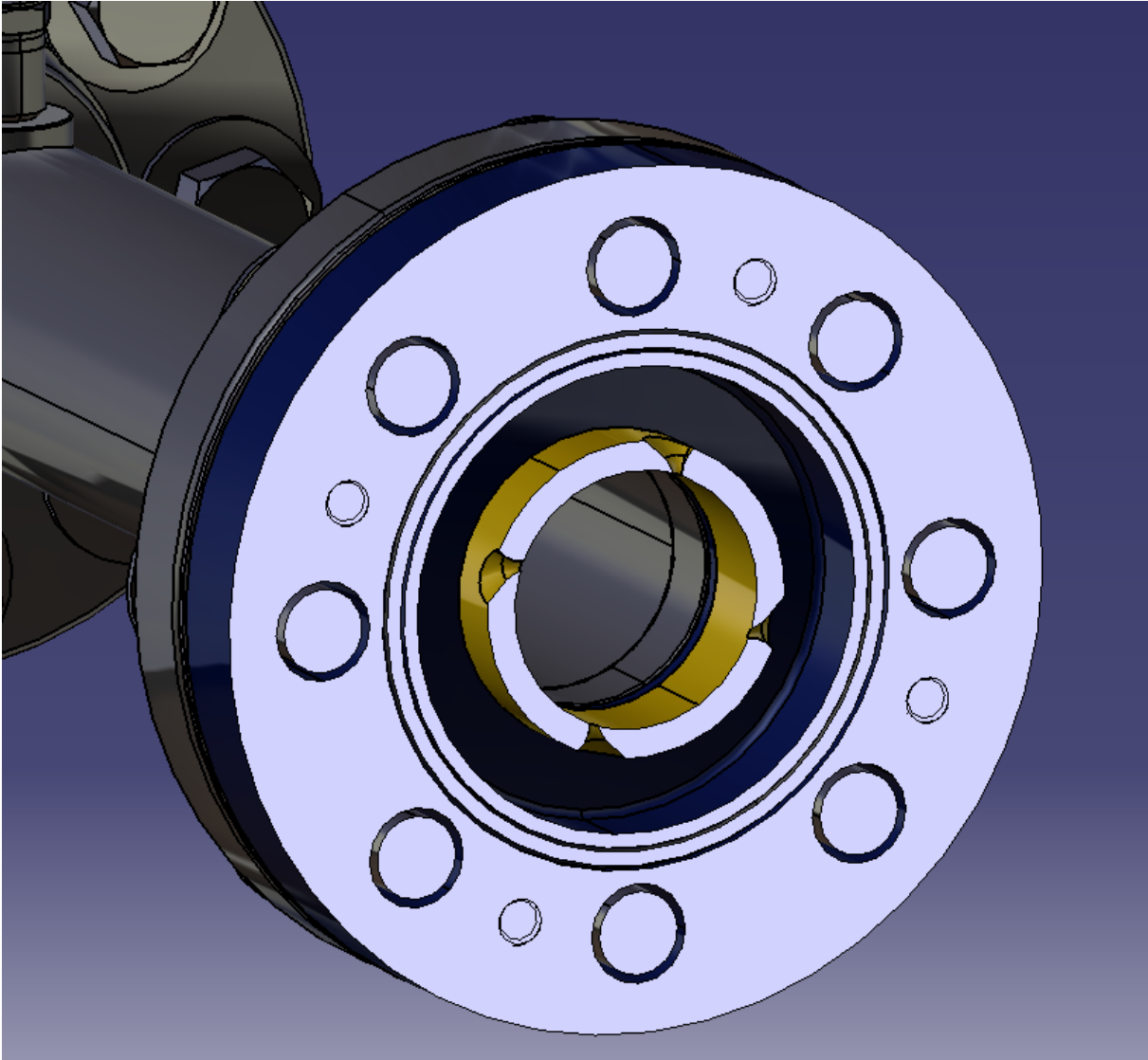


Figure 11 Fuel Manifold Plenum Chamber with 4x $\alpha 22.5^\circ \beta 90^\circ$

The plenum cavity in the manifold is large allowing the static pressure strain gauge to read the total pressure as the velocity is relatively low even for the highest mass flow rates of fuel with plenum velocities well under 5 m/s. The gold colored object is the fuel injection liner while the blue is part of the clamp together manifold. The plenum chamber is roughly 31.8 mm wide with an annulus of 60.3 mm to 88.9 mm making for approximately 107 cm³ in volume.

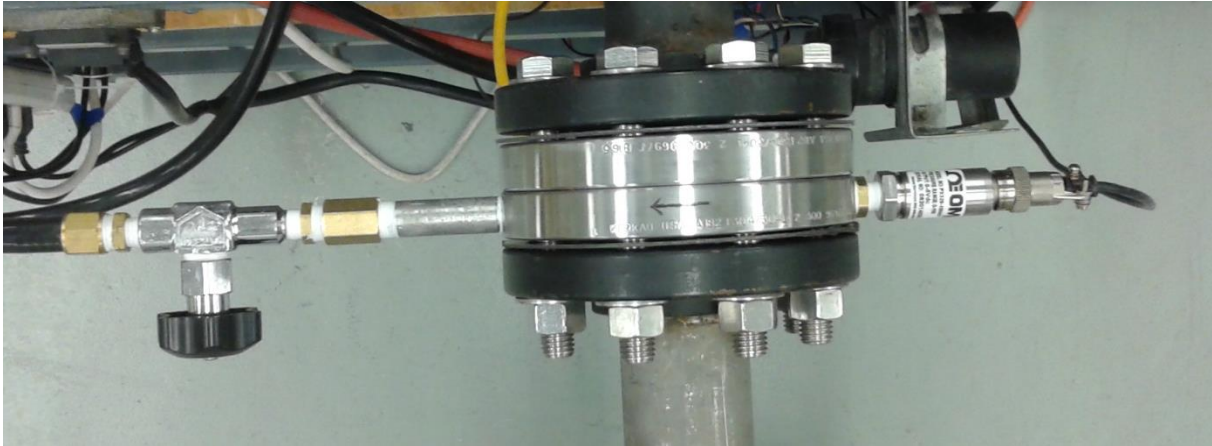


Figure 12 Finalized Fuel Injection Setup

Figure 12 displays the final mechanical configuration of fuel delivery. As the fuel supply cannot match the demanded flow rate, a small chamber leading the SV3503 Solenoid was maintained at a high pressure and the use of a needle valve, a ported Matheson LMF4375P, restricted the flow to create a plateau of fuel delivery to the manifold for a short period of time.

3.3.1.2 Calibration

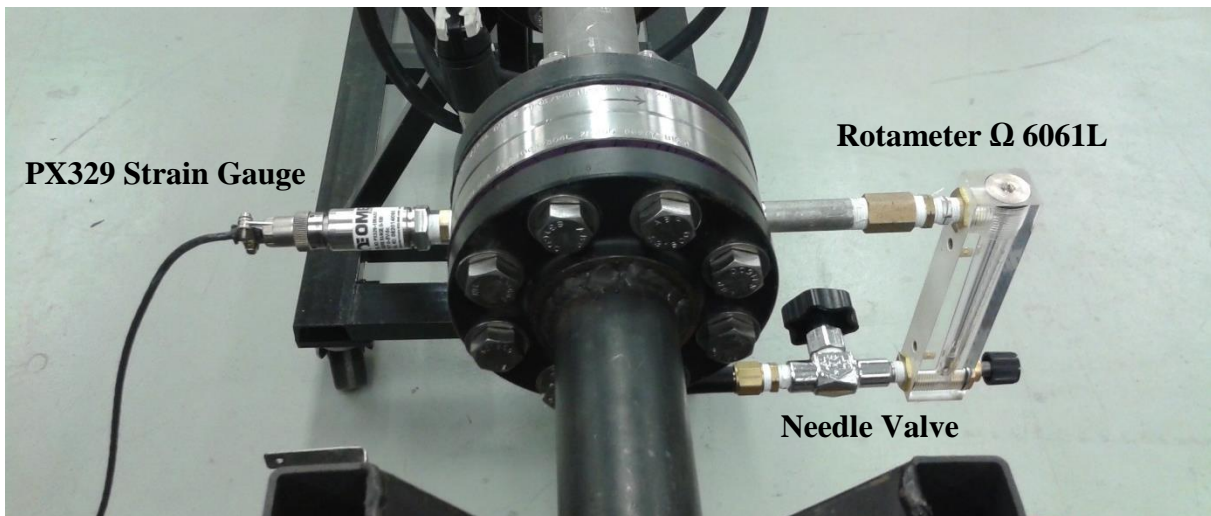


Figure 13 Fuel Injection Calibration

The fuel manifold pressure and corresponding steady state flow rates were established using a compressed air supply and a rotameter, Omega 6061L. The PX329 static pressure strain gauge being used in conjunction at the exit of the Rotameter and attached to the fuel injection

manifold. Corrections were applied to account for the slight differences between air and the ethylene fuel used. The resultant calibration curves for mass flow rate were curve fitted to the static pressure measurements in the manifolds plenum chamber allowing computations during post processing to compute the equivalence ratios.

Calibration with a rotameter was conducted using compressed air at 80 psi from the accumulator tank and using the needle valve to set CFM. The pressure was taken in two steps without adjustment of the rotameter or supply pressure. The first pressure measurement by the PX329 was taken at the Rotameter exit using 3/8 NPT Tee fittings and swapped to the manifold for a second static pressure measurement.

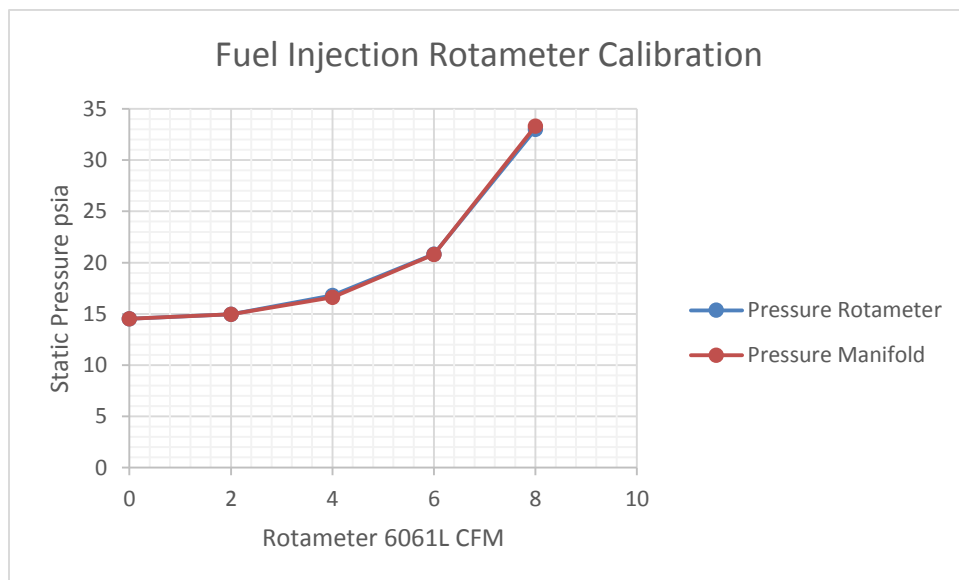


Figure 14 Fuel Injection Calibration of Pressure vs. Volumetric Flow Rate

As can be observed, there exists little difference between the static pressure in the line immediately following the rotameter and the manifold. The trend is also nonlinear as to be expected, and with known supply conditions the mass flow rate can be computed.

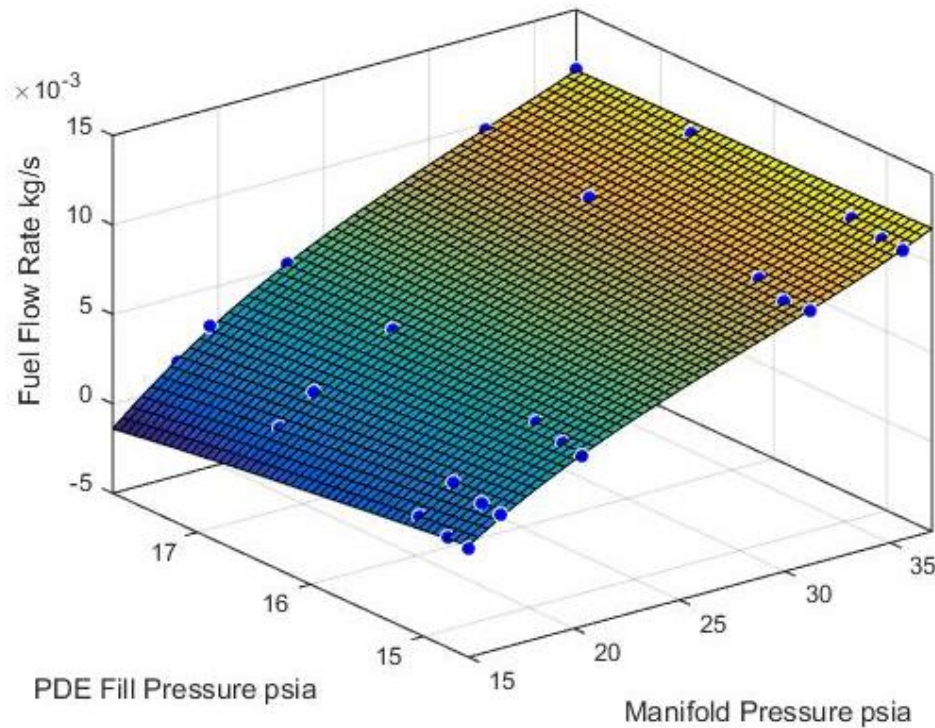


Figure 15 Fuel Manifold Calibration Curves

The fuel injection curves are from results obtained using the 6061L Rotameter and PX329 Static Pressure Strain Gauge. The relationship between the manifold pressure and mass flow rate is nonlinear as expected. The nozzle mass flow rate is a function of fuel temperature, combustion chamber pressure, and primarily manifold pressure. Chamber pressure during filling impacts the fuel flow rate and for the cases of physical DDT geometry it is significant.

It is important to note, that 1D predictions failed to accurately compute the mass flow rate in comparison with the rotameter except within a narrow region of interest included in the subsonic region below tested values. This is primarily due to incorrect assumptions based on the flow properties through the small orifice and the fact that the throat is not circular in cross-section nor exits normal to the wall. The curve fit equations for the mass flow rate of fuel in kg/s. P_F refers to the Manifold pressure while P_{PDE} is the chamber pressure during filling.

$$\dot{m}_{fuel} = C_{00} + C_{10}P_{PDE} + C_{01}P_F + C_{20}P_{PDE}^2 + C_{11}P_{PDE}P_F + C_{20}P_F^2$$

Table 2 Fuel Manifold Curve Fit Constants

Coefficient	Value
C ₀₀	4.1770E-02
C ₁₀	-7.5620E-03
C ₀₁	9.5990E-05
C ₂₀	3.7040E-04
C ₁₁	9.6650E-05
C ₀₂	-1.7970E-05

Table 3 4 Port Fuel Injection Information

Fuel Injection: 4 Port 22.5° Insert	
Drill: 5/64th, 7/32 Radius Countersink	
Angle	22.5°
Yaw	90.0°
Nozzle	Throat Dia. Inch
1	0.083
2	0.081
3	0.081
4	0.079

The above table displays the physical parameters of the injection insert. The throat diameters, not the hydraulic diameter, were found using pin gauges to accurately determine the size within 5/10ths. A trade size #2 Radius Countersink was used to drill the JICF nozzles into the tube followed by a 90 degree chamfer then polished to a mirror finish using a jewelers rouge and oil slurry.

3.3.2 Jet In Cross Flow

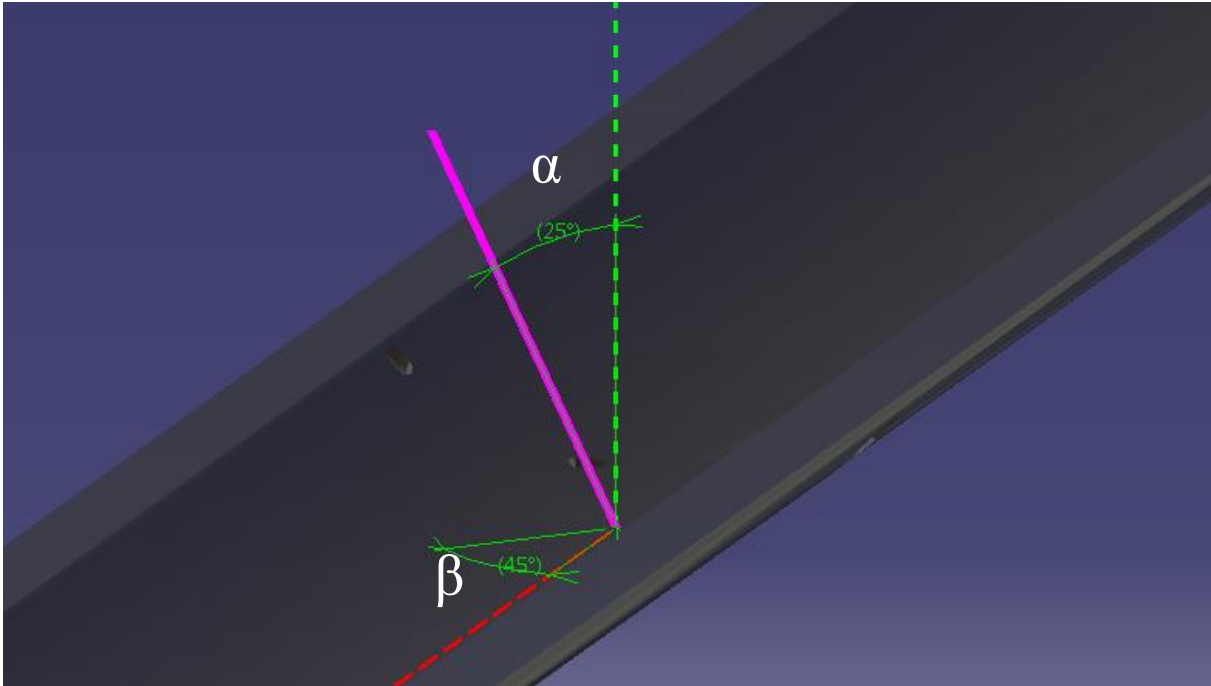


Figure 16 Jet Orientation Definitions, α 25°, β 45°

The JICF Turbulence generator technique employed uses a single jet that is pitched α with respect to the walls normal and yawed β from the downstream direction rotated about the surface normal. An array of 6 JICF's were drilled into the DDT section for use with a clamp-on air manifold. This method was by far the simplest and cheapest alternative without disturbing the flow with a physical protrusion that could skew the result.



Figure 17 JICF Clamp on Air Manifold in the aft position

The clamp on air manifold, as displayed in the above figure in the aft position, was fabricated using a steel pipe nipple and a milled shaft collar allowing for quick transitions between nozzles.

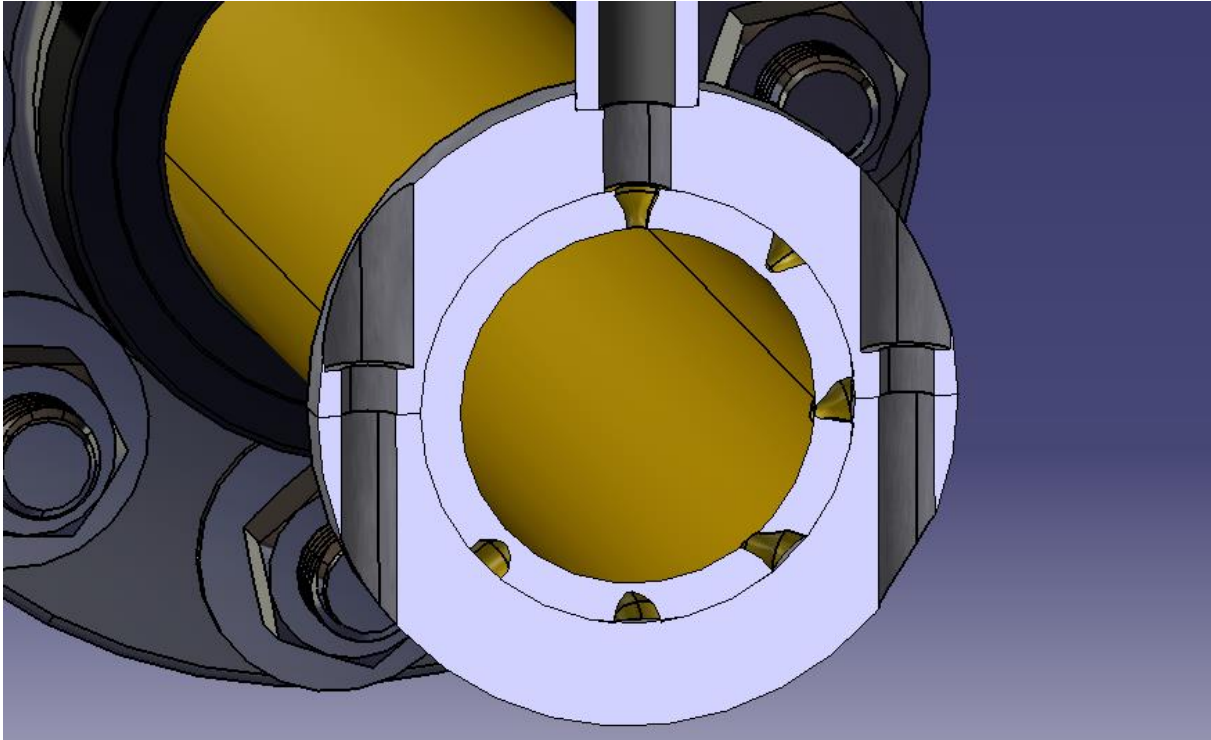


Figure 18 Jet Selection with Clamp-on Manifold

The jet is selected by rotating the manifold to the desired nozzle and securing the manifold.

Table 4 JICF Location and Orientation

JICF	Pitch α	Yaw β	Axial 13.0" Designation x/D 6.7	Axial 24.4" Designation x/D 12.56
Jet 1	0	0	JICF01	JICF10
Jet 2	25	180	JICF02	JICF20
Jet 3	25	135	JICF03	JICF30
Jet 4	25	90	JICF04	JICF40
Jet 5	25	45	JICF05	JICF50
Jet 6	25	0	JICF06	JICF60

Table 4 displays the JICF's and their physical information in regards to orientation. All nozzles were pin gauged to 0.113" in diameter within 5/10^{ths}. The axial distance is the separation

between ignition and the JICF's. By using findings from GE the distance required for a flame kernel to expand to the full diameter is roughly 20% of the length to achieve DDT and was chosen to be the closest plane of injection, x/D of 6.7^{12} . The x/D 12.6 location is the DDT tube flipped 180 degrees at the flanges to test axial spacing effects. The later portion, closer to the diagnostic section, allows for a closer look at the pressure and velocity developments near the jets; however, it must be noted that the flame front will be stronger and fully developed in that region.

This series of tests requires consistent operation of the JICF throughout filling and into blowdown. The design of the modular air supply was to provide a consistent and repeatable supply throughout the cycle and is able to attenuate between cycles.

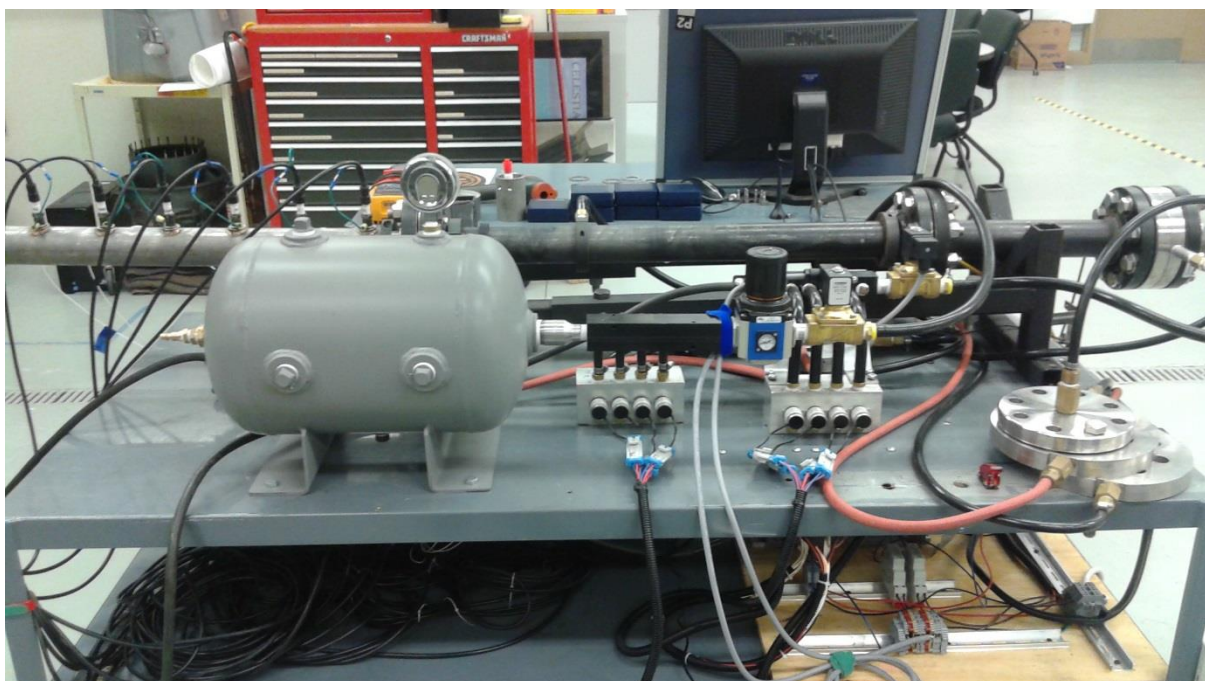


Figure 19 JICF Air Supply

This was accomplished with the use of an accumulator tank and pressure regulator. With the accumulator held at the wall supply of 78-80 psig and regulated to the desired supply pressure, it became possible to hold up to 70 psig for several seconds. It is important to note that the regulator, Nitra AR-443, was dynamically set to the desired pressure for every JICF.

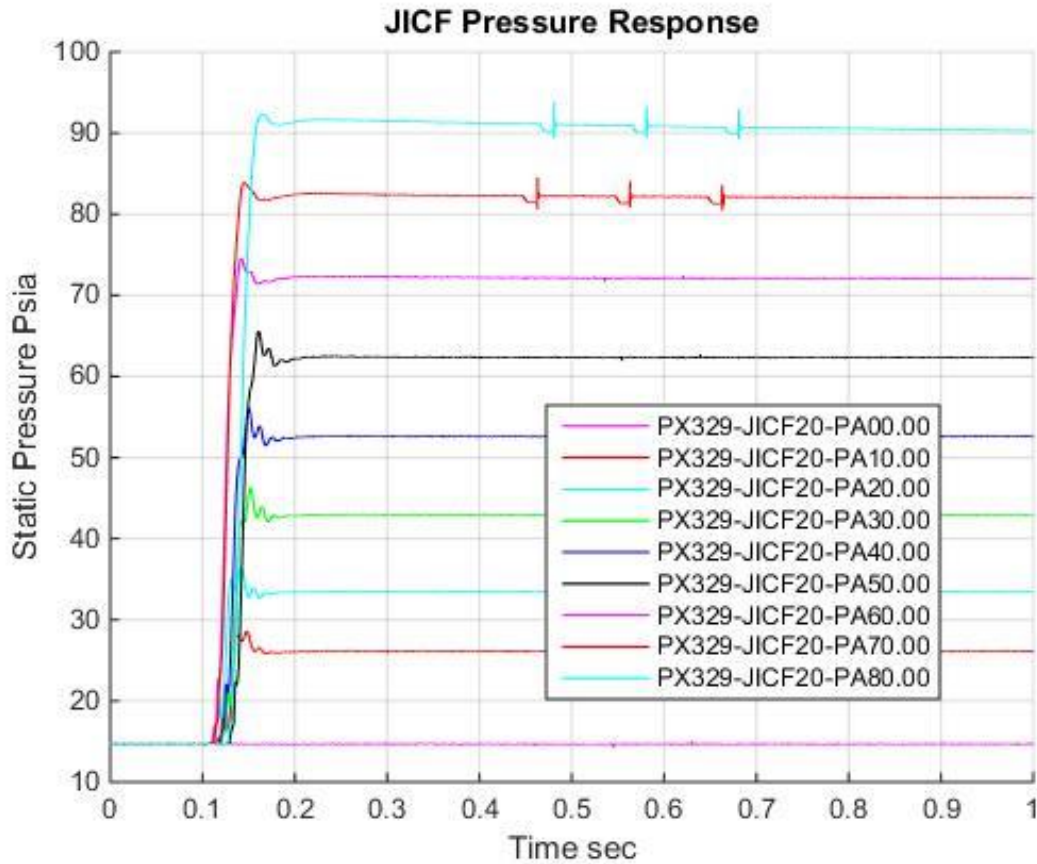


Figure 20 JICF Supply Pressure Response

Response of the JICF turbulence generator from 0 to 80 psi is displayed in the above figure. As can be easily observed, the response settles to near steady state before 200ms seconds and fuel is injected at 350ms in the cycle.

The metric used to compare the effectiveness of the JICF is momentum ratio between the JICF and the bulk flow. Previous studies focused on impingement jets in crossflow often use momentum flux and momentum ratio^{1-4, 7, 11}. Since this area of study is likely in the overblown region of operation, the momentum ratio will be utilized. Furthermore, the flow structures of interest are those propagated in the main flow and not the boundary layer along the wall.

Jet velocity at the nozzle's exit assuming choked flow, isentropic and adiabatic.

$$U_{jet} = U^* = \sqrt{\gamma RT^*}$$

The Momentum Ratio between the JICF and bulk flow is below and used to categories the JICF interactions. Due to difficulties correlating theory to calibration the MR was modified to use mass flow rate and the jets choked velocity.

$$MR = \frac{\rho_{jet} U_{jet}^2 A_{jet}}{\rho_{\infty} U_{\infty}^2 A_{PDE}} = \frac{\dot{m}_{jet} U_{jet}}{\dot{m}_{pde} U_{pde}}$$

Momentum Flux between the JICF and bulk flow is given bellow, and not used for this study. The usage for comparison is often studies within the boundary layer or those not in the overblown region where the flow structures no longer interacts with the surface.

$$J = \frac{\rho_{jet} U_{jet}^2}{\rho_{\infty} U_{\infty}^2}$$

3.3.2.1 JICF Calibration

The calibration method used the PX329 static pressure strain gauge and an Omega 6061L Rotameter with a constant air supply. With the use of a regulator, Nitra AR-443, and the 4.6 gallon accumulator tank at 80psi the supply air can hold a constant value for a considerable length of time. The rotameter indicates volumetric flow rate and with the known static temperature and pressure immediately after the meter, mass flow can be computed by the following equations.

Mass flow rate of calibration air

$$\dot{m}_{air} = \dot{Q} \frac{P_{static} MW_{air}}{Ru T_{static}}$$

Mass flow rate of fuel from air calibration

$$\dot{m}_{fuel} = \dot{m}_{air} \frac{MW_{fuel}}{MW_{air}}$$

Where the static pressure and temperature is of the gas immediately following the Rotameter. \dot{Q} represents indicated volumetric flow rate on the meter. It must be noted that the 6061L rotameter indicates flow rate in CFM and must be converted to the correct units.

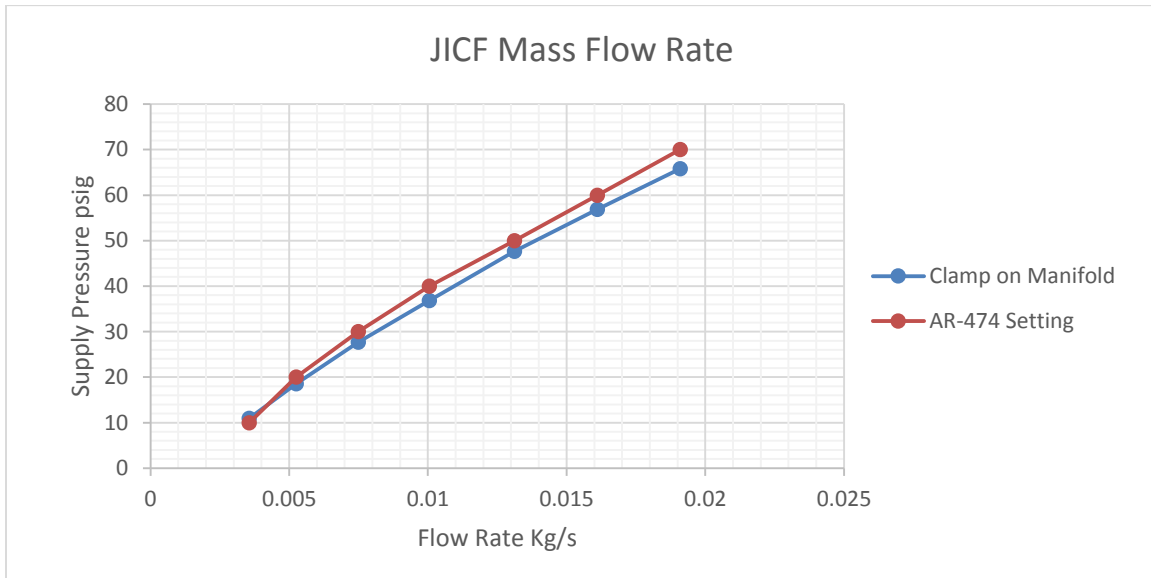


Figure 21 JICF Mass Flow Rate Calibration Curve

The above plot of the supply pressure setting and static pressure at the clamp-on manifold connected to JICF5 indicates some moderate pressure drop through the line. The pressures were taken with the PX329 strain gauge at the 3/8 NPT connection. The highest predicted bulk velocity estimated to be 41 m/s in the line at 70 psi. This relatively low velocity leads to a few simplifying assumptions and avoids some flow losses.

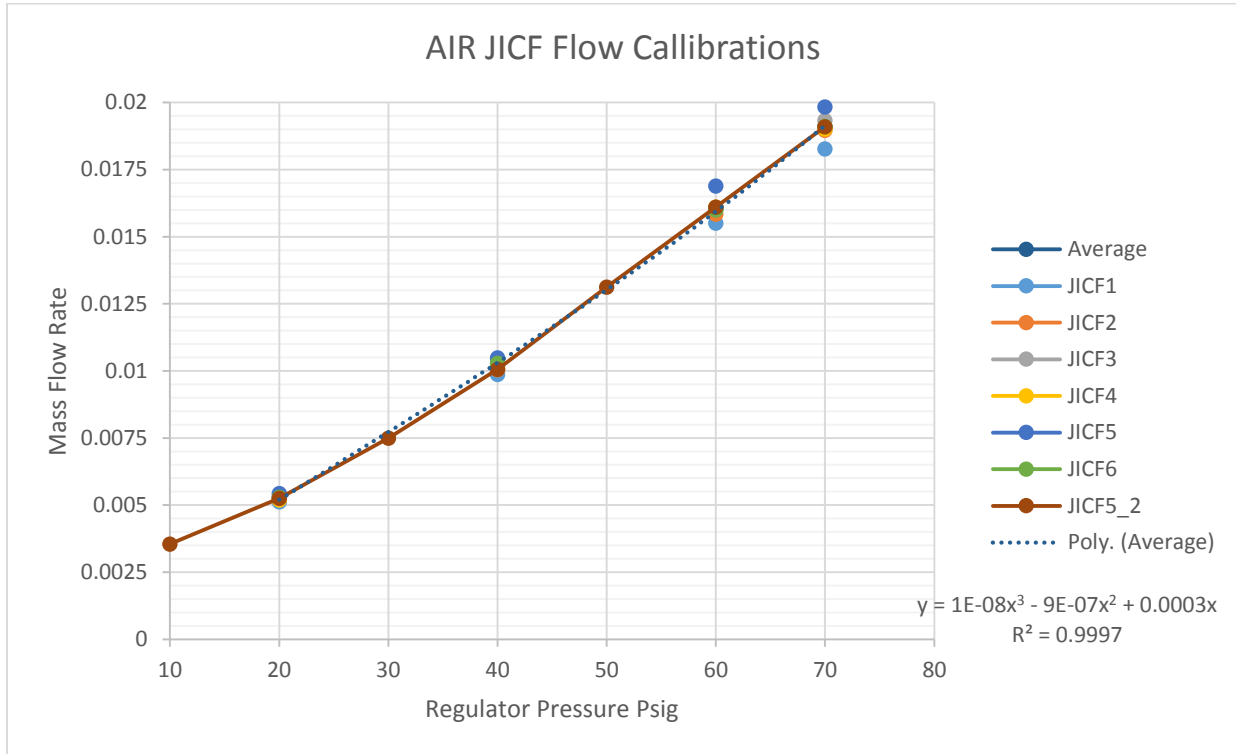


Figure 22 JICF Flow Rate Calibrations

The calibration curves for all JICF nozzles are displayed in the above plot. As can be observed, the flow characteristics for all cases agree fairly well until the highest pressure settings. The ability of the regulator to be set to a consistent value was found to deviate by up to 1.5 psi. This deviation adds uncertainty; however, given the nature of the test this is acceptable with the wide range of supply pressure tested.

3.3.3 Electrical System

The electrical system utilized the National Instruments USB-6351 data acquisition system to control the three outputs and sample Analogue Inputs. The advertised gross sampling rate for the AI is 1.25 MHz; however, this specific DAQ is capable of sampling at a gross rate of 1.4MHz with little cross channel contamination with the exception of the PX329 static pressure strain gauge.

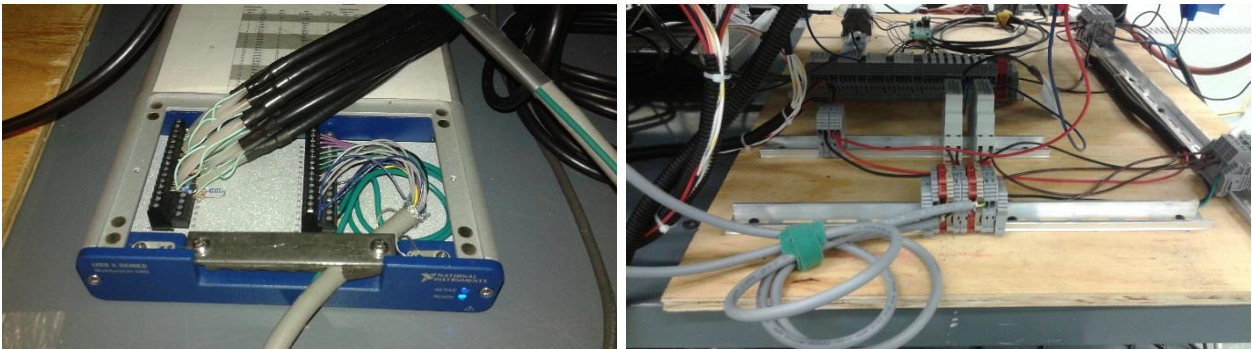


Figure 23 National Instruments USB-6351 DAQ and accompanying busses and power distribution

The outputs of the DAQ connected to standard 35mm DIN rail busses aided in the modularity of the system, thus simplifying additions to the test rig and allowing greater control of the power distribution and grounding leading to significant reductions in noise and interference with inputs. A further reduction in noise was the move from DC powered coils to using AC relays and coils for the Omega SV3506 solenoid valves. As a result, the only component that influences the analogue channels is the automotive ignition coil detected almost exclusively by the PX329 static pressure strain gauge. The contamination in the dynamic pressure transducers and ion probes is minimal, displaying a 5mV rise across all channels without resonance and scatter even during arc discharge. The interference with the PX329 is primarily from the voltage drop in the DC power supply from the coil charging.

3.3.4 Data Acquisition

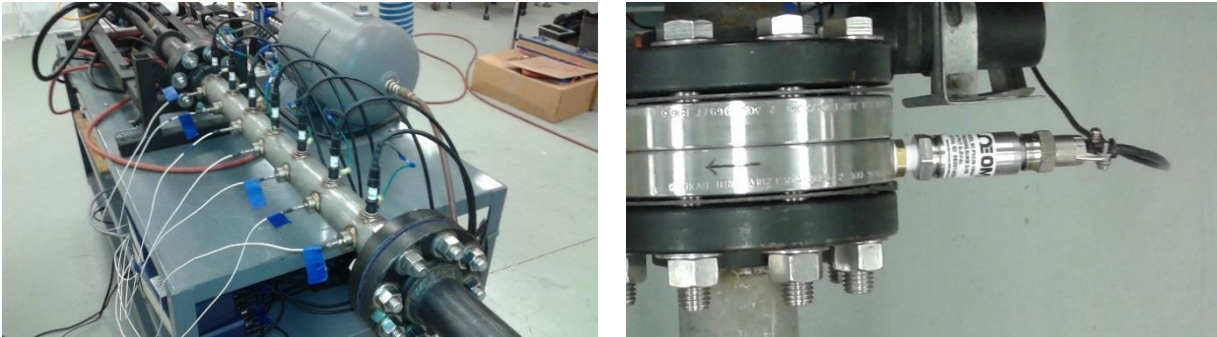


Figure 24 Test Rig Analogue Inputs, Dynamic Pressure, Ion and Static Pressure

The data input of the test rig comprises of three types of sensors: Static pressure strain gauge, dynamic pressure transducers, and conductivity “Ion” probes. The 7 pairs of dynamic pressure transducers and ion probes allow for the computations of flame and wave velocities and the detection of detonation events. It is important to note that the gross sampling rate of the DAQ is divided among the Analogue inputs. For this reason, various patterns were used in order to keep the sampling rate high enough per channel as to maintain a reasonable resolution. Configurations [1, 2, 4, 5, and 6] were scanned during sequential tests to gather data at all locations to develop the velocity trends per case.

Table 5 Scan patterns and sample rate per configuration

Pattern	Input Location #		Channel Sample Rate
#	Ion	Pressure	Hz
1	PX,1,2,3,4,5,6,7		156250
2		1,2,3,4,5,6,7	178571
3	1,4,7	1,4,7	208333
4	1,2,3	1,2,3	208333
5	3,4,5	3,4,5	208333
6	5,6,7	5,6,7	208333

During preliminary testing it was deduced that cross channel interference existed between the PX329 Static Pressure strain gauge and the first two scanned channels of static pressure

transducers. The analogue range for all sensors was -5 to +5 VDC to help improve the settling time; however, the ambient reading from the strain gauge being ~ 0.74 VDC while the rest was ± 2 mVDC. This offset displayed fairly significant cross channel buildup during sampling and lead to the removal of the PX329 sensor in all but one scan configuration. It is also important to note that sink resistors of 10KOhms were added in parallel to all AI's and a 1KOhm was placed in the open channel following the PX329, even with the addition of an empty channel the contamination was still present in the first input following. Another method explored, to a degree, was reducing the sampling rate; however, even at a 500 kHz gross sampling rate the cross channel buildup was still present; however reduced, and deemed not worth the loss in resolution

3.3.4.1 Ion Probes

Ion probes or conductivity sensors, operate with an anode and cathode held at a potential difference and when a conductive event occurs it closes the circuit and produces a voltage drop. Conductivity probes work for flame front detection due to the chemical reactions releasing ions and free radicals. The conductivity of the gas is a function of many factors including temperature, pressure, chemical processes and equivalence ratio. Another physical parameter of importance is the shape and proximity of the flame front to the wall. For deflagrated flames the actual front may not have a planar profile and could be conical as found in many studies leading to errors in detection. Detonations, on the other hand, produce a very strong and thin chemical reaction region that is nearly a planar allowing for accurate detection.

In previous studies held at ERAU Gas Turbine Lab, ion probes have consisted of Autolite 25 and 26 resistor spark plugs (8-10KOhm) connected to the PCB 482C amplifier in an open circuit with the ground connection being a common point on the PDE tube assembly. Noise due to EMF and other electrical interference was significant and in the cases of deflagrations can obscure the

relevant data as the signal response is weak and on the same order of magnitude as the standard deviations of the noise. The peaks during cycling AFS solenoid valves and the ignition coil also displayed larger magnitudes than the signals of interest. The two primary reasons for low signal strength and high noise ratio is the common ground with the spark ignition coil, and utilizing the amplifier in an open circuit configuration. The PCB 482C amplifier is designed to provide a constant current supply (2-20 mA, up to 26 VDC) while it amplifies differences in the driving voltage. A resistor in parallel (4.7 K Ω , 4.00 mA) allowed the system to operate as designed and displayed a signal strength 4 orders of magnitude higher than the background noise. The local ground being attached to the ion probe itself closed the circuit with the coaxial shield. This method did not display a large decrease in background noise and interference from the valves and coil until all inputs to the PCB 482C were isolated from the test rig ground. The end result yielded a clean signal that is not affected by the cycling of valves and the ignition coil charge/discharge while maintaining a high signal response.

3.3.4.2 Dynamic Pressure Transducers

PCB 111A24 Dynamic Pressure transducers use fused quartz and an internal amplifier to measure pressure gradients and static pressure changes within limits. They are well suited for shock wave measurements and pressure trends within shock tubes. The pressure transducers are used in conjunction with the PCB 482C amplifier with a 4.00mA driving current. The minimum resonant frequency of the transducers is 400 KHz and sampling at 200 KHz per channel will generally not cause large fluctuation in readings; while multiple runs decrease the uncertainty. Additional information can be found in appendix B2.

3.3.4.3 PX329

The static pressure strain gage, an Omega PX329, internally amplified with a 0-5 VDC output was used to record the fuel manifold pressure. The factory 5-point calibration can be found in Appendix B1. In order to help isolate and clean the signal a 10 VDC precision power supply was fabricated to supply the excitation voltage with a ripple of less than 1 mV.

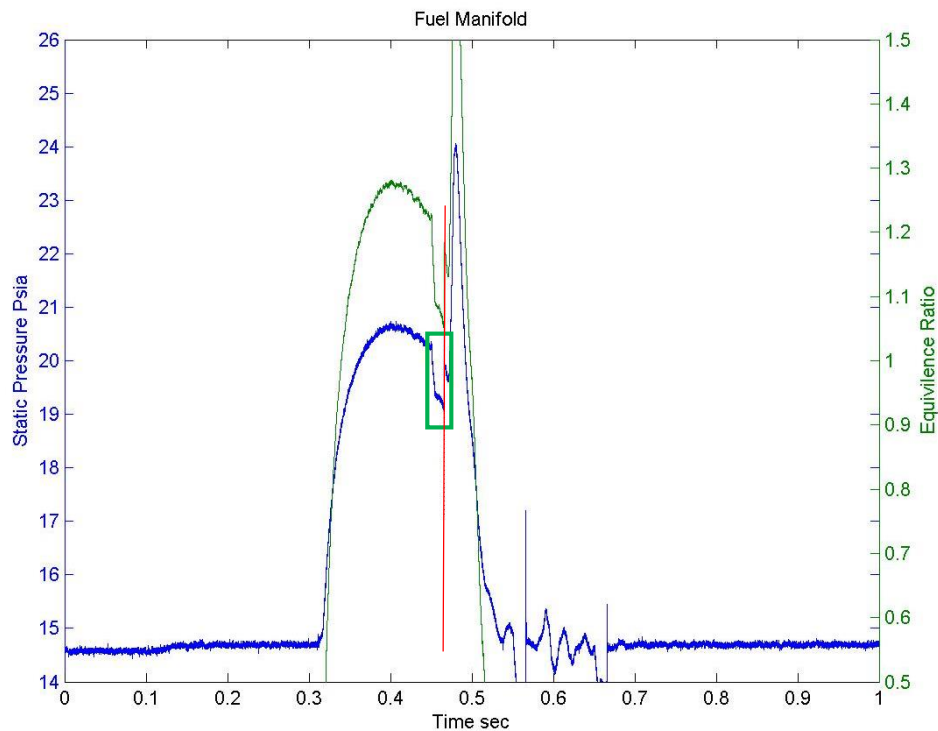


Figure 25 JICF20 at 60psi mass flow 0.0764 kg/s and an average Φ of 1.25, 4xPort 22.5° Injection

Unfortunately, the unit was supplied power from the common 13.9 VDC power supply and during charge and discharge of the ignition coil would register a deviation marked in the green box (figure 24); however, no harmonic was induced. This was later used during post processing to help determine the time between ignition and ion detection. The location of the spark discharge is represented by a red line in the above figure.

3.3.5 Bulk Air Delivery



Figure 26 Bulk Air Supply

Due to the large volumetric flow required, the economic solution was an industrial blower, a Spencer Turbine 15Hp VB110B. The blower is able to supply 0.18 kg/s of air with a clean tube configuration of length 2.76 m. A reducing section, an ANSI 150 class flex hose connector 3” to 2”, and a porous thrust surface to facilitate the required testing conditions.

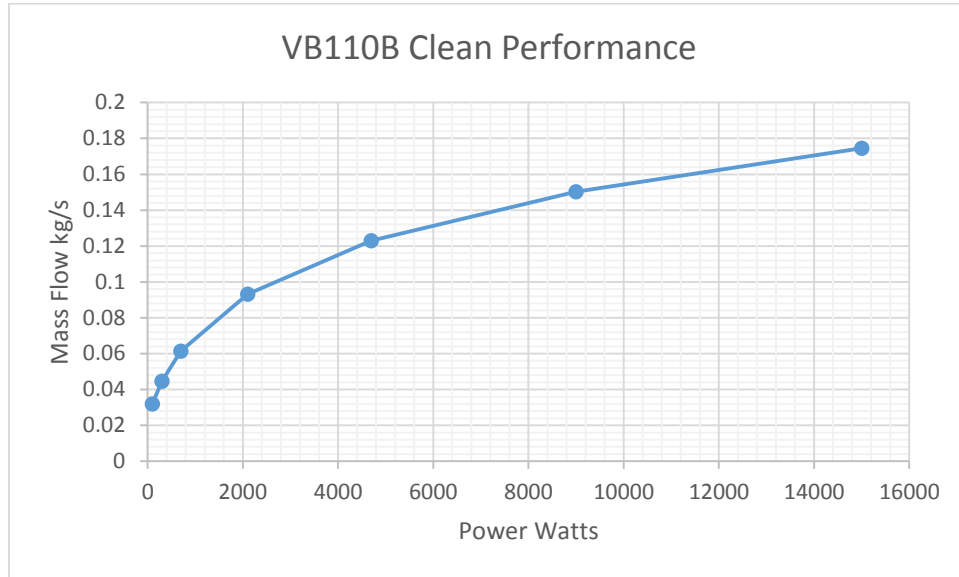


Figure 22 VB110B Blower Performance with clean configuration

The mass flow rate per power supplied by the Hitachi L300P 20Hp VFD is displayed in the above plot for the clean tube configuration with a porous thrust surface. The use of a VFD and differential manometer allowed for control of the mass flow rate without the use of a restrictor. It is also important to note that the exit temperature of the air rises with increased backpressure and VFD power as the blower/compressor is neither isentropic nor adiabatic process due to losses.

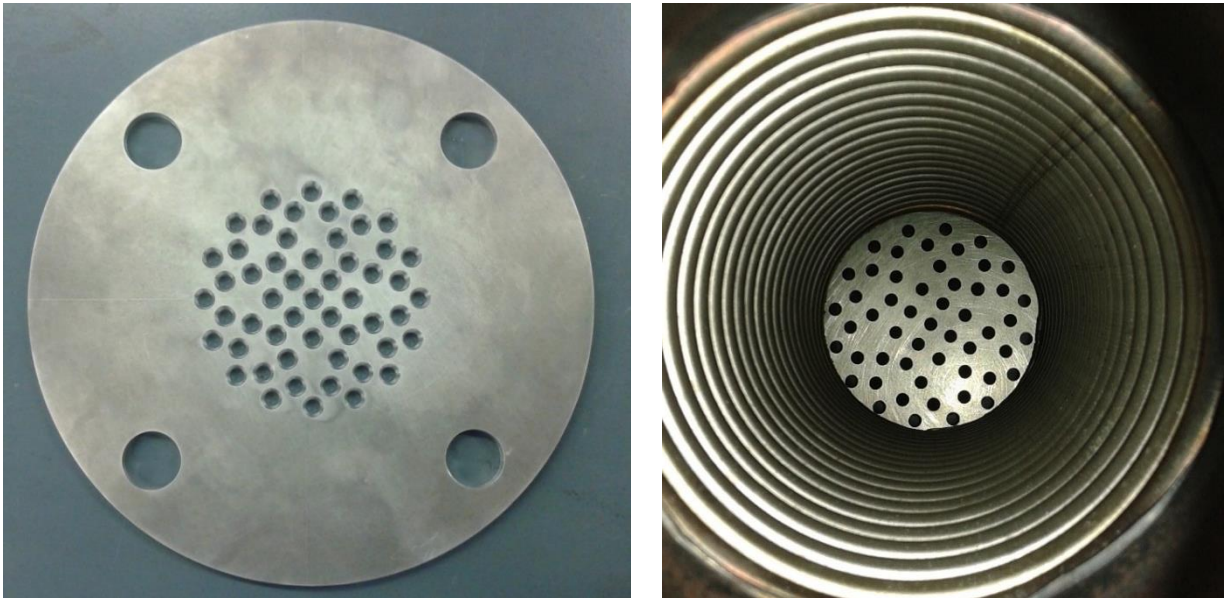


Figure 27 Porous Pressure Surface

The porous pressure surface consists of 53 $3/16$ " holes drilled using a radius center drill in a $1/4$ " AL6063 plate located at the 3" flange of the flex hose reducer (80% Blockage with respect to reducer). This method allowed for an even distribution of flow rate across the surface and minimize some loss due to the smooth profile of the individual nozzles in the downstream direction. Since the location of the plate was 10" in front of the reducing nozzle, it was assumed that perturbations and flow inconsistencies had enough time to attenuate and compress through the nozzle, leading to a uniform flow field before fuel injection.

With the porous thrust surface, mass flow is able to backflow during combustion and blowdown. The problem with a porous thrust surface is that it will impose a flow structure that will decrease the post shock pressure and possibly weaken the formation of the shock front, as studied by Cooper, Jewel and Shepherd in *The Effect of a Porous Thrust Surface on Detonation Tube Impulse*²⁶.

3.3.6 Venturi Flowmeter

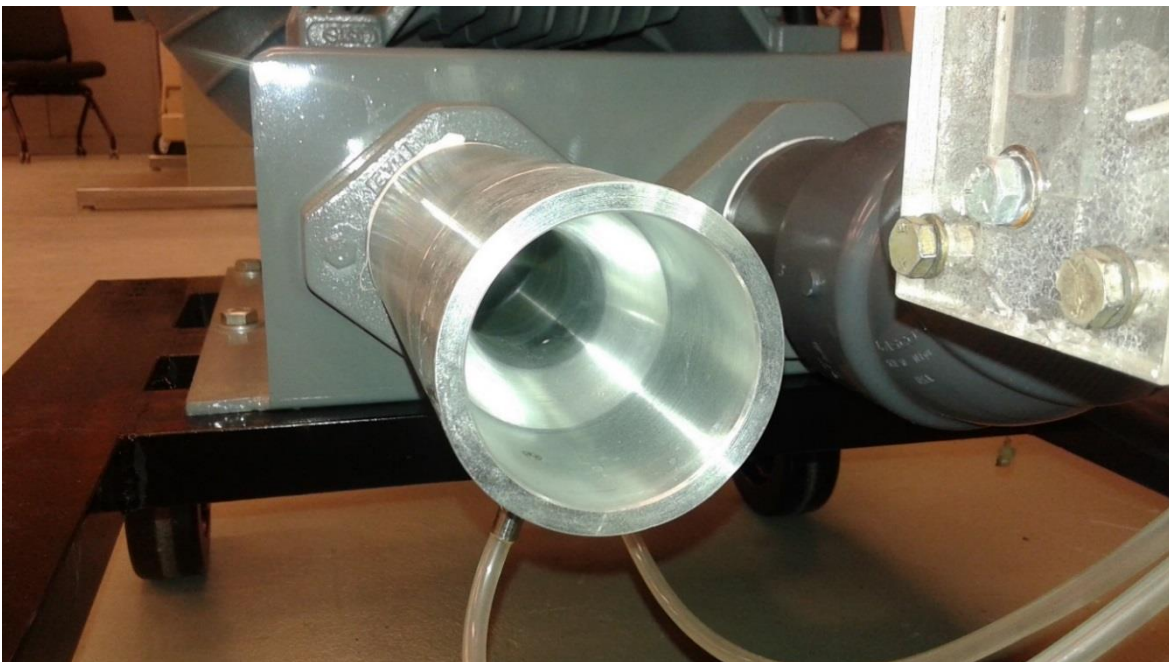


Figure 28 Venturi Flowmeter Installed

The venturi used for the study was manufactured out of AL2024 T6 stock with a 1.75” throat, internal diameter of 2.90” and an overall length of 10.00”, displayed in figure 27. A series of designs were evaluated using CFD, in order to check analytical predictions and estimate total pressure recovery. The 4th iteration displayed the best performance (in CFD) for pressure recovery while maintaining a moderately close differential pressure measurement to compressible 1D prediction.

3.3.6.1 CFD Study

The grid utilized for each trial consisted of a quarter cross-section containing 1.5M structured cells within the mesh. The boundary layer growth was started with a delta of 0.001” to capture the viscous effects along the wall and adaptive meshing at the surface was used to reduce the maximum Y^+ to a value less than 1. On average, using the static wall pressure at the boundary yielded 7.3-8.1% higher differential pressures between CFD and compressible predictions for the same mass flow rate.

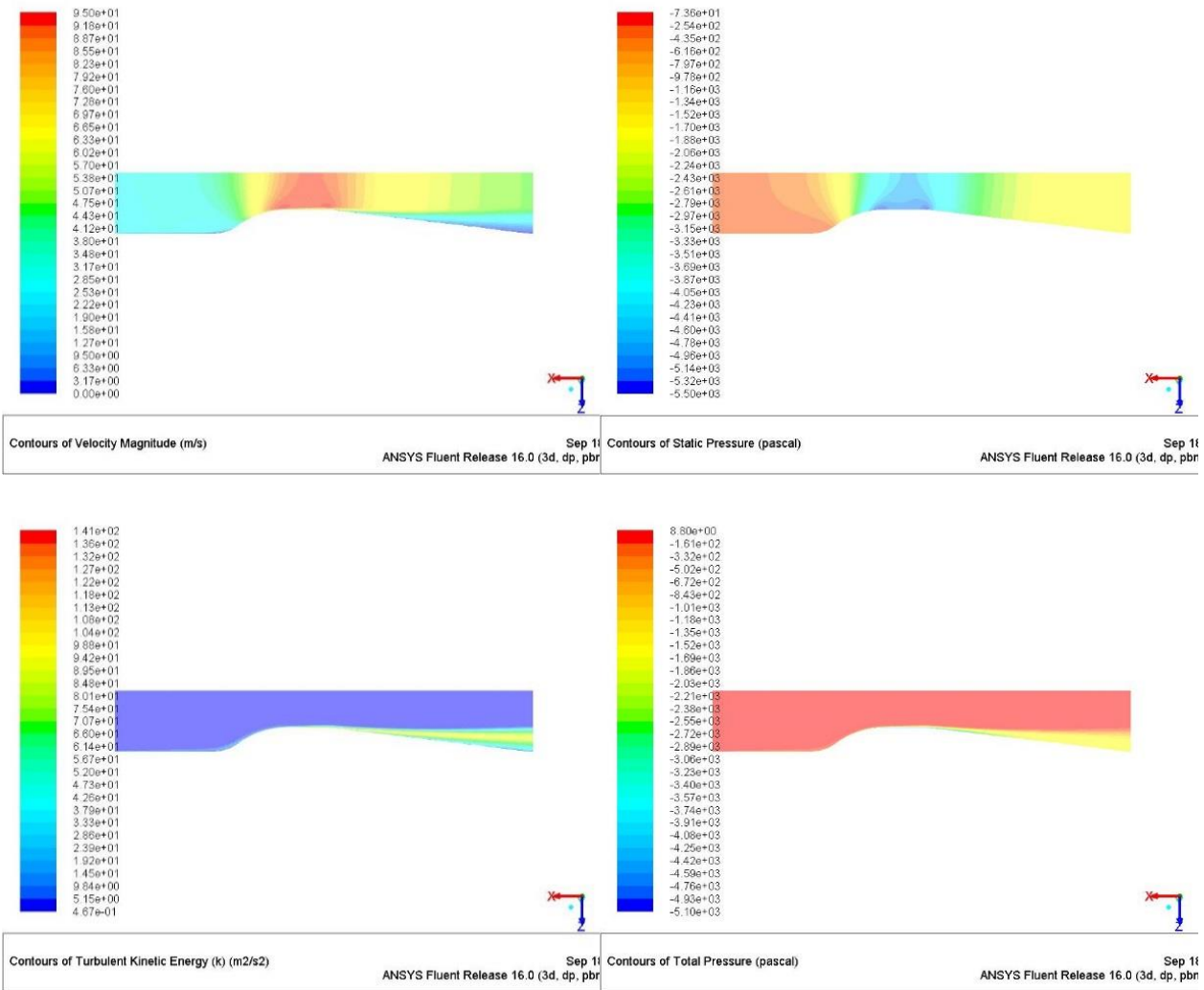


Figure 29 Venturi Flowmeter at 0.156 kg/s mass flow rate contour plots

As can be observed, losses and some separation are present within the diffuser segment. The theoretical total pressure recovery being 99.6% at a flow rate of 0.156 kg/s. This does not take into account inlet losses or separation. Losses and separation are located after the throat tap and will relatively leave the differential pressure measurements intact.

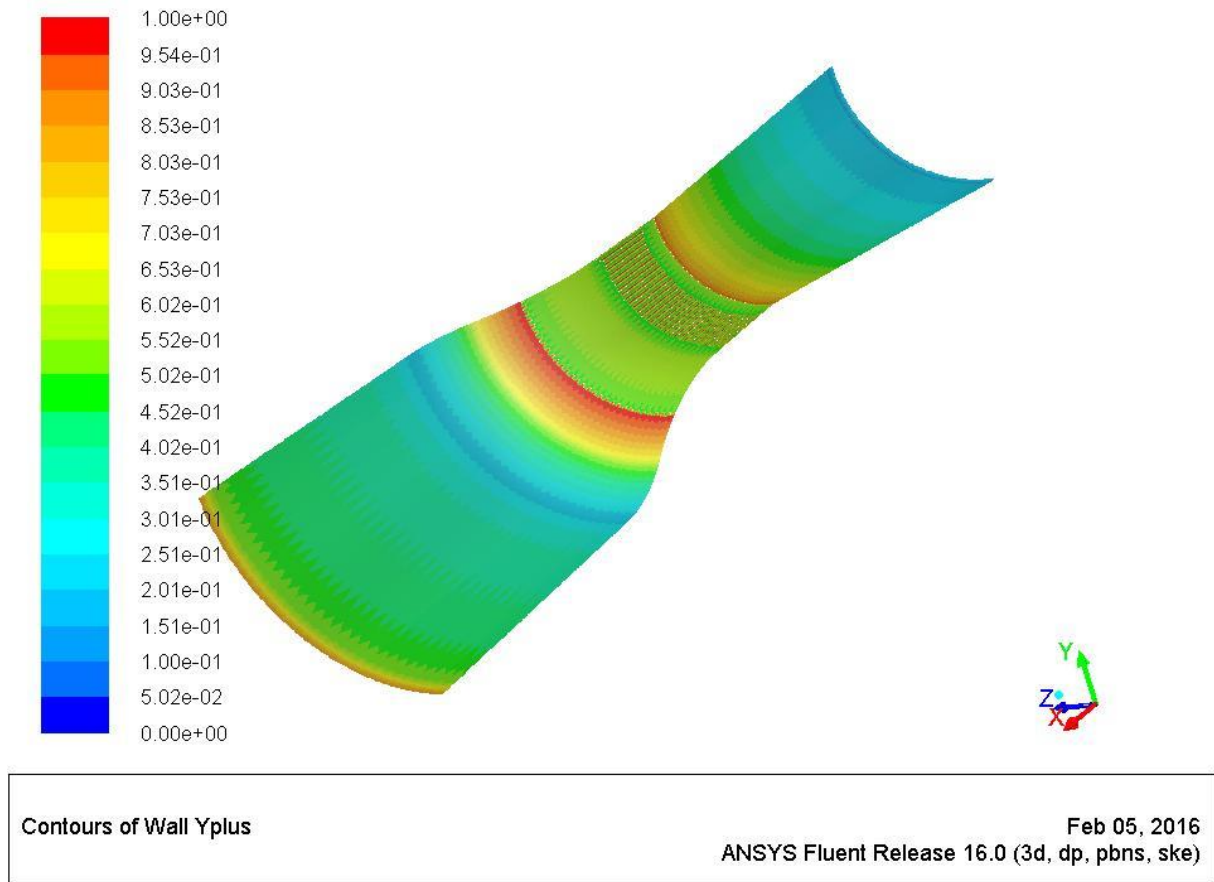


Figure 30 Venturi Flowmeter 0.156 kg/s Y plus

The above figure is a representation of the Y^+ for the structured grid of ~ 1.5 M cells after 2 rounds of grid adaptation. The initial cell growth was started at 0.001” with a growth rate of 10%.

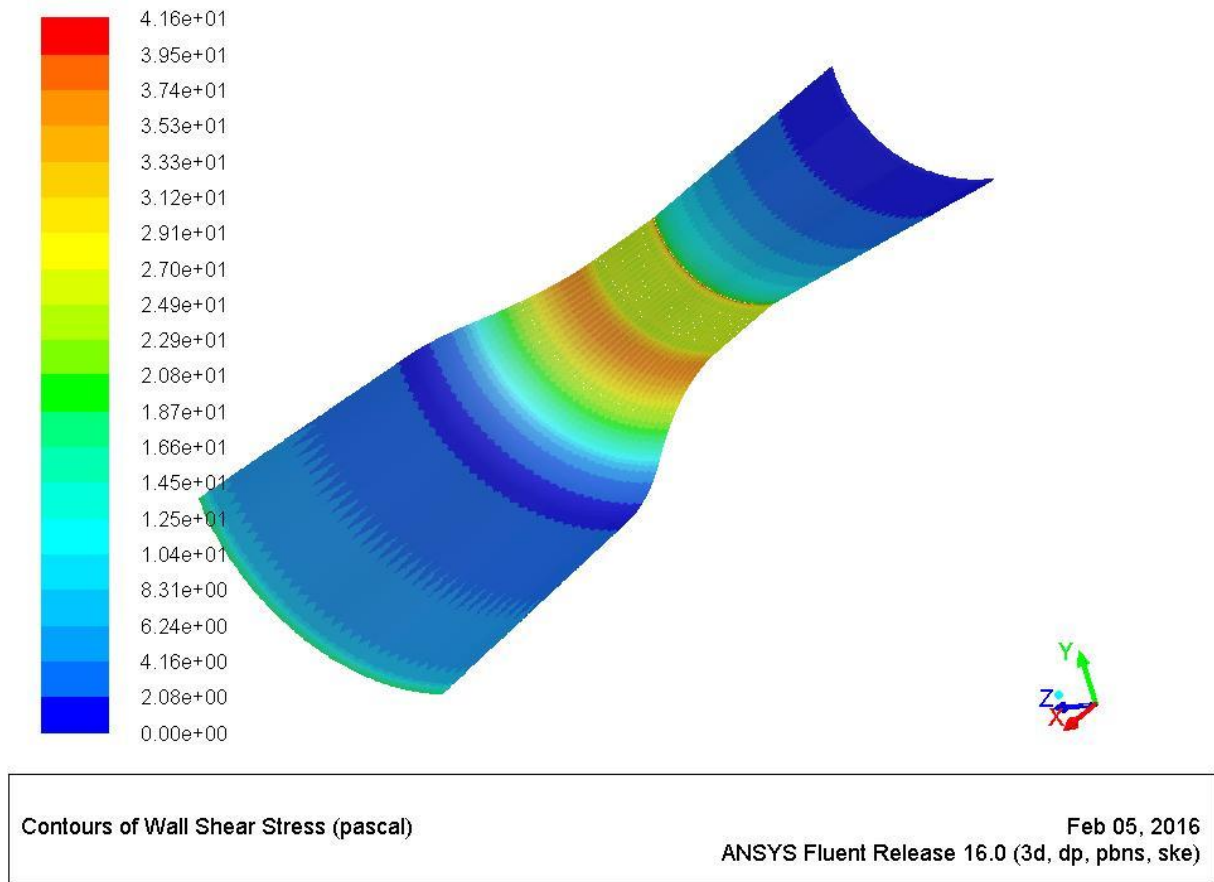


Figure 31 Venturi Flowmeter 0.156 kg/s wall shear stress

Inspection of the wall shear flow reveals a few interesting correlations with some of the localized pressure gradients and flow separation. The location of the high shear stress leading into the throat correlates well with the lower pressure regions and from the velocity contours the boundary layer thickness was reduced, causing the flow near the wall to accelerate.

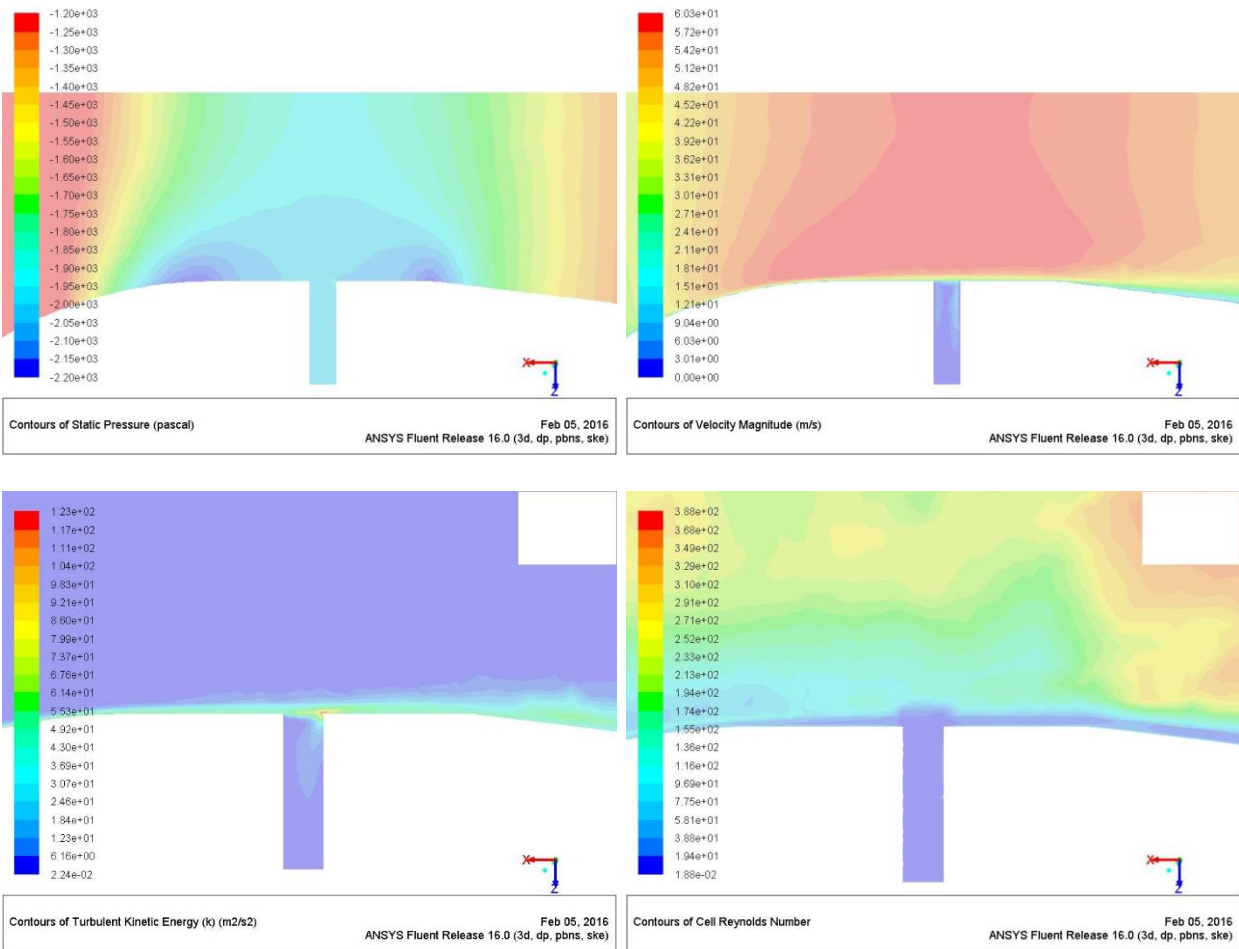


Figure 32 Unstructured Mesh with a mass flow rate of 0.052 kg/s examining the pressure and velocity at the throat tap location

A secondary mesh was generated to check the assumption that the wall static pressure is the same as the port going to the manometer while falling between the low pressure regions. An unstructured mesh with ports in place, once again, yielded the same results within 0.5% of the structured CFD studies and 7.3% higher differential pressure than the compressible predictions. Furthermore due to the port size being relatively small, having a diameter of 0.084", significant losses or flow deviations were not observed.

Due to limited resources and time constraints, the calibration of the venturi was primarily based off of the CFD predictions since it is grid independent, two models of turbulence agree and

the difference compared with the analytical compressible calculations was acceptable. The increase in differential pressure is expected to be higher in the real case and with CFD due to the boundary layer thickness decreasing the effective throat diameter.

3.3.6.2 Analytical Compressible Equations

The solution used to compute mass flow rate through the venturi during operation comprises of an iterative solution to a set of isentropic and adiabatic compressible equations. In order to help reduce the number of iterations the initial values are initialized with 1D incompressible calculations.

3.3.6.2.1 1D Incompressible

Step #1: Initialize values

$$\rho_1 v_1 A_1 = \rho_2 v_2 A_2$$

$$P_1 + \frac{1}{2} \rho_1 v_1^2 = P_2 + \frac{1}{2} \rho_2 v_2^2$$

Note: density is assumed constant and v_2 is substituted from the continuity equation in terms of areas and v_1 leading to the following solution. Density is first assumed to be ambient based on the ideal gas law. With A_1 and A_2 being the known physical parameters of the venturi flow meter.

$$v_1 = \sqrt{dP \frac{2}{\rho} \left[\left(\frac{A_1}{A_2} \right) - 1 \right]^{-1}}$$

$$M_1 = \frac{v_1}{a_1} = v_1 / \sqrt{\gamma R T_1}$$

3.3.6.2.2 1D Compressible Solution

Step #2: A_1 plane, inlet static pressure tap.

$$P_{o1} = P_o P R_1$$

$$T_{o1} = T_o$$

$$\rho_{o1} = \frac{P_{o1} MW_{air}}{Ru T_{o1}}$$

$$T_1 = T_{o1} \left[1 + \left(\frac{\gamma - 1}{2} \right) M_1^2 \right]^{-1}$$

$$P_1 = P_{o1} \left[1 + \left(\frac{\gamma - 1}{2} \right) M_1^2 \right]^{-\frac{\gamma}{\gamma - 1}}$$

$$\rho_1 = \frac{P_1 MW_{air}}{Ru T_1}$$

$$a_1 = \sqrt{\gamma R T_1}$$

$$\dot{m}_1 = \rho_1 M_1 a_1 A_1$$

Step #3: A₂ plane, throat static pressure tap

$$P_2 = P_1 - dP$$

$$P_{o2} = P_{o1} P R_2$$

$$T_{o2} = T_{o1}$$

$$M_2 = \sqrt{\frac{2}{\gamma - 1} \left[\left(\frac{P_{o2}}{P_1} \right)^2 - 1 \right]}$$

$$T_2 = T_{o2} \left[1 + \left(\frac{\gamma - 1}{2} \right) M_2^2 \right]^{-1}$$

$$\rho_2 = \frac{P_2 MW_{air}}{Ru T_2}$$

$$a_2 = \sqrt{\gamma R T_2}$$

$$\dot{m}_2 = \rho_2 M_2 a_2 A_2$$

Step #4: Iterative comparison. Loop to step #2 and update M₁ until the desired discrepancy between the mass flows is within 0.1 g/s. This usually takes 5-20 iterations for convergence.

$$M_{1\text{ new}} = \frac{1}{2} \frac{2\dot{m}_2 - \dot{m}_1}{\rho_1 a_1 A_1}$$

3.3.6.3 Corrections to Compressible

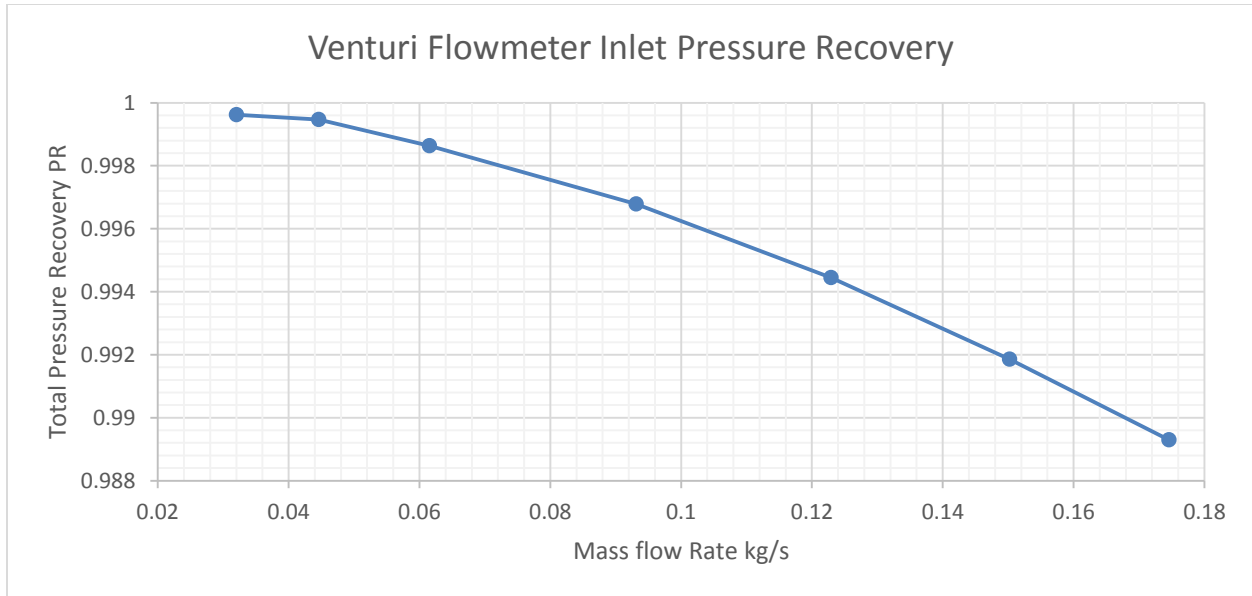


Figure 33 Venturi Flowmeter Inlet Pressure Recovery

Corrections for total pressure losses and measured differential pressure are below for reference. The PR_1 function is a curve fit equation from measured data to compensate for the total pressure loss from the ambient room pressure to the total pressure located at the first tap. The second PR_2 is derived from CFD and is the pressure loss at the throat of the venturi from the first tap and is already compensated for by shifting the differential pressure measurement based upon a curve fit equation to match the compressible predictions to the CFD results.

$$PR_1(\dot{m}_1) = 1.000 - 0.3468\dot{m}_1^2 - 0.00151\dot{m}_1$$

$$PR_2(\dot{m}_2) = 1$$

The measured differential pressure was corrected to match it to the CFD results to compensate for boundary layer effects, allowing for improved accuracy of mass flow rate. It must

be noted, that this correction is from CFD studies and the result was found to be grid independent; the same was true for multiple turbulent dissipation models.

$$dP = dP_{measured}(1 - 0.04765\dot{m}^{-0.24023})$$

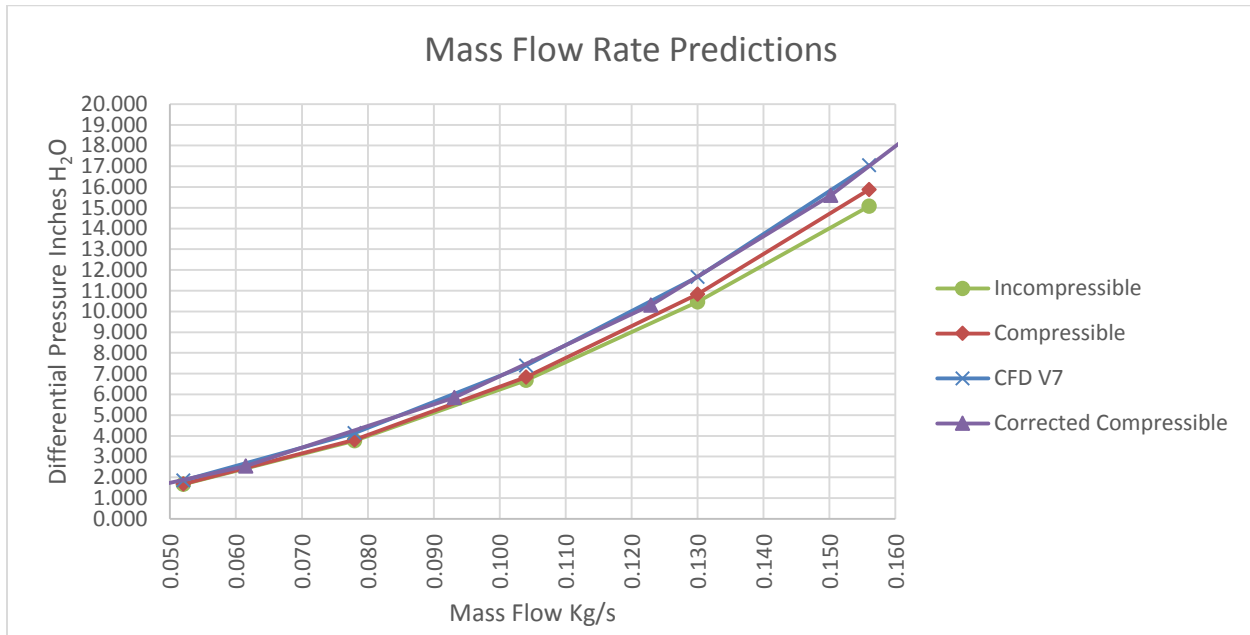


Figure 34 Venturi Flowmeter mass flow rate predictions

The above plot represents the various methods of acquiring the mass flow rate through the flow meter as a function of differential pressure. The first method plotted is incompressible, the method used for initialization which assumes isentropic, adiabatic and constant density. The compressible method displays a higher differential pressure, especially at higher flow rates as would be expected. CFD results display the highest differential pressure in comparison to the 1D idealized methods; however, results are within 8% for all models utilized. The primary reason for the higher pressure is boundary layer effects and localized pressure gradients near the throat.

4 Results and Discussion

4.1 Phase 1: Physical Obstacle Testing

Five configurations were successfully tested for two equivalence ratios. A representation of the configurations can be found below for visual comparison.

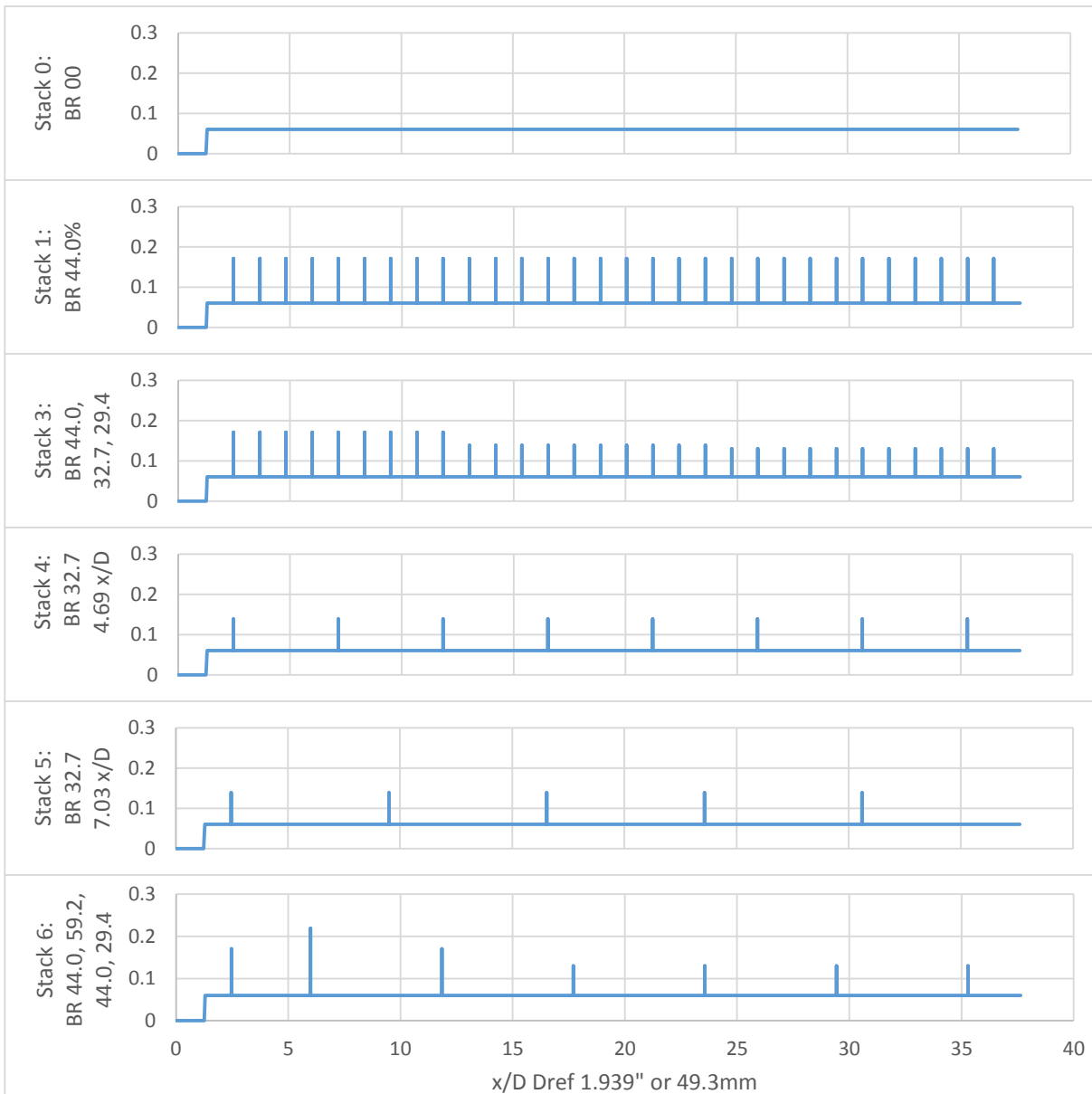


Figure 35 Phase 1 Physical DDT Stacks, Cross Section of 0.0 is wall and 0.5 is centerline

4.1.1 Full Stack Representative Raw Data

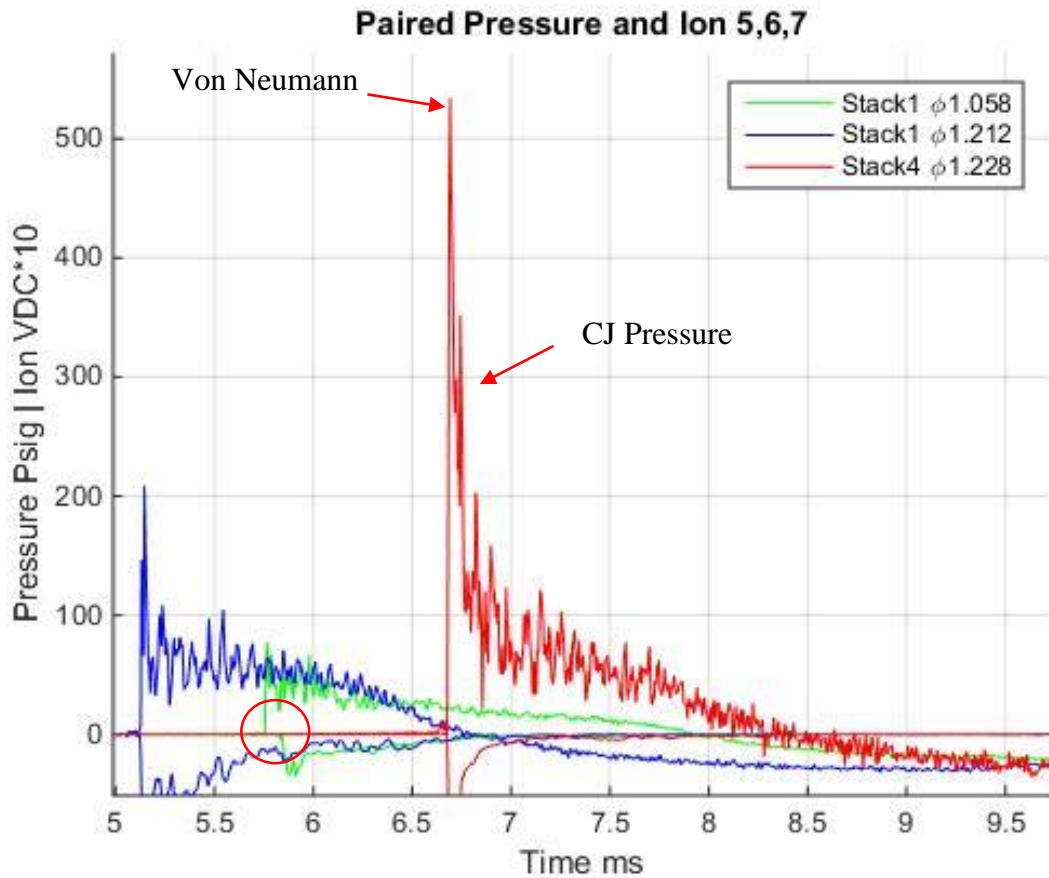


Figure 36 Representative Raw Data of Stacks 1, 4 at station #7

The near Stoichiometric Stack 1 case is a deflagration flame front displaying some time separation between the pressure wave and flame front (green). The higher equivalence stack 1 is in the process of transitioning to detonation. It was not fully achieved due to the pressure not reaching CJ pressure of nearly 280 psi (blue). Stack 4 is a good example of a fully developed detonation wave. The max pressure attained is the Von Neumann pressure spike and the first small plateau of pressure corresponds to the CJ detonation wave pressure, also not the coincidence of the flame and shock detection near 6.7 ms. The falling of the pressure history is the result of the products expanding to the choked condition in the flow stream and the blowdown of products.

4.1.2 Full Stack Condensed Information

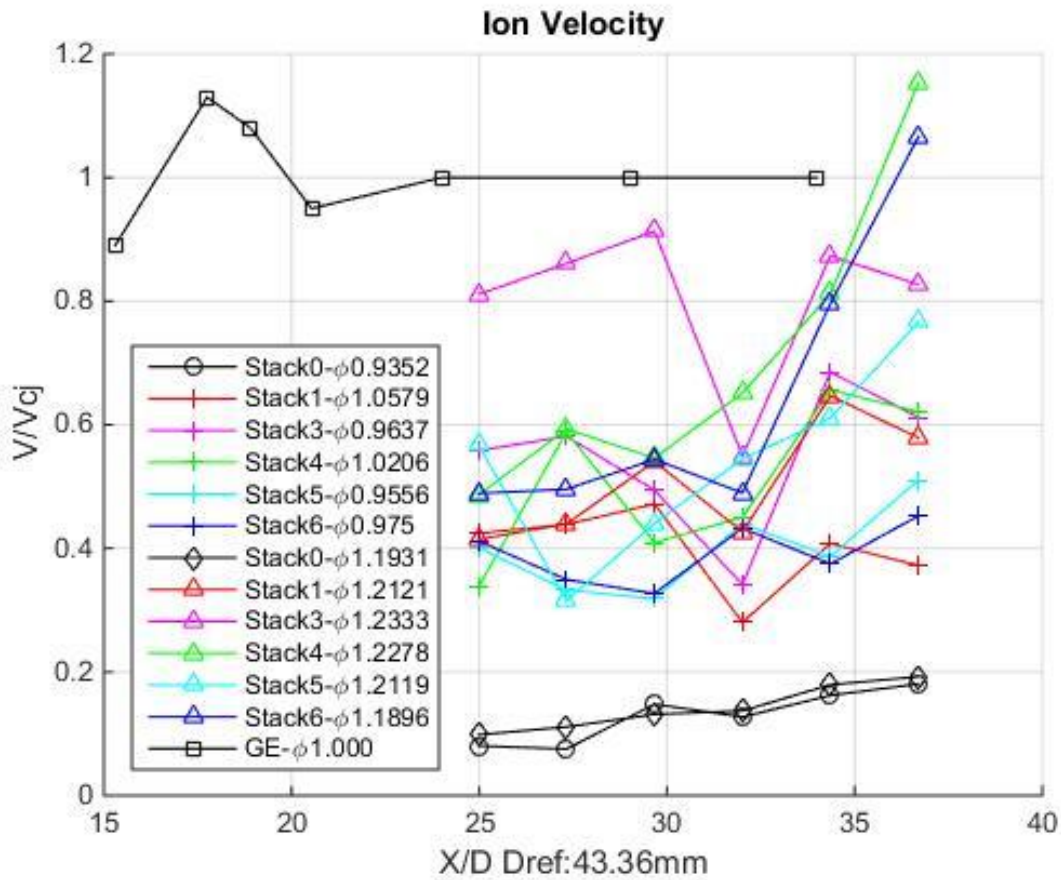


Figure 37 Nondimensional Velocity of Physical DDT Stacks $M_{air} 0.0539 \text{ kg/s}$

Figure 36, Flame velocity attained within the Diagnostic test section. As from observation many cases did not reach the detonation was speed, cases under V/V_{CJ} of 1.0. The best performing cases being Stack 3, 4 and 6. Stack 3 is a diverging obstacle case with a separation of $1.17 x/D$, stack 4 is constant spacing constant blockage of BR 32.7 and $4.69 x/D$ and Stack 6 is a convergent divergent with variable spacing. The highest exit velocities belong to the cases with the least obstructive obstacles in the diagnostic section. For several cases and locations indicating velocities under theoretical, detonation success was achieved by further examining the time history of the flame and pressure response. In general, excessive obstacles can hinder flame and wave speed.

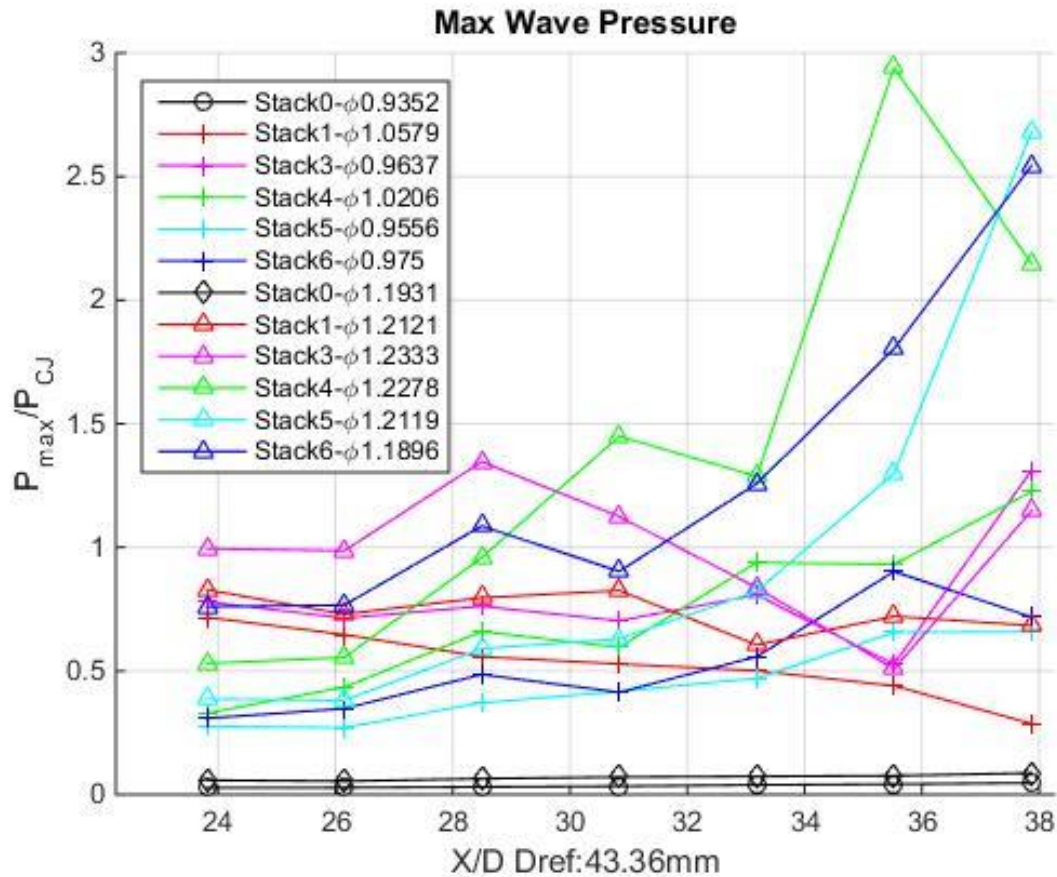


Figure 38 Nondimensional Pressure of Physical DDT Stacks $M_{air} 0.0539 \text{ kg/s}$

The above plot of pressure ratio with respect to the Chapman-Jouguet pressure is a good indication if detonation was achieved for cases greater than 1. Noting that for $\Phi 1.23$ and stacks 4, 5 and 6, displaying average pressures well beyond the CJ value, indicates one of two items. First the possibility of an overdriven detonation wave which is unstable, or more than likely the detection of the Von Neumann pressure spike. In the above cases it is the Von Neumann pressure spike as the velocity is near V_{CJ} . This pressure spike, not captured by CJ Theory is well approximated by applying the normal shock relations as in the ZND model and corresponds rather well.

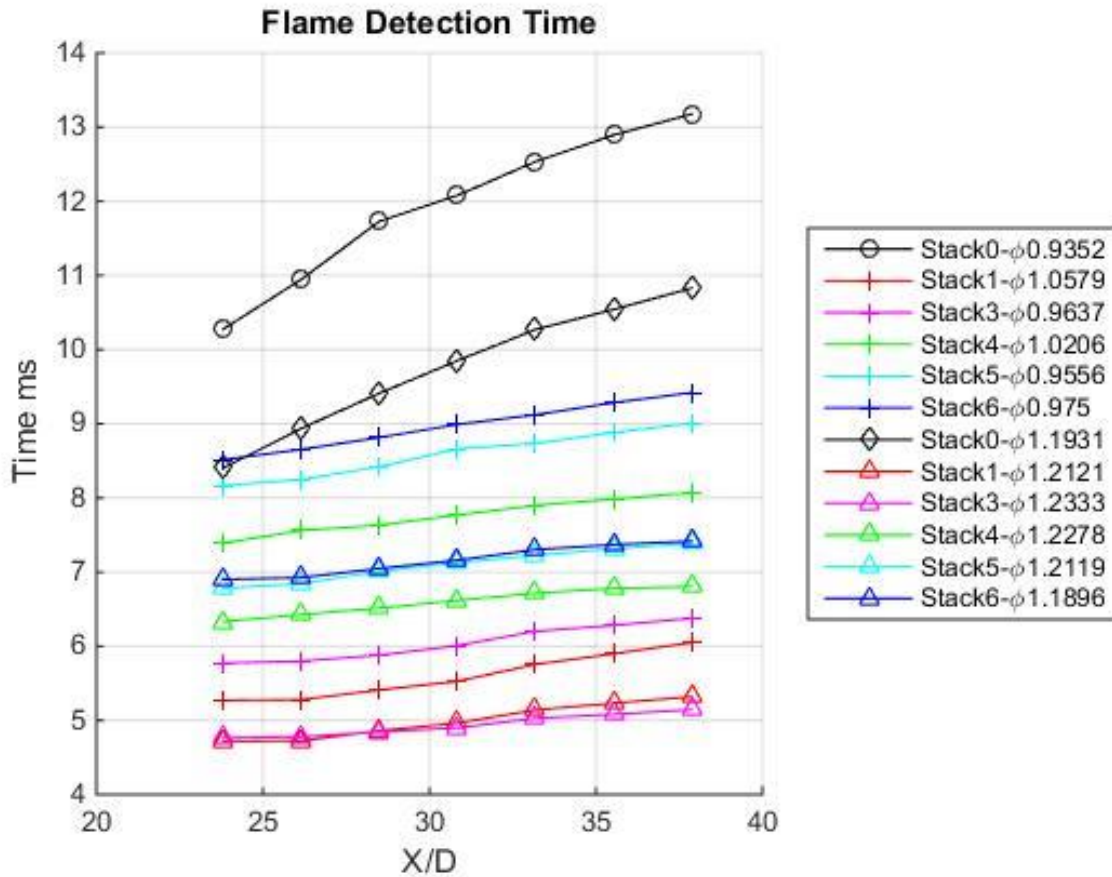


Figure 39 Flame Detection Time of Physical DDT Stacks 0.0539kg/s

The detection time between the configurations is rather interesting in figure 39. Stacks 1 and 3 have the highest obstacle densities of all configurations with only a 1.17 x/D separation between each while the others vary greatly (bottom two data lines for the higher equivalence ratios). Overall it is expected that the higher fuel air mixtures display a reduction in time from their stoichiometric counterparts due to the heat release and chemical reaction rate being higher.

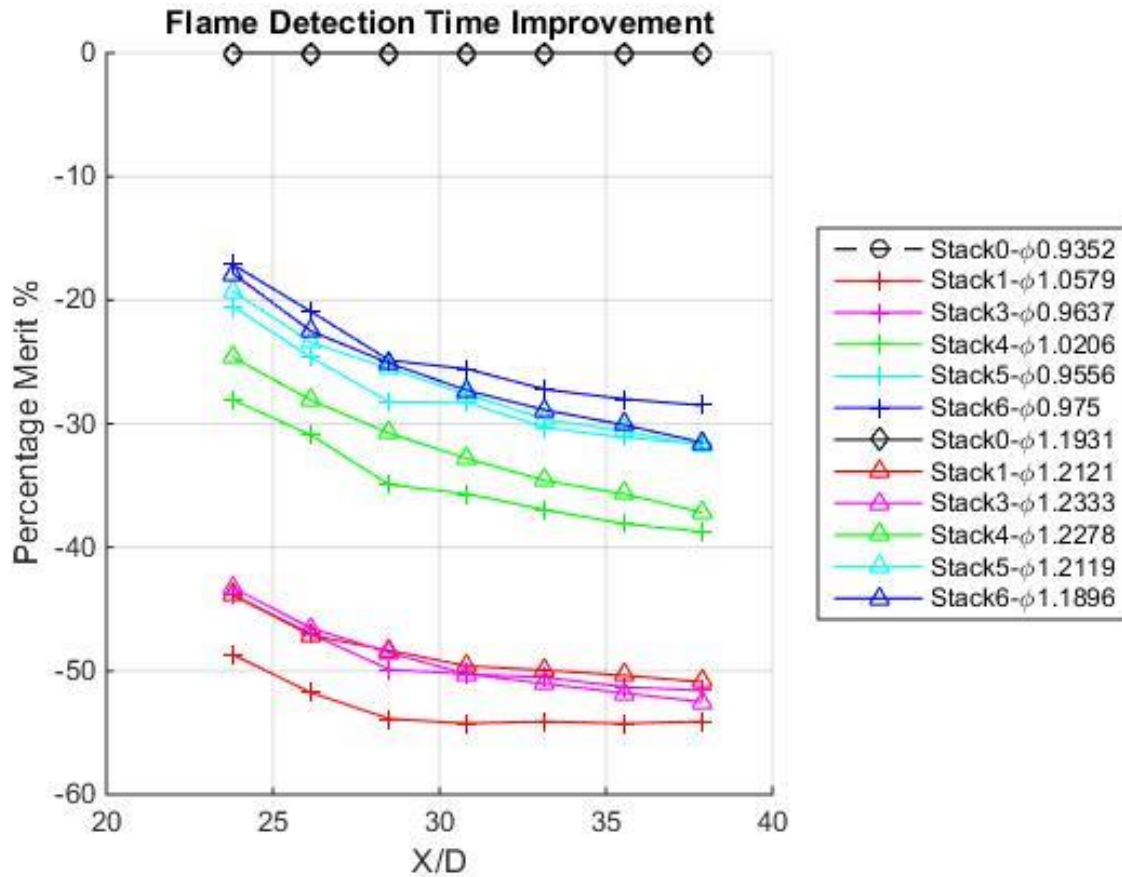


Figure 40 Flame Detection Improvement over Baseline, Physical DDT Stacks M_{air} 0.0539 kg/s

Observing the performance increase over the appropriate baselines in figure 40, it is clear that the flame accelerates quickly in the section leading to the diagnostic section while still maintaining in several cases comparable velocities in the diagnostic section overall. It can easily be stated that the high density of obstacles aids flame acceleration in the early stages; however, the configurations with fewer obstacles achieve higher exit velocities due to the unnecessary flow restriction slowing the flame and wave fronts. Observing the slopes after x/D of 32, Stacks 4, 5 and 6 display the highest velocities. These configurations impose the least amount of flow obstruction in the DDT section.

Table 6 DDT Stack Pressure Loss

Stack #	Pressure Loss		
	Pa	Psig	%
Stack 0	2055	0.298	2.05
Stack 1	26681	3.870	26.66
Stack 3	17267	2.504	17.25
Stack 4	6636	0.962	6.63
Stack 5	5313	0.771	5.31
Stack 6	9267	1.344	9.26

The above table contains the required static head pressure required differential to drive a set mass flow rate of 0.0539kg/s of air through the obstacles with an ambient pressure of 14.514 psi. Noting for the configuration with the highest number of obstacles, Stacks 1 and 3, they display the highest losses. Stack 1 contains uniformly spaced 44% BR obstacles while Stack 3 uses a diverging series beginning with 44% BR and reduces to 29% BR over the length.

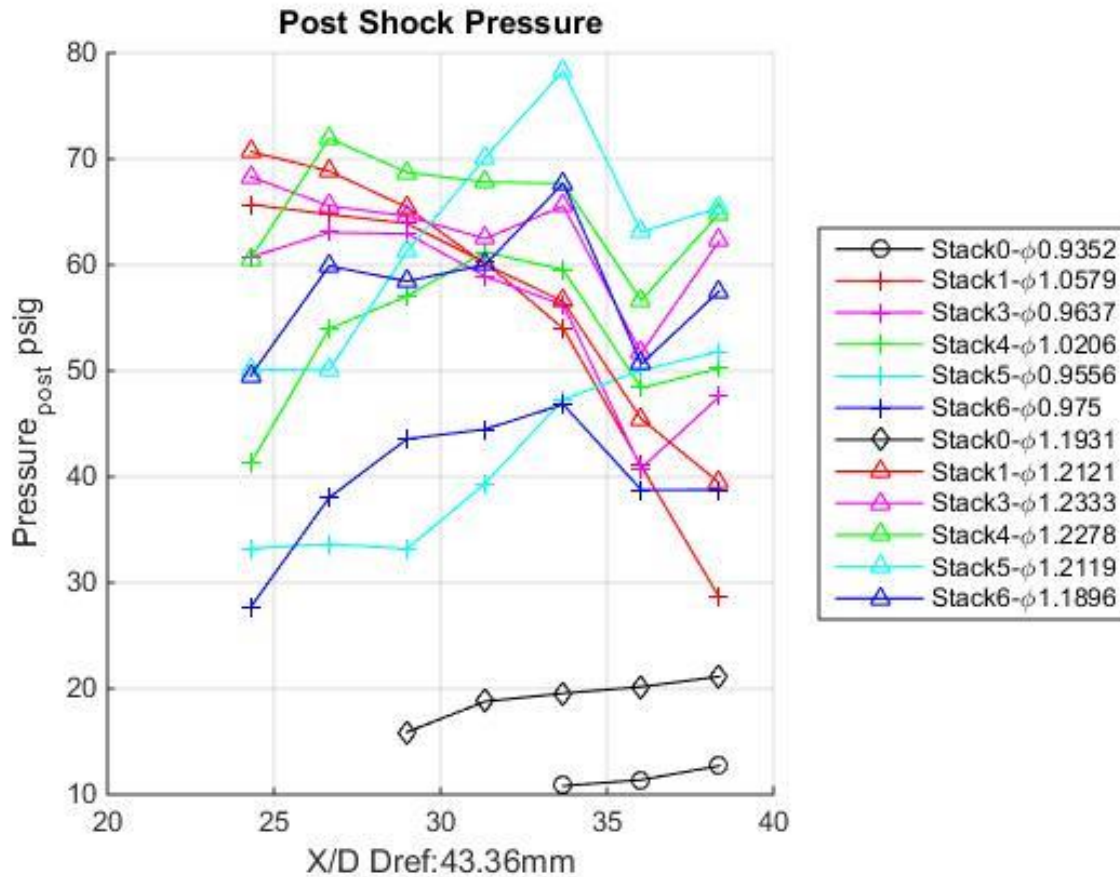


Figure 41 Post Pressure of Physical DDT Stacks 0.0539kg/s

The post shock static pressure was averaged over 0.70 ms after the products have expanded and accelerated to the sonic velocity in the product stream, displayed in figure 40. The importance of this metric is to quantify the effectiveness of the pressure rise in the combustion chamber; however, the products if subjected to additional flow restriction, as in some of the cases, will not be fully accelerated due to the choked conditions of the additional blockages and not the clean inner diameter. It must also be noted, that due to the porous thrust surface in a clean tube configuration with a 36% BR (respect to inner diameter of the spacer 1.707" and open area of the porous thrust surface), and it is not expected to reach the same post shock pressure plateau as the valve configuration²⁶. However, the successful stacks achieving DDT displayed pressures congruent to tests with no backflow and even exceeding it slightly. The implication strengthens

the case for localized pressure surfaces to help the favorable pressure gradient during blowdown; if the application uses a porous thrust surface with insufficient fuel and air total pressure needed for stagnation^{19, 28}.

A direct comparison being made for stacks 4 and 5 examining the impact of the fuel and air delivery scheme. The valve configuration used by Gagnon is the exact setup sharing the hardware of the DDT section and supplied in 3 locations with the use of 7 AFS GS60 gaseous fuel solenoid valves³⁰. The estimated Φ of 1.30 was utilized for the valve configuration whereas the valveless utilized Φ 1.22.

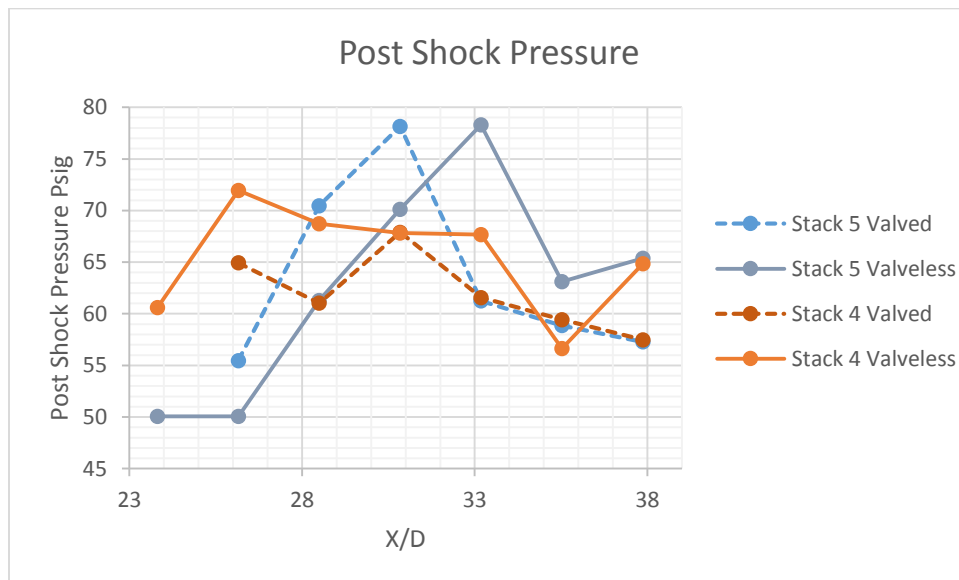


Figure 42 Refill Method Comparisons, Post Shock Pressure

As can be observed the valveless case with a porous thrust surface is near the valve configuration post shock pressure in figure 42. The post shock plateau pressure is seemingly unaffected with the use of plentiful obstacles upstream, albeit a slight axial increase for stack 5.

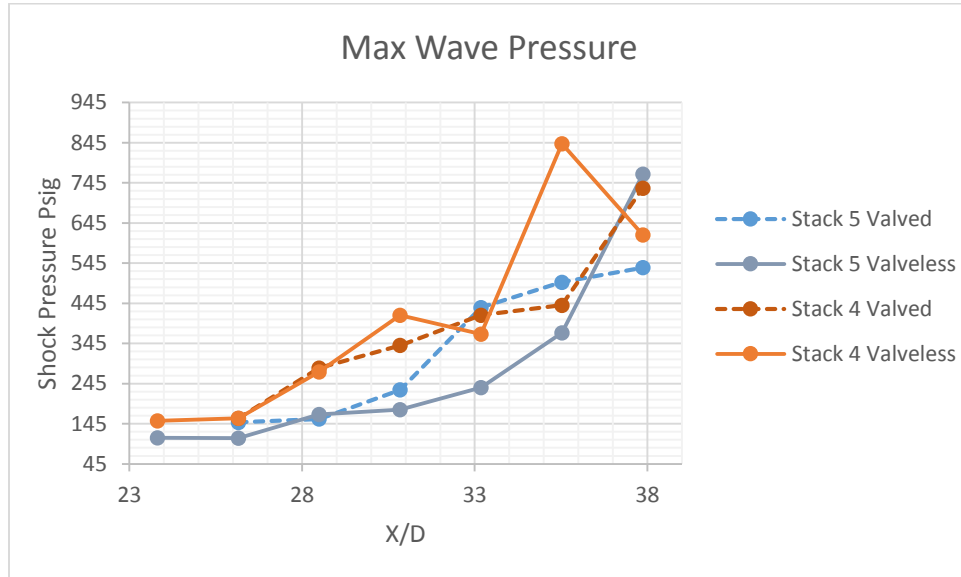


Figure 43 Refill Method Comparisons, Wave Pressure

The pressure trends between the injection schemes are also close in figure 43. The majority of the standard deviations are around 100psi. Given the spread, it is reasonable to draw several conclusions and state the pressure wave achieved is not affected by filling velocity or the porous thrust surface to a great extent with plentiful obstacles. The case with the fewest number of obstacles upstream, stack 5, displayed a meaningful reduction until the later transition section requiring an additional orifice.

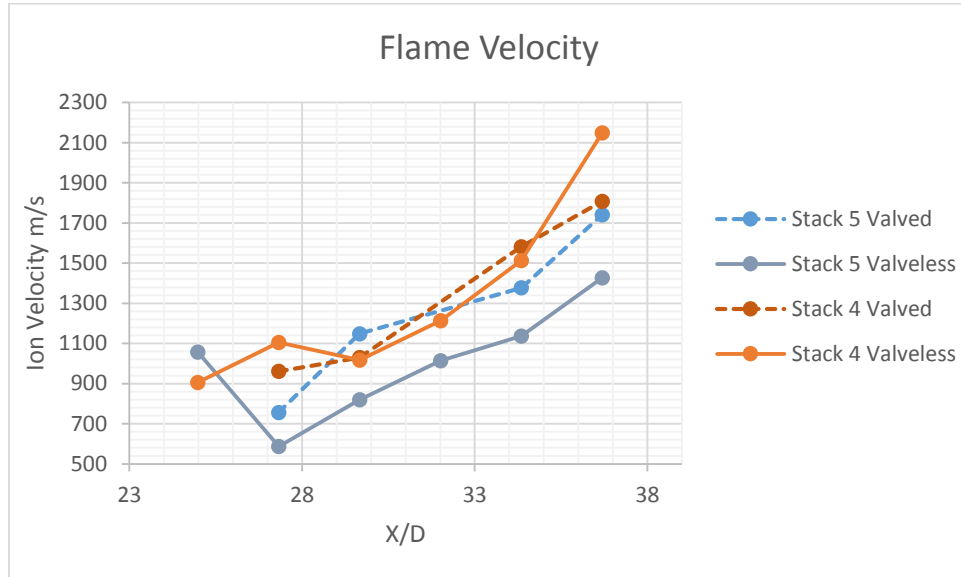


Figure 44 Refill Method Comparisons, Flame Velocity

Flame velocity for Stack 5, BR 32.7 and 7.03 X/D, the least densely packed case displaying velocity reductions in comparison to the valve scheme. In general, the valveless supply with a porous thrust surface serves to decrease multiple performance parameters; however, the use of frequent physical obstacles appears to significantly decrease the backflow, alleviating the expected reductions in post shock pressures and flame velocities.

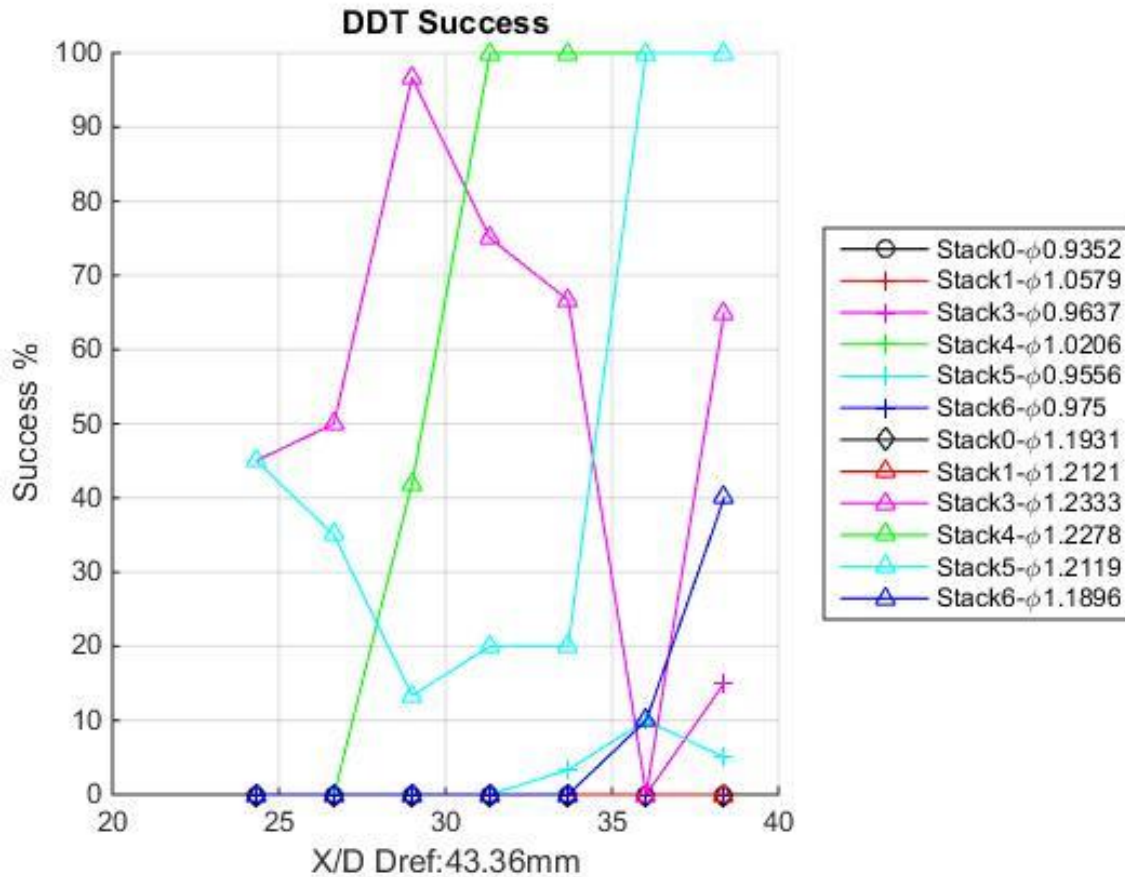


Figure 45 DDT Success for Physical DDT Stacks

Drawing trends from the DDT success and Post shock pressure, even without achieving detonation, the pressure gain is significant as long as fast deflagration is achieved. Another primary concern of not achieving detonation is the possibility of wasting the unburned reactants that exhaust before being consumed, i.e., emissions, wasted fuel, and possibility burning reactants in the turbine section.

In general, the testing with moving mixtures for Stack 4 (CSCB.A.4) and Stack 5 (CSCB.C.6) from Gagnon's studies correlates remarkably well³⁰, displaying similar trends and performance in attained pressure, ion velocity and detonation success. This in effect is a one to one comparison of verifying the rigs performance of using a valveless scheme to a valve configuration with the same test section.

4.1.3 General Electric Trial Reproduction

The reproduction of General Electric’s trial displayed a failure to transition to detonation reliably for equivalence ratios of 1.00 and 1.23 in a comparable non-dimensional lengths. It must be noted that the geometry differs in several respects.

Table 7 Physical Differences between GE and Reproduction Trial

	GE	ERAU
Inner Diameter	51.0 mm	43.3 mm
Spacing Between	50.8 mm	50.8 mm
Blockage Ratio	43%	44%

ERAU’s test rig was 27.9% smaller in cross-sectional area and the physical obstacles retard the transition, as the average flame velocity only reached 760 m/s, 40% of the Detonation Velocity, and few configurations achieved detonation pressure and V_{CJ} . This was not wholly unexpected as similar trends were observed in Christopher Tate’s experiments in quasi static mixtures⁸. The cell size being near 22mm, approximately 53% of the inner tube diameter and 70% of the orifice, may be close enough to collapse the detonation wave structure and keep it from fully forming as observed.

4.2 Phase 2: Single Orifice Tests

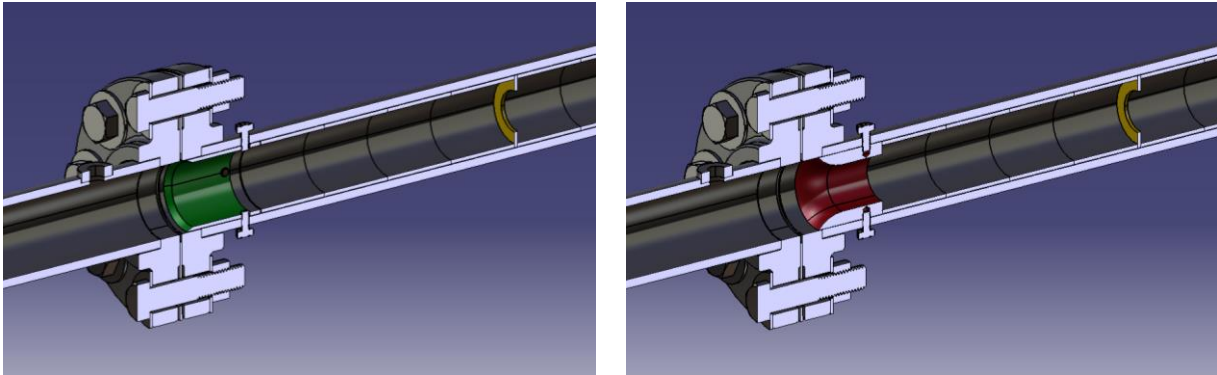


Figure 46 Phase 2 Testing Configurations

The above figure displays a section cut of the single orifice configurations. The Left image is the single orifice trial, right is the combined single orifice with the low loss bluff body. The gold washer is the simple blockage inserted into the flow on the same plane of JICF0# injection, 24.5" downstream of the fuel injection port location. The spacers used to locate the orifice reduce the inner diameter from 1.939" to 1.707" and filled half the test section. The diagnostic array maintains the inner diameter of 1.939".

4.2.1 Representative Raw Data

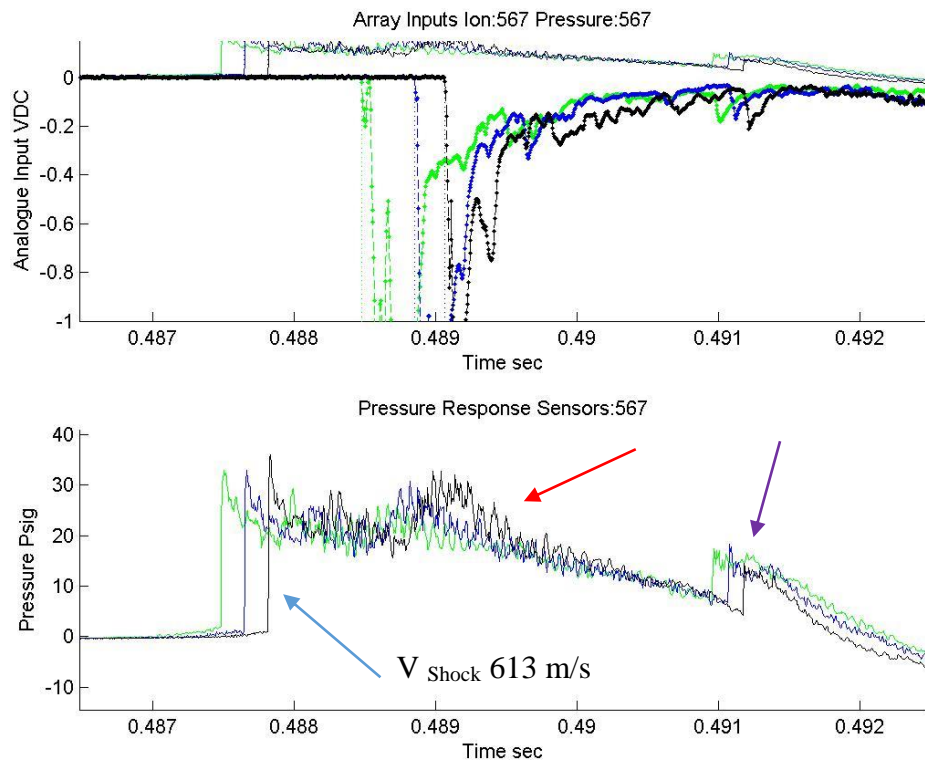


Figure 47 Raw Data of Combined BR03 at Φ 1.2516 Mass Air 0.0539 kg/s

The above figure is the raw data from pair 5, 6 and 7 towards the aft of the diagnostic section. The drop in voltage is the time of spark discharge and as observed does not excite harmonics in the system. The dominant feature of this configuration is a leading pressure wave traveling at 613 m/s or nearly Mach 1.77 with a pressure of 36-40psi agreeing fairly well with theory. The post shock pressure is less than expected by 30%, and likely due to the porous thrust surface allowing some backflow. The second slight rise in pressure, indicated by the red arrow, corresponds with the flame front and is a result of associated heating and expansion. The third is a reflection from the upstream perforated pressure plate, highlighted by the purple arrow.

4.2.2 Equivalence 2 Compiled Data

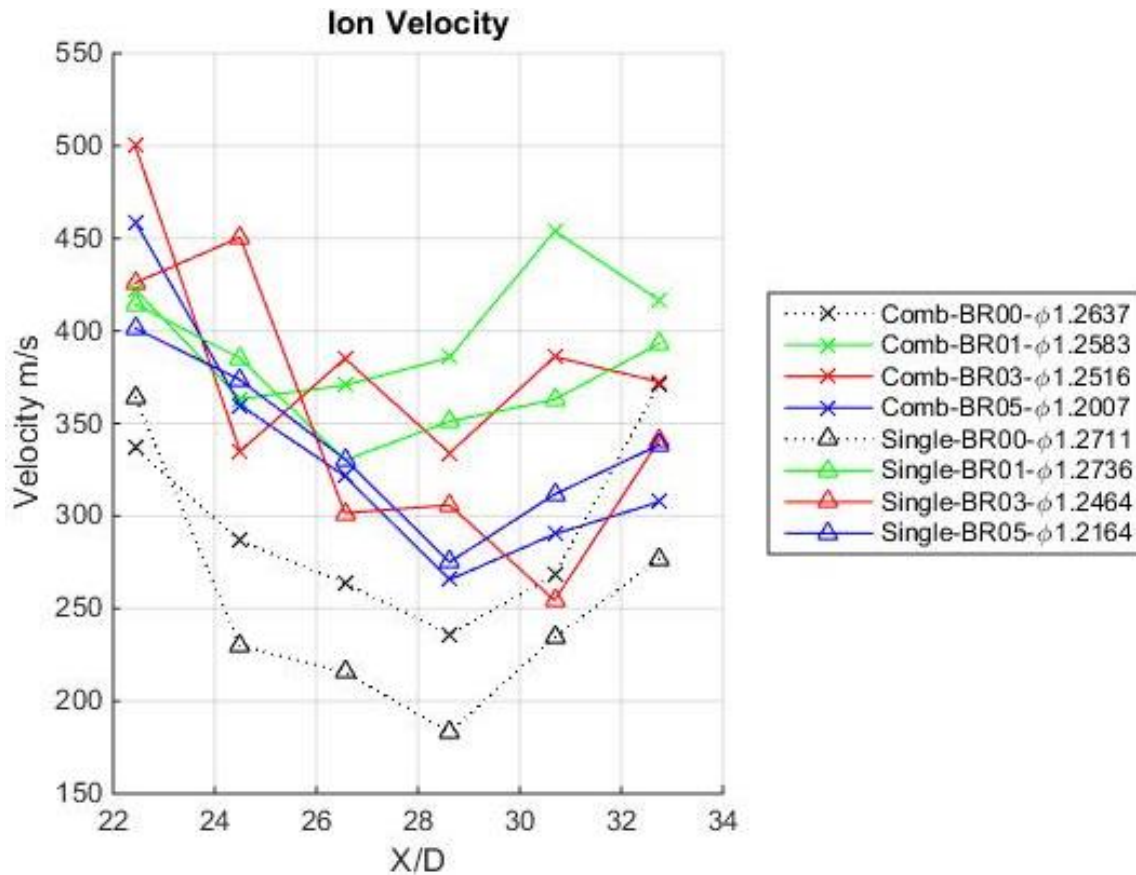


Figure 48 Ion Velocity of Single and Combined BRs at Φ 1.25 Mass Air 0.0543 kg/s

The velocity displayed in the above figure shows a few interesting trends. The first trend for all configurations is the U shaped velocity profile. The flame front acceleration is initially negative entering the diagnostic section before it rises at the end. This is most likely due to an area change of 29% leading into the diagnostic section from the front transition section due to the use of the retaining spacers. Furthermore, flame front velocity is a function of blockage ratio; however, this relation is nonlinear as the flame velocity drops at the highest blockage utilized. Lastly, the bluff body does not display the same acceleration as the BR03 blockage. This may be due to the location of the bluff body being 10" upstream of the JICF location where the flame kernel has most likely not fully developed. Overall it is important to note that the standard deviations range from

45m/s to 160 m/s so the uncertainty is roughly on the same order as the difference between the tests.

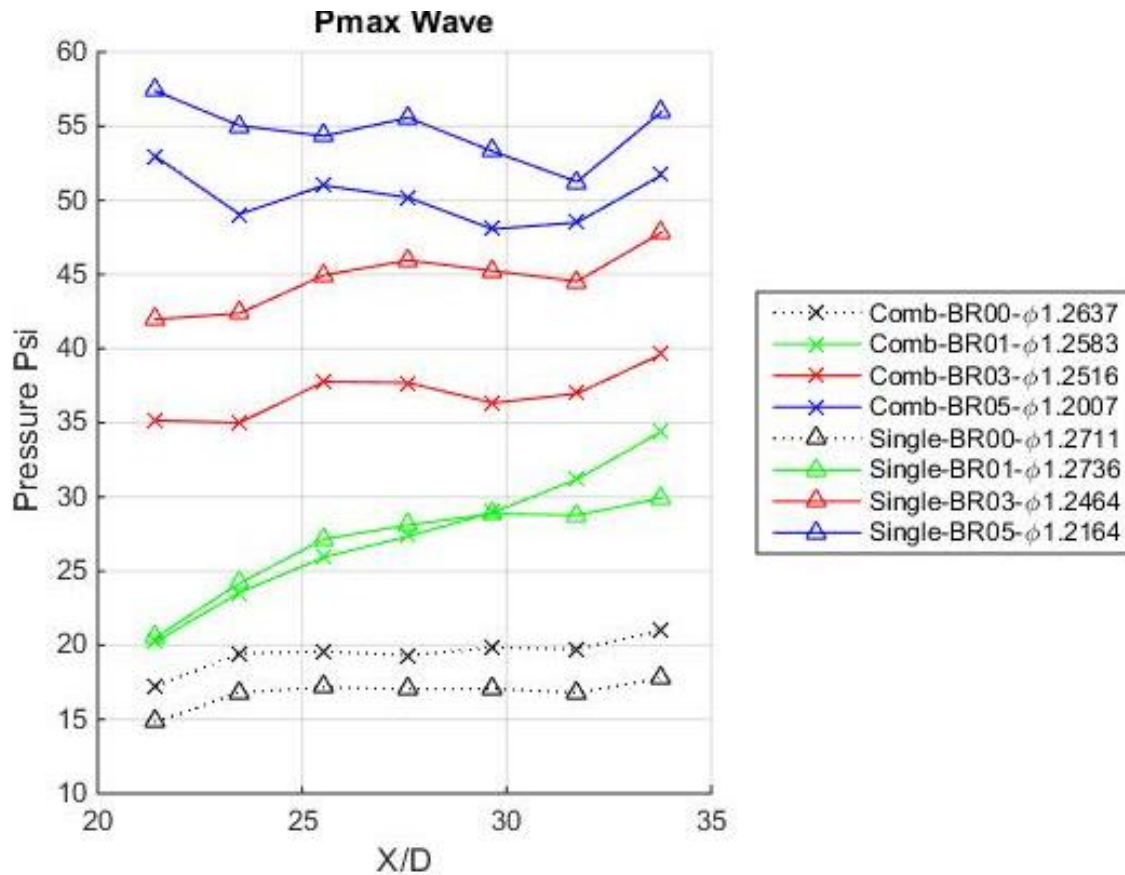


Figure 49 Max Pressure of Single and Combined BRs at Φ 1.2516 Mass Air 0.0543 kg/s

The pressure developed within the combustion chamber indicates a strong correlation to the blockage ratio, and the bluff body addition is not entirely favorable in figure 49. As the orifice blockage increasing to that of the bluff body, the attained pressure decreases. This is likely due to the bluff body's proximity to the ignition location, which is too short a distance for flame kernel to growth to the full diameter of the chamber; however, it imposes additional turbulence that is favorable in comparison to its absence.

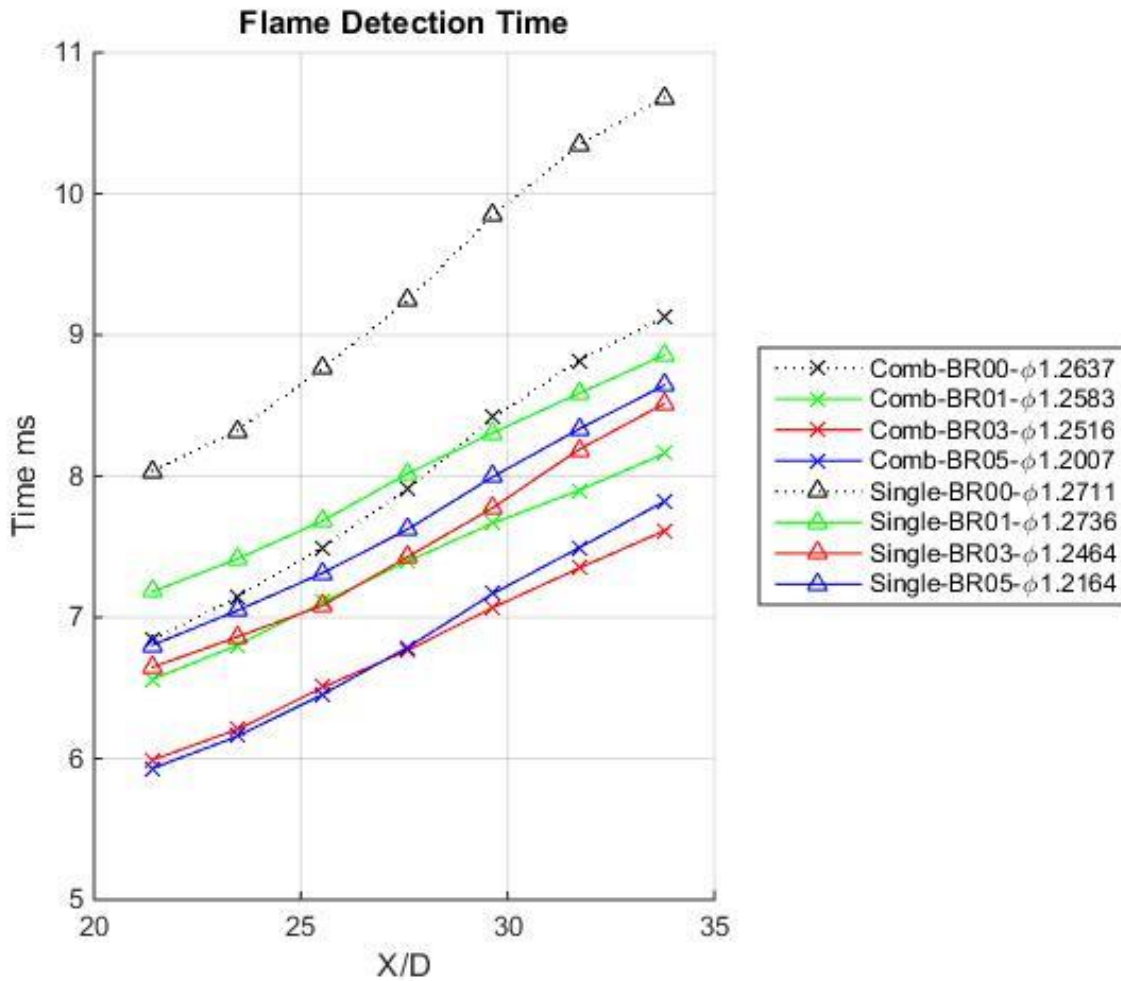


Figure 50 Flame Detection Time of Single and Combined BRs at Φ 1.2516 Mass Air 0.0543 kg/s

It was found that an improved metric for comparison was using the blowdown time; time between spark discharge and ion sensing, to establish the overall performance. If Ion velocity was utilized only, i.e., the velocity between consecutive pairs in the diagnostic section, the overall trends would be lost. It is interesting to note that the higher blockage ratio begins to collapse onto each other while the velocity trend peaks at the BR03 (44%) and significantly decreases for the BR05 (59%) orifice possibly due to excessive mixing. It is apparent that the velocity spike occurs shortly after the blockage and then decreases to a moderate level.

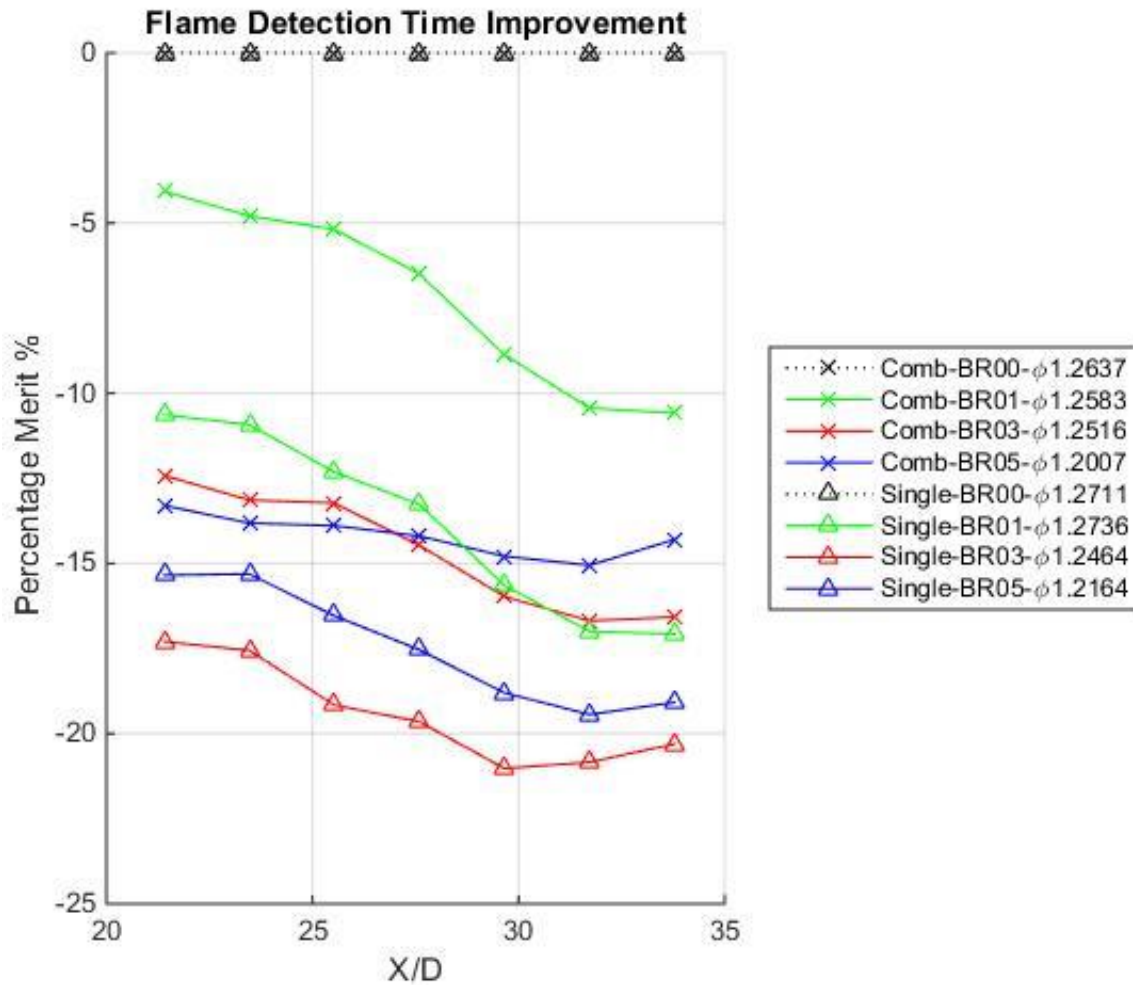


Figure 51 Improvement of Flame Detection Time of Single and Combined BRs at Φ 1.2516 Mass Air 0.0543 kg/s. Referenced to BR00

Using no blockage with spacers as the baseline, it becomes apparent that the bluff body significantly decreases the blowdown time as would be expected due to it acting as the first blockage in a series of two.

A very important consideration, neglected by many studies, is the associated flow losses due to the physical obstacles.

Table 8 Phase 2 Filling Losses for Each Configuration

Head Pressure during Steady State Filling		Pressure Loss			
Configuration	B.R. %	M _{air} 0.0539 kg/s		M _{air} 0.0763 kg/s	
		Psi	%	Psi	%
Comb_BR00	46.4 00.0	0.263	1.813	0.432	2.977
Comb_BR01	46.4 29.4	0.379	2.610	0.591	4.072
Comb_BR03	46.4 44.0	0.534	3.682	0.927	6.390
Comb_BR05	46.4 59.2	0.977	6.734	1.853	12.766
Single_BR00	0 0.0	0.183	1.263	0.273	1.880
Single_BR01	0 29.4	0.305	2.099	0.419	2.885
Single_BR03	0 44.0	0.476	3.280	0.789	5.438
Single_BR05	0 59.2	0.922	6.350	1.752	12.074

Performance of the streamlined bluff body in comparison to a single orifice is noteworthy. This should highlight the need to intelligently design physical geometry for its intended purpose in order to reduce flow losses and improve survivability. In the case of the bluff body and BR03 a 52% reduction in pressure loss was achieved with roughly the same blockage ratio as BR03.

4.3 Phase 3: JICF Testing

4.3.1 Representative Raw Data

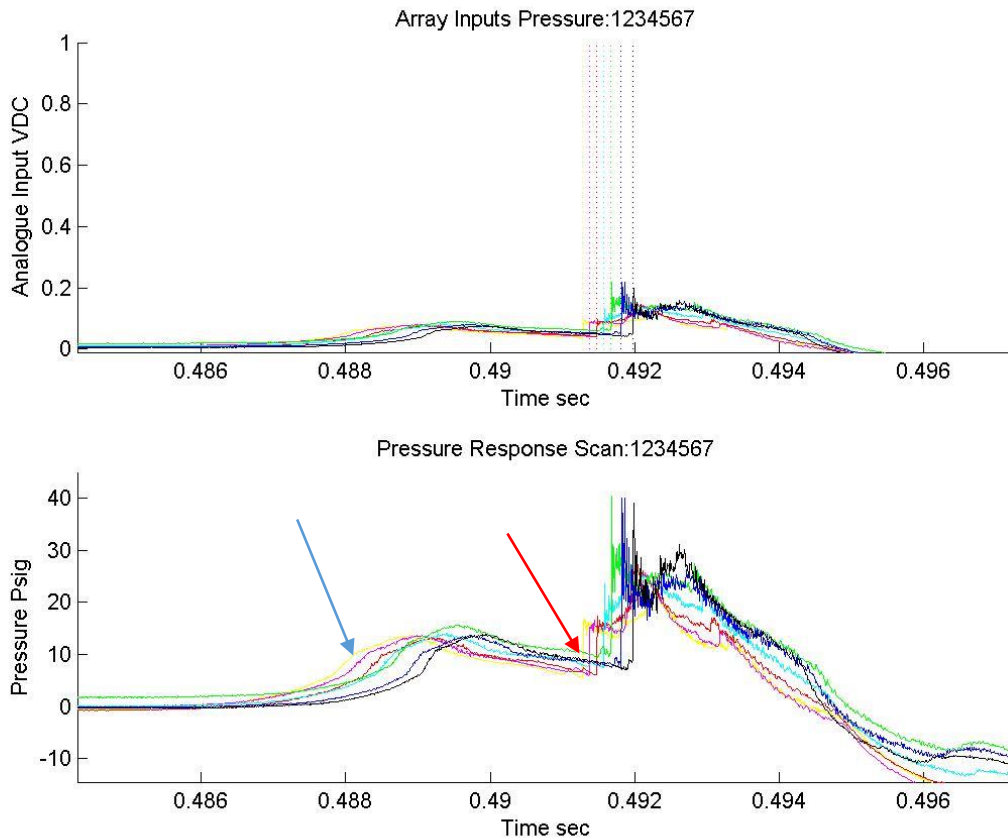


Figure 52 JICF03 (α 25° β 135°) M_{air} 0.054kg/s Φ 1.2808|0.9877 Pressure Sweep

The above figure is the pressure scan of all dynamic pressure transducers simultaneously. Two important observations; first, a weakly formed acoustic wave (blue arrow), and secondly a reflected shock (red arrow) followed by an increase in post shock pressure.

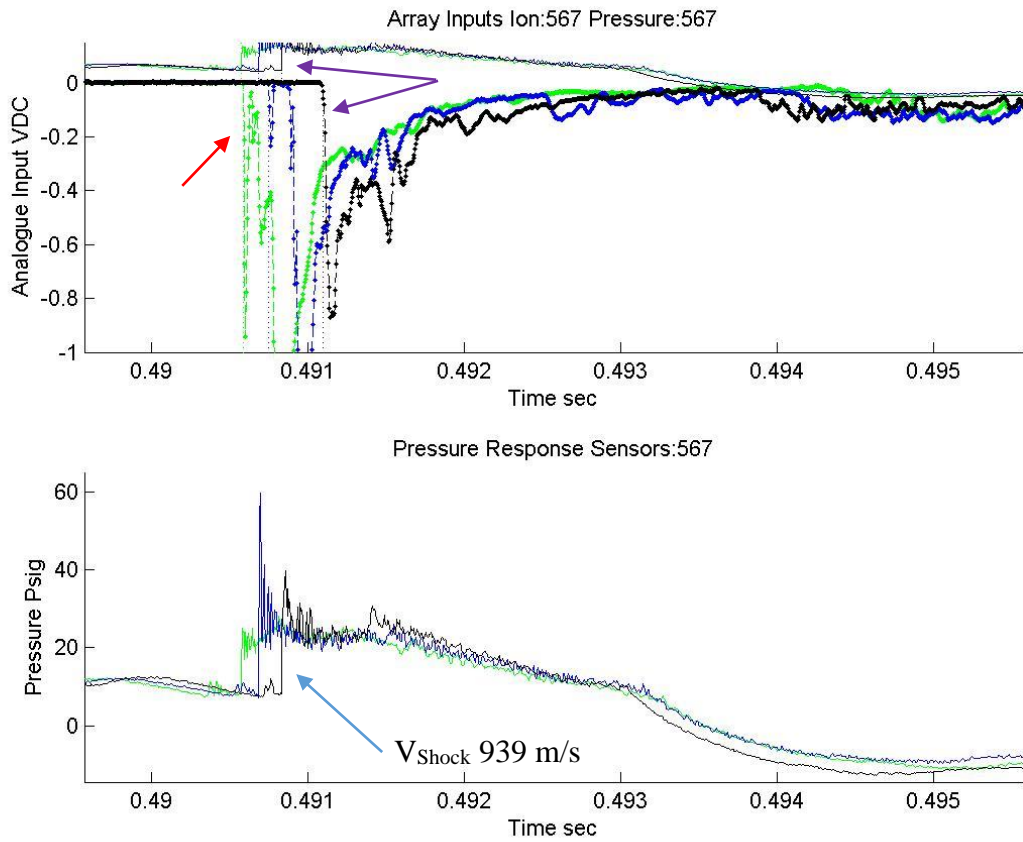


Figure 53 JICF03 (α 25° β 135°) M_{air} 0.0539kg/s Φ 1.2808|0.9886 Paired 567

Looking closely at the paired pressure and ion sensors it becomes apparent that a reflection entered the diagnostic array after the flame front and continued through it. Station 5 (green lines) shows that the two fronts approximately coincide and by station 7 (black lines) the pressure wave has overtaken the flame front.

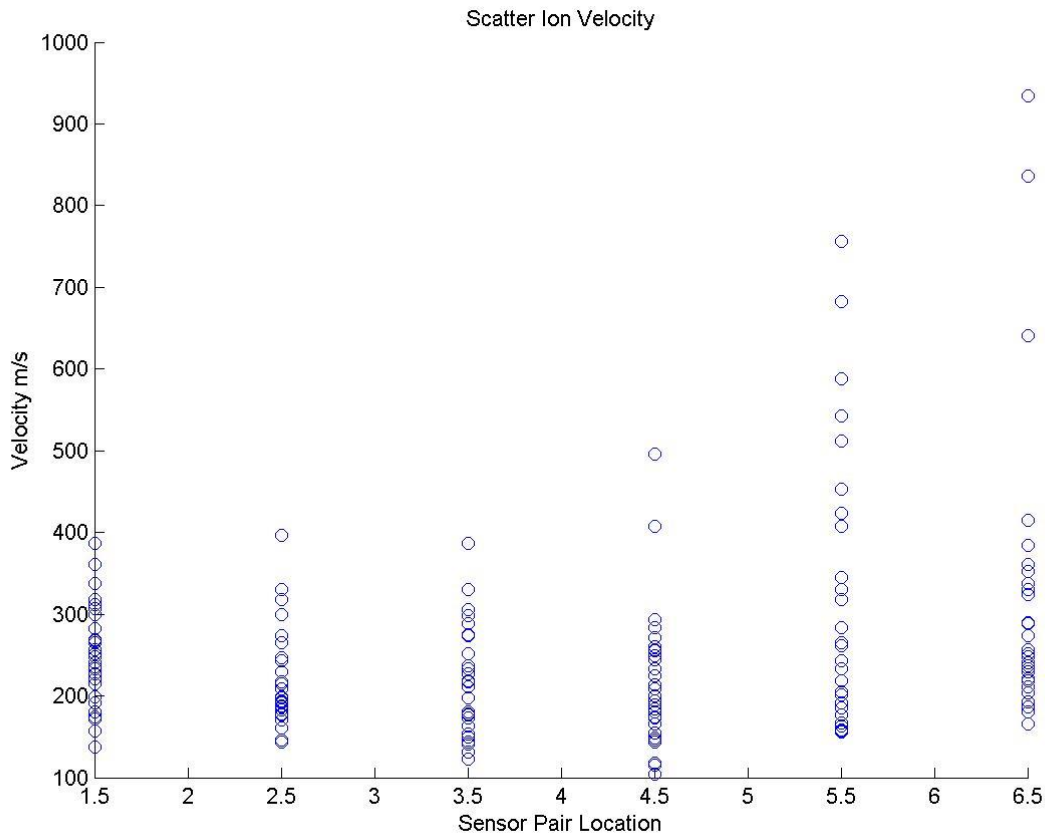


Figure 54 JICF03 (α 25° β 135°) M_{air} 0.0539kg/s Φ 1.2808/0.9886

Scatter in the study displayed a generous spread as can be observed in the above plot. To condense the data to a few figures of merit that represents the majority of the cases, only points between the 10th and 90th percentiles as well as within the outlying 30% of the raw standard deviation were used. This strips the representative value from the extreme outliers while maintaining a reasonable level of agreement. The two condensed metrics retained is the mean and standard deviation.

4.3.2 JICF Sweep Condensed Data

In order to establish global trends for various JICF orientations and locations a sweep was conducted under the same operating conditions. Equivalence ratios examined were 0.98, and 1.28, and air mass flow rates of 0.0539, and 0.0764 kg/s to determine consistency.

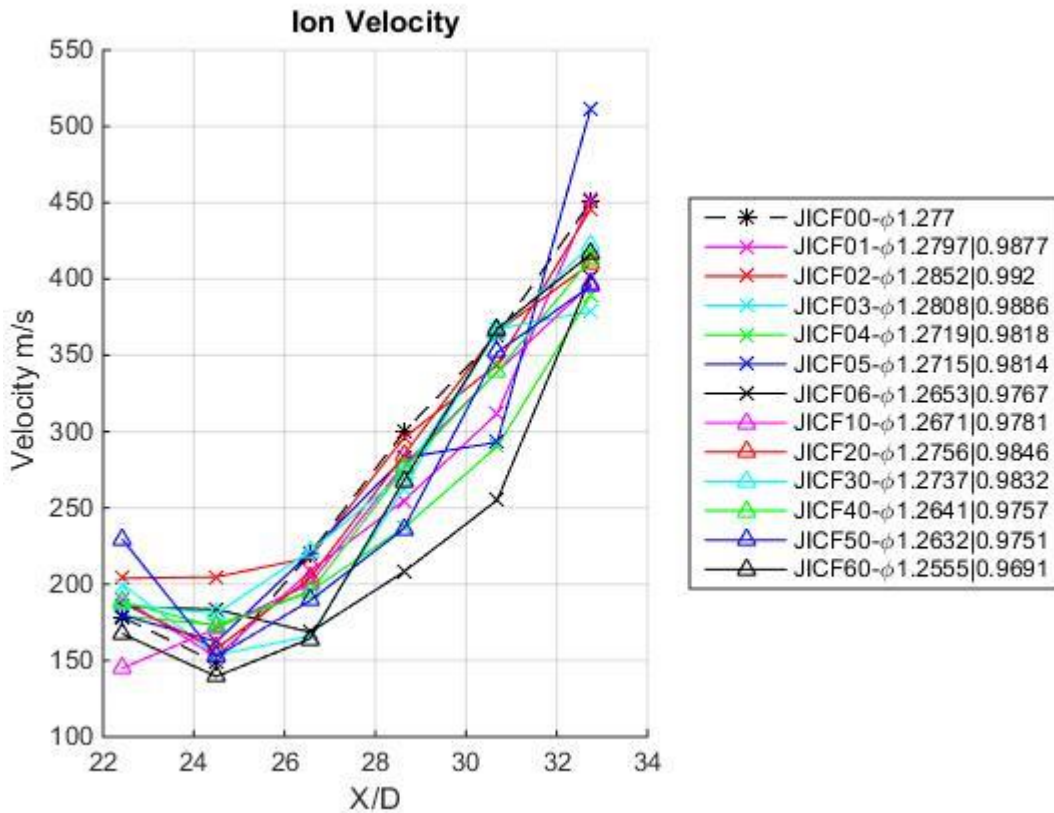


Figure 55 Ion Velocity JICF Sweep, Φ 1.28, MR 3.855

The first insight in the above figure is a slightly detrimental to negligible effect of the JICF's on flame velocity. The standard deviation for many of the cases range between 50-100 m/s and is the same magnitude as the difference from the baseline. It must be stated that due to the high deviations, no strong conclusions can be drawn other than an ineffectiveness to accelerate the flame and more than likely a detriment to the chemical reaction rate. The detriment stems from multiple items; first the leaning of the fuel air mixture decreasing the chemical reaction rate by the introduction of diluting air, secondly poor mixing will impose locations with no chemical reactions

due to lack of fuel content, thirdly the additional of cool JICF air serves to cool the reactants, flame brush, and products. The addition alone increases the bulk flow rate by up to 28% during filling for MR 3.855 as displayed. The fact that the fluidic cases display velocities at or under the baseline case, with no JICF injection, indicates the effects of the negative attributes.

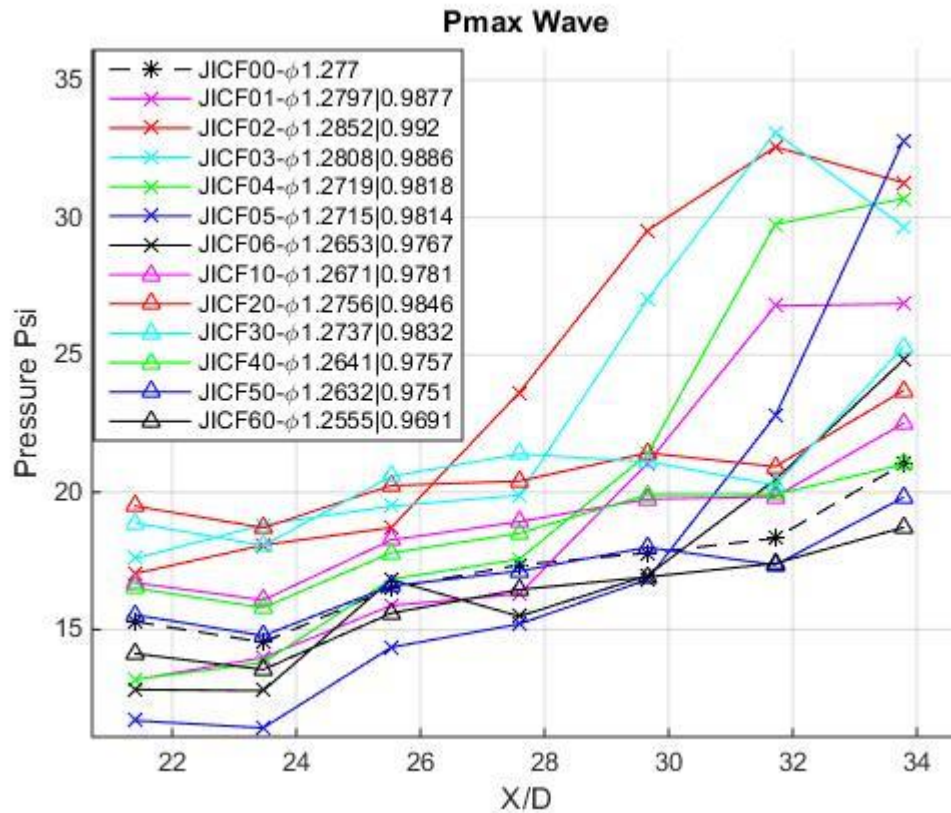


Figure 56 Max Pressure JICF Sweep, Φ 1.28, MR 3.855

Observations in figure 56 indicate 2 trends. First, jet orientation displays favorability towards Upward facing JICF's (α 25° β 90°-180°) for the majority of the sensor locations. Secondly, axial position displays a large favorability to the leading location for all JICF's, denoted by JICF0#.

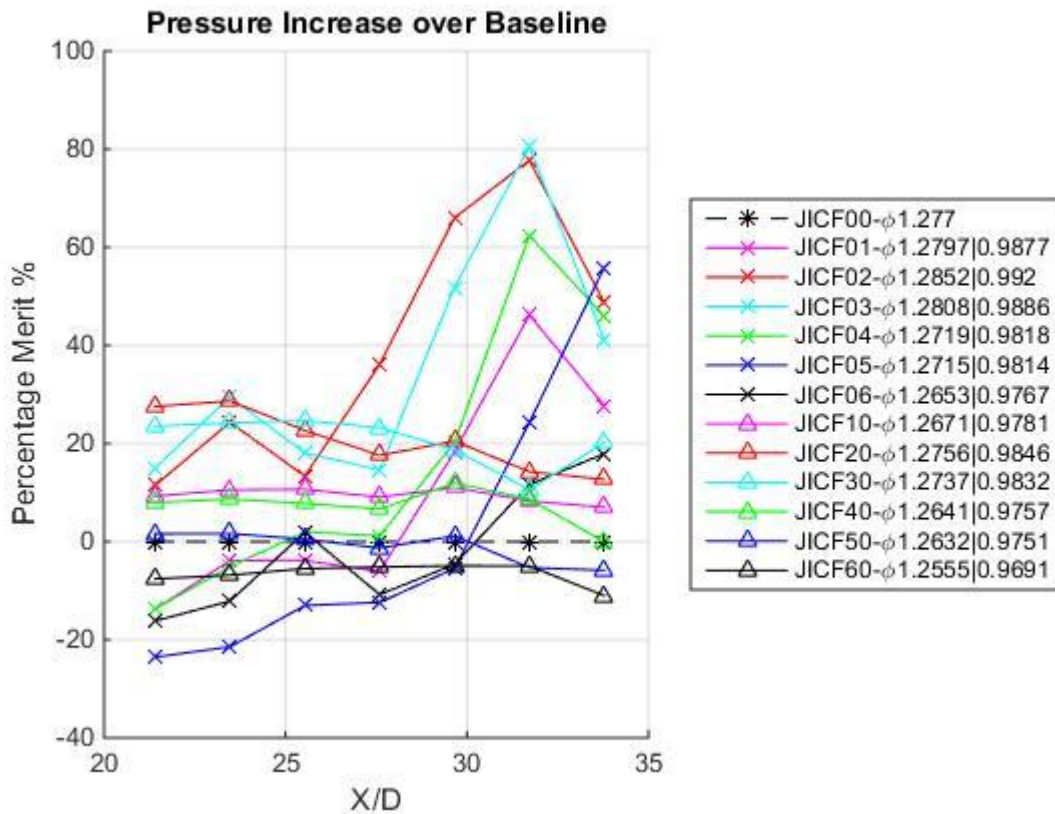


Figure 57 Pressure Increase over Baseline JICF Sweep, Φ 1.28, MR 3.855

In comparison to the baseline clean configuration, the pressure increases can clearly be observed and the best performing cases are JICF02 JICF03 α 25° and β 180° and 135° respectively. There are several other configurations with a lower the attained pressure. These detrimental flow structures are those that theoretically produce large and long lasting vortex pairs that mix poorly with the bulk flow. Take the two cases closely aligned with the flow and fall near or under the baseline case.

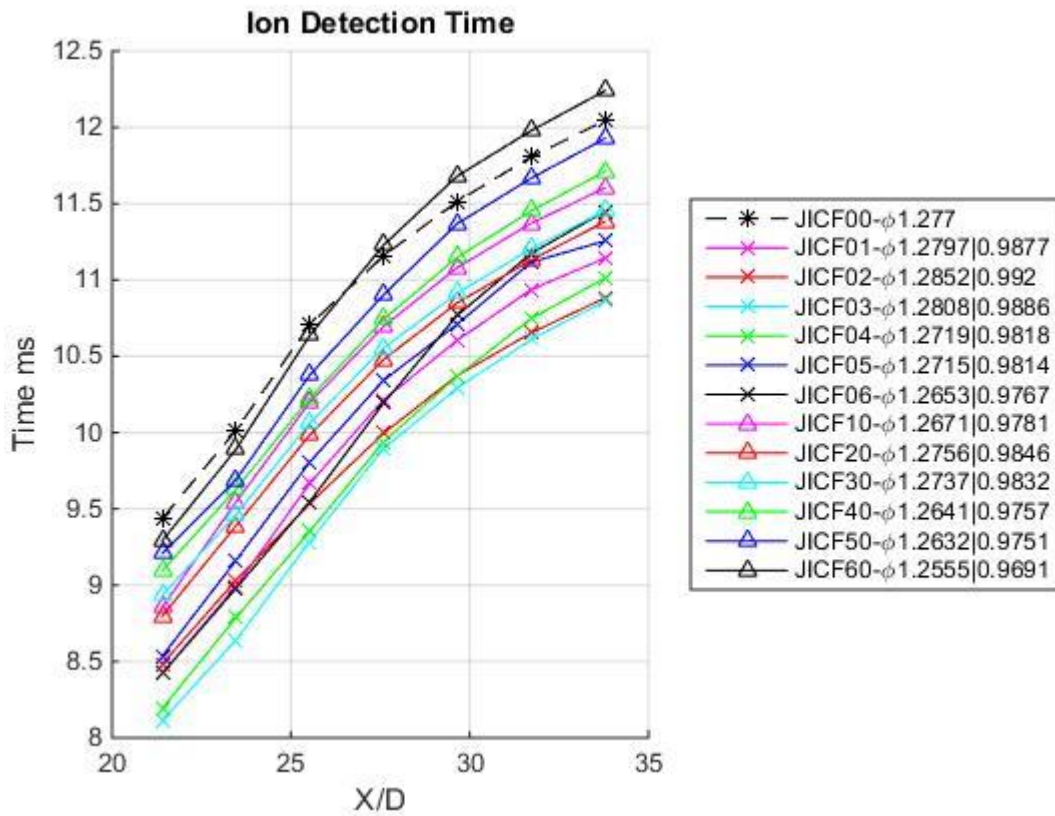


Figure 58 Ion Detection Time JICF Sweep, M_{air} 0.0539 kg/s, Φ 1.28, MR 3.855

The detection times for the JICFs are located in the above figure. A clear difference is the separation of the aft and forward locations of JICF injection. This is logical as the leading location has a significantly longer length and time for its effect to influence the combustion process. Both locations also display a strong favorability to several JICF orientations.

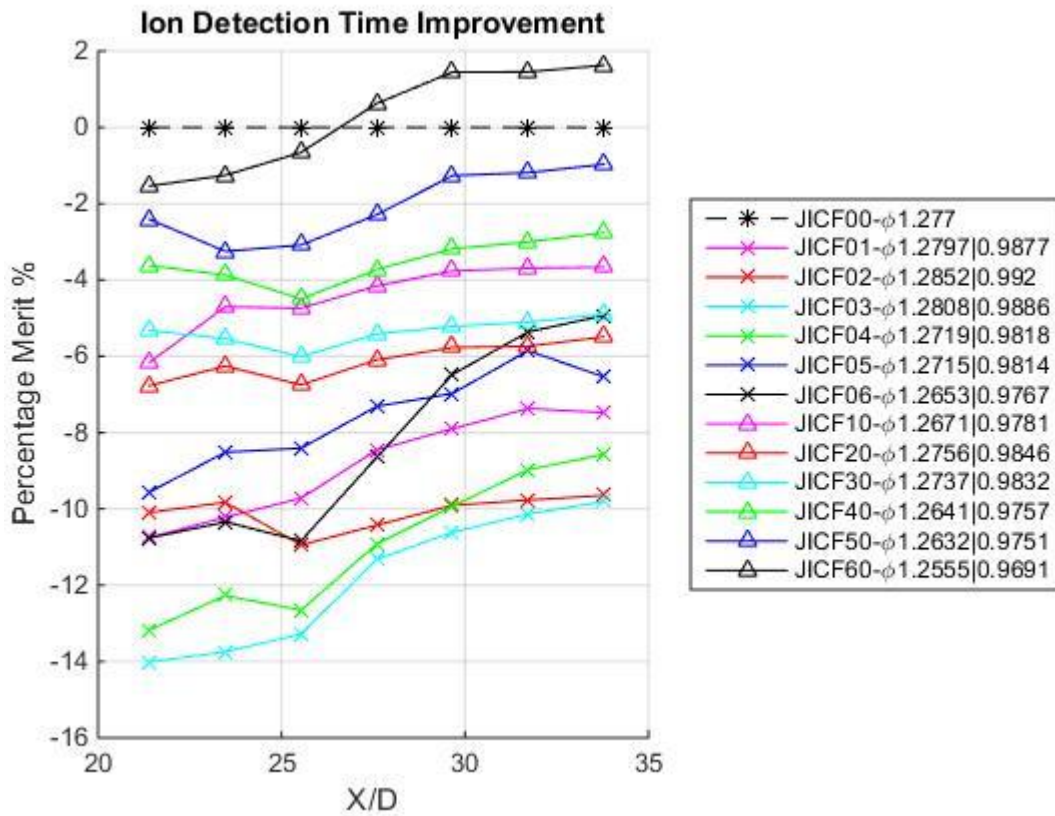


Figure 59 Ion Detection Time Improvement JICF Sweep, M_{air} 0.0539 kg/s, Φ 1.28, MR 3.855

The improvements in blowdown time in comparison to the baseline clean case is located in the above figure with negative values signifying a favorable reduction in time. The best performer was JICF03, α 25° β 135°, upward facing and 45° off, estimated to induce a biased paired streamwise vortex with small shedding filaments⁷.

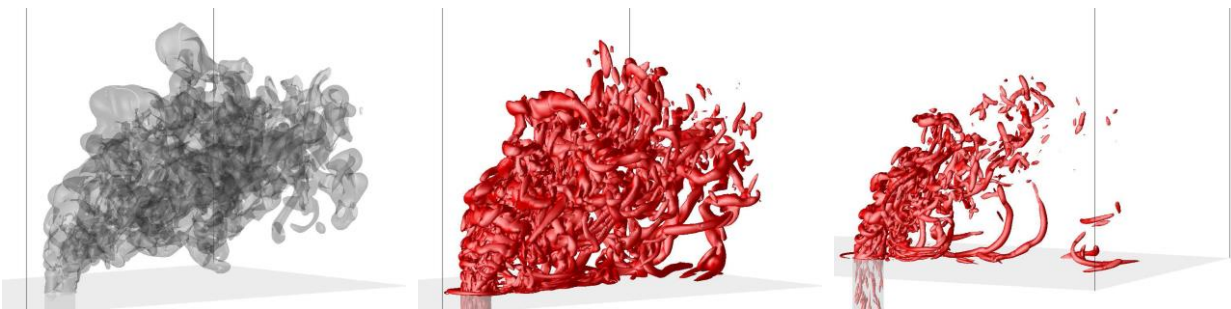


Figure 60 Visualization of Instantaneous flow field of a Normal JICF, MR 3.3, Re 2100, Bulk Flow M 0.2³¹

Figure 60 is an example of the instantaneous flow field of a vortex shedding JICF normal to the wall. The first image to the left is a transparent scalar contour of vortex intensity while the other two to the right are solid contours at two different vorticity levels³¹.

4.3.3 Effect of varying jet strength

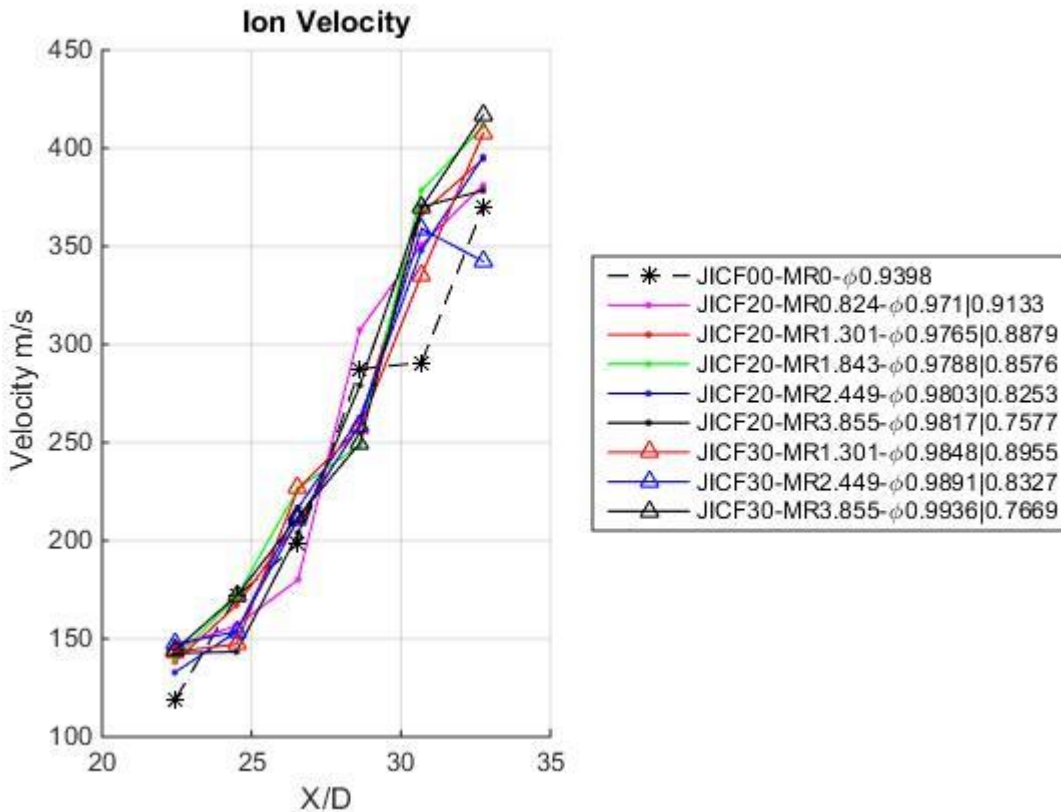


Figure 61 Ion Velocity JICF20 (α 25° β 135° and 180°) MR Sweep, initial Φ 0.98

Varying jet strength in the above plot displays a fairly minimal impact on flame velocity regardless of the addition of oxidizer. First, the leaning of the fuel air mixture has no discernable impact on flame velocity. Secondly, there is likely a non-reactive pocket of gasses that is too lean to combust before mixing takes place and furthermore the temperature change and high shear likely results in localized quenching. The main takeaway from this is that a significant dilute (up to 28.7% for MR3.855) can be added to the mixture stream in an asymmetric fashion without effecting the

deflagration velocity achieved. The caveat to this trend is that the addition of oxidizer also increases the bulk flow rate and velocity that leads to a maximum steady state filling increase of approximately 7.37 m/s for the MR 3.855 case.

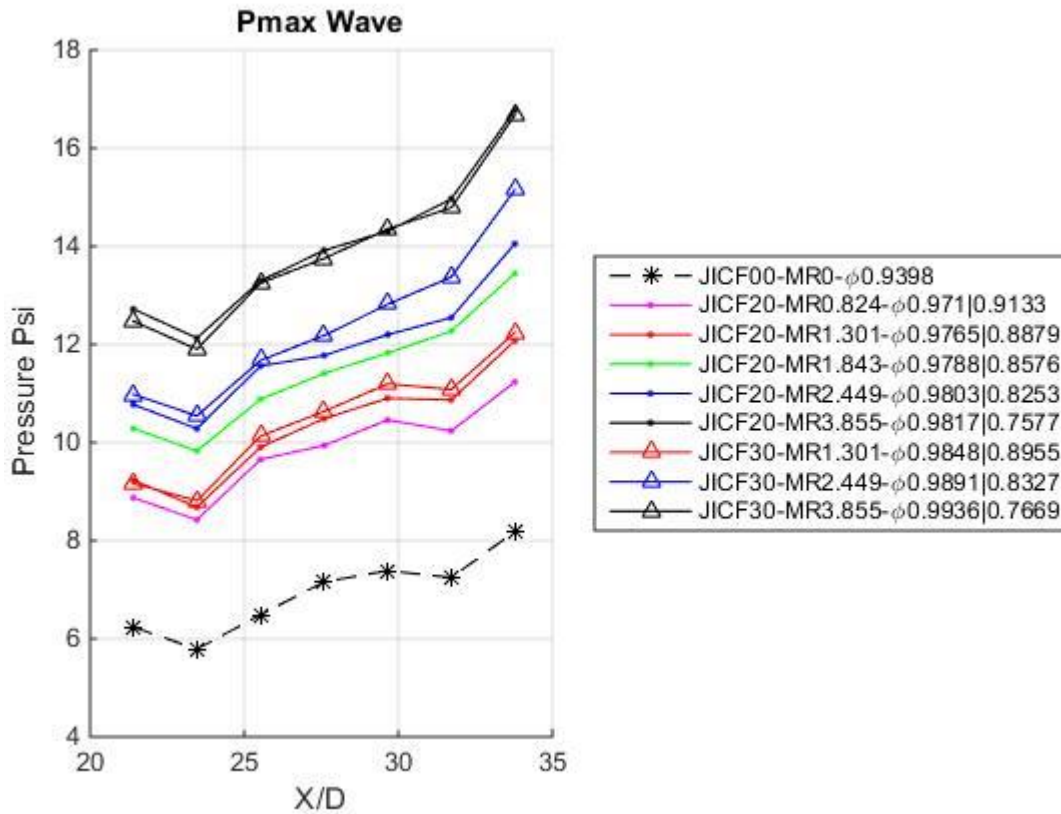


Figure 62 Max Pressure JICF20 (α 25° β 180°) MR Sweep, initial Φ 0.98

Achieved max pressure displays a strong correlation with increasing momentum Ratio even for cases with lower maximums such as the above figure. The Standard deviation of the data ranges from 1 to 5psi, the same order of magnitude as the difference above for some locations. To that extent only general trends are trusted. As for the dilution of the bulk flow, once again the pressure does not seem to degrade; however, there are several competing effects as previously discussed.

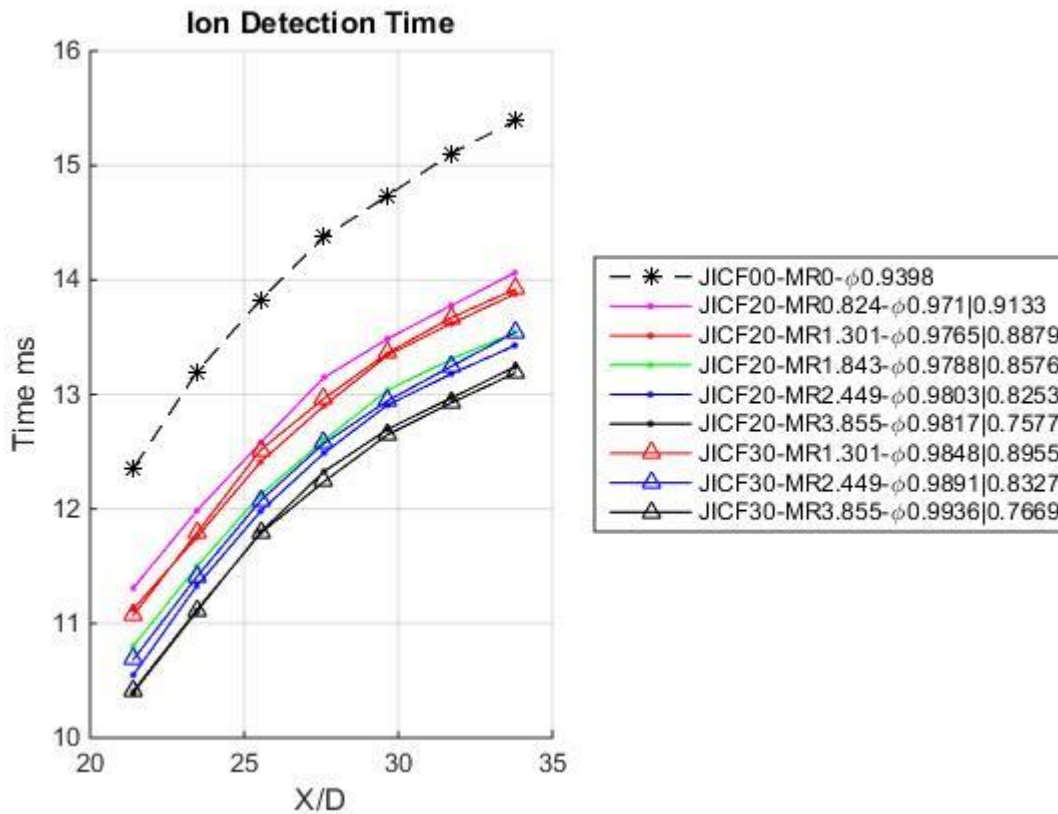


Figure 63 Ion Detection Time JICF20 and 30 (α 25° β 180° 135°) MR Sweep, initial Φ 0.98

Ion detection time displays clear correlations with increasing momentum ratio in figure 63. The aft location, as displayed, produces a fundamentally smaller difference than the leading location. It must be noted that the change in velocity due to the addition of the JICF dilute does not in fact make up the differences in blowdown time. This implication suggest that another mechanism is the root cause of the trend and from previous studies for both fluidic and physical obstacles can display a localized velocity spike without an increase downstream.

4.3.4 Equivalence Ratio Influence

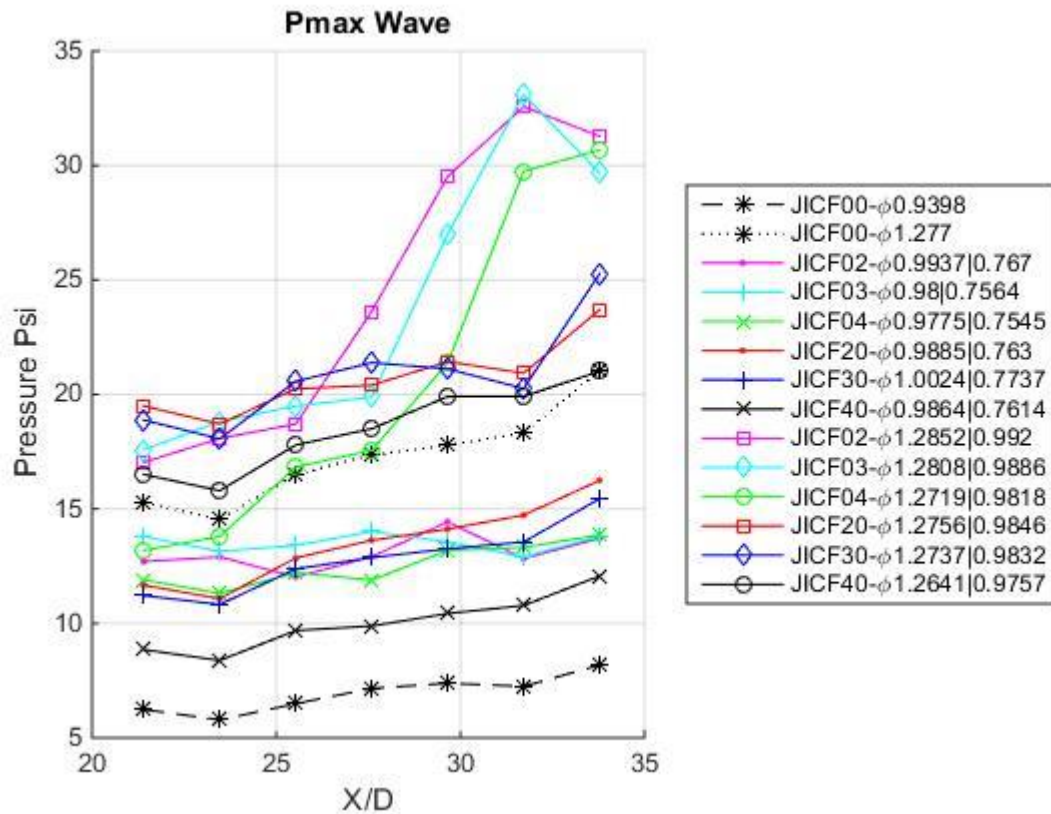


Figure 64 JICF 02, 03, 04, 20, 30, 40 $M_{air} 0.0539\text{kg/s}$ MR3.855 Φ 1.00 and 1.28

The base fuel air mixture has a profound impact on the attained pressure. Rich mixtures yield a slightly lower final temperature; however, the chemical reaction rate and heat release is higher than its lean counterpart. Also of interest is the 3 cases that display a sharp increase in pressure represent the rich mixtures while the lean displays a fairly consistent increase throughout the diagnostic section.

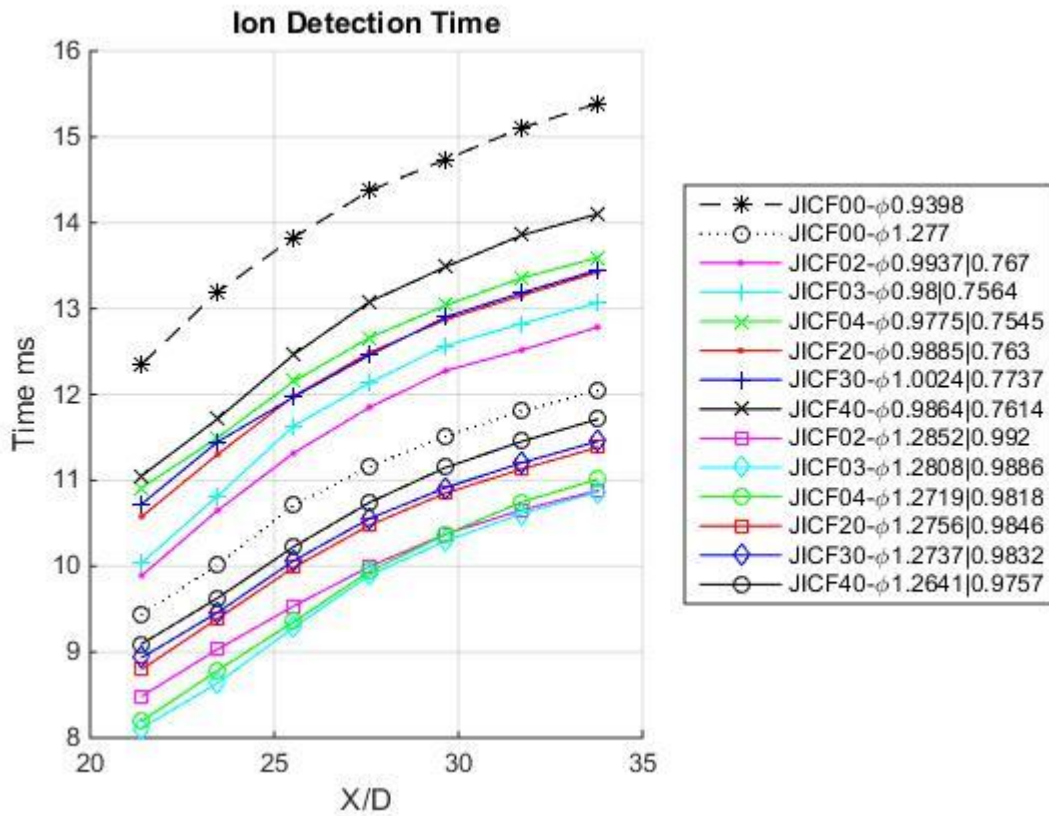


Figure 65 JICF 02, 03, 04, 20, 30, 40 M_{air} 0.0539kg/s MR3.855 Φ 1.00 and 1.28

Given the same addition of dilute for every JICF case, the impact of orientation and location can be easily observed in figure 65. The three best performing orientations at both locations are displayed, α 25° β 90° 135° and 180° for both axial locations and equivalence ratios. The largest impact of time reduction stems from equivalence ratio, followed by the axial injection location favoring rich mixtures and upstream JICF injection.

4.3.5 Bulk Flow Effects

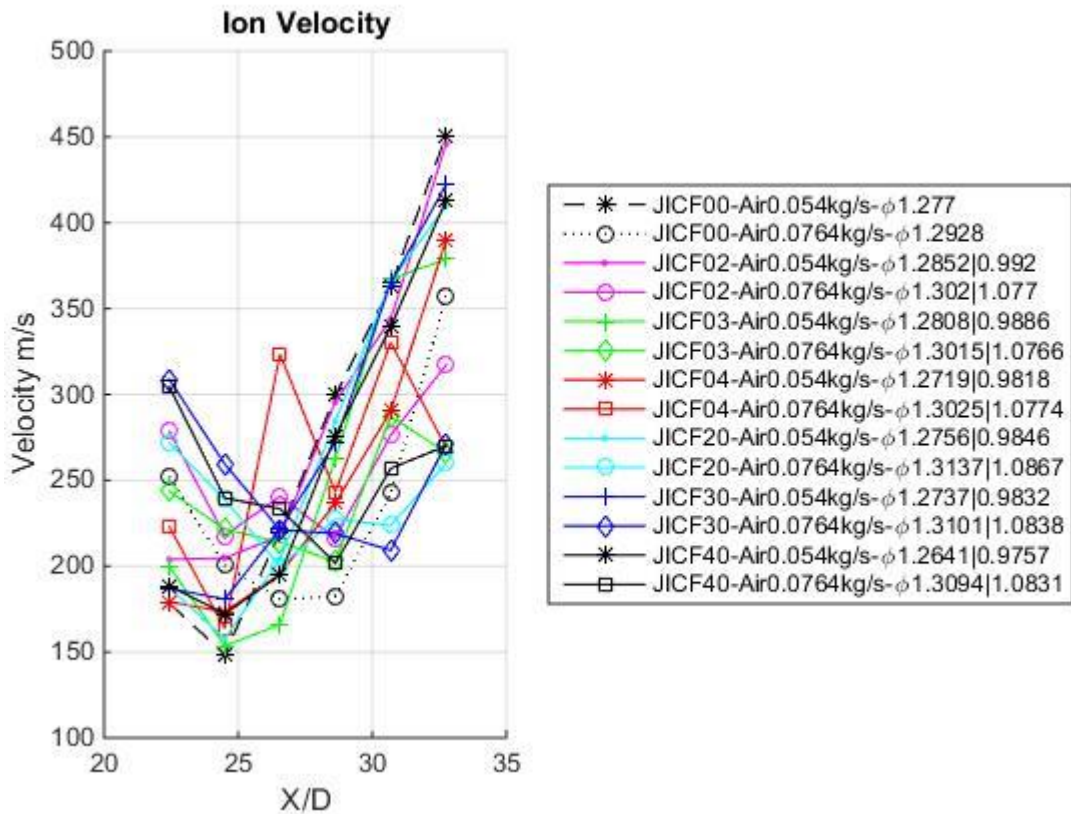


Figure 66 Effect of Flow Rate on JICF Flame Velocity

A few correlations can be drawn in the above figure including a decrease in flame velocity with an increase in fill velocity. One could assume that it is due to a lower JICF MR; however, the clean configurations displayed the same trend. The flame velocity (150-450 m/s) is much larger than the filling of reactants (25.4-36.5 m/s). The difference between the two clean configurations is less than 120 m/s, just outside of the standard deviations and surprisingly contains many of the JICF data points within the two. In general, the higher bulk flow rate displays lower flame velocities, especially those interacting with the JICF's.

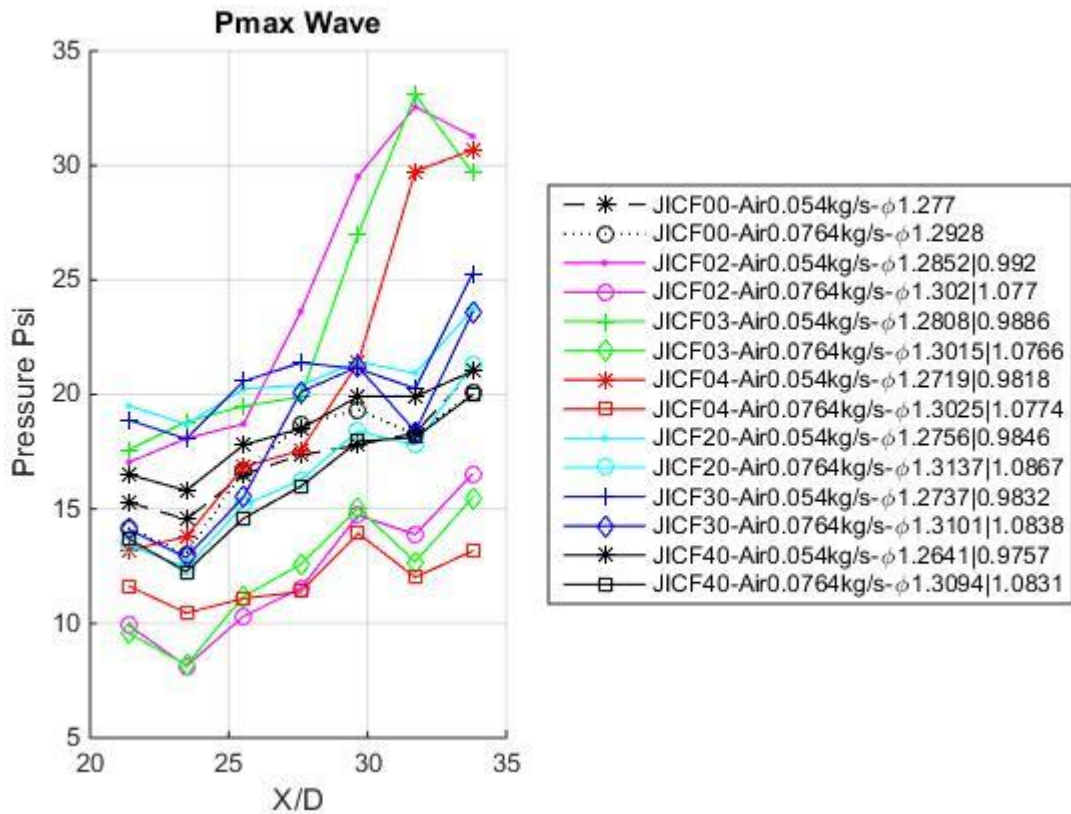


Figure 67 Effect of Flow rate on JICF Max Pressure

The achieved pressure displays a clear favorability to lower filling velocity; however, the MR of the JICF is not the same. Unlike the previous discussion of the effect of varying jet strength, the trend at the higher flow rate shows that the majority of the JICF's negatively impact the ability to build pressure. Due to the likelihood of poor mixing, and non-reacting regions, the mixing in the flow may in fact be insufficient to disperse and spread the flame front to make up for the secondary oxidizer injection.

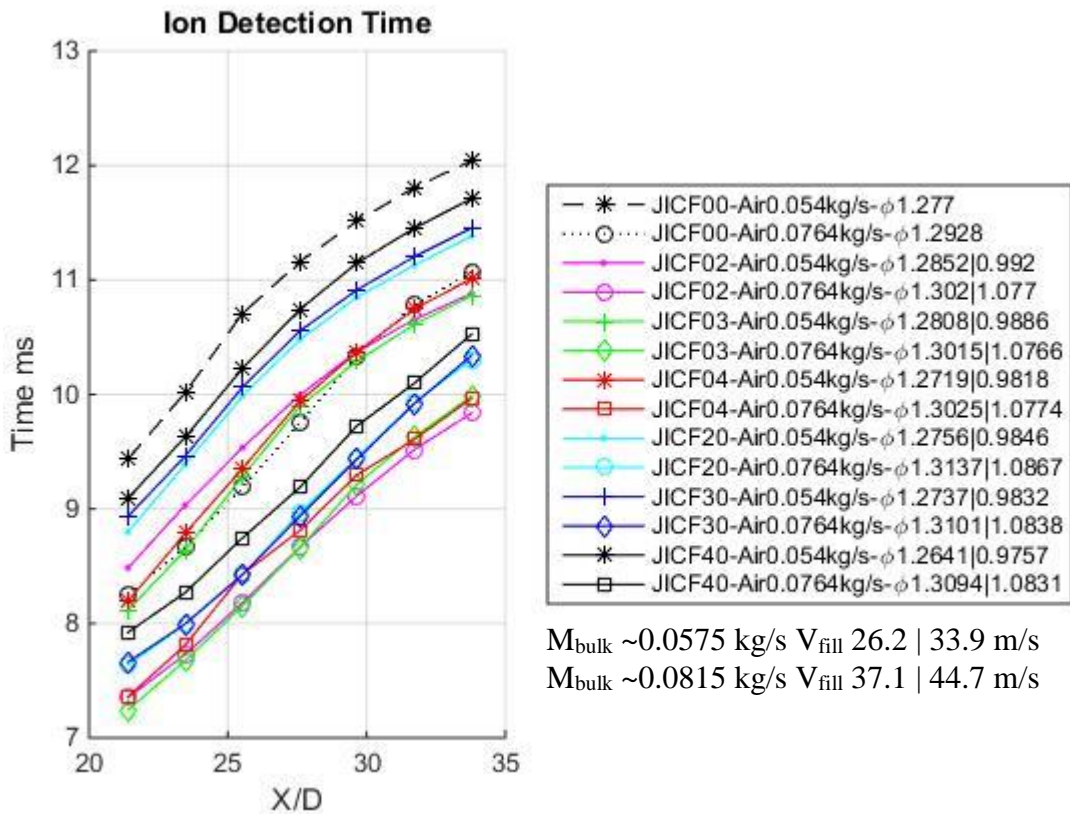


Figure 68 Bulk flow Variation on Blowdown Time

The base time difference with no JICF injection is 1.184 ms for station #1, 21.4 x/D ($M_{\text{air}} 0.0539\text{kg/s}$ 9.437ms MR 3.855 | $M_{\text{air}} 0.0764 \text{ kg/s}$ 8.253ms MR 1.911). Filling velocity does reduce the blowdown time, figure 68; however, not as significant as the reduction during filling. It is of interest that the velocity and pressure of the higher flow rate case displayed many negative impacts; however, the ion detection time still displays a reduction. The JICF delivers a secondary oxidizer mass flow rate of 0.0165 kg/s, and makes up for a difference of 0.024 kg/s between the two baseline cases to roughly match the ion detection time. At least for the higher performing cases, the flame is accelerated.

4.4 Phase 4: Bluff Body and JICF

4.4.1 Representative Raw Data

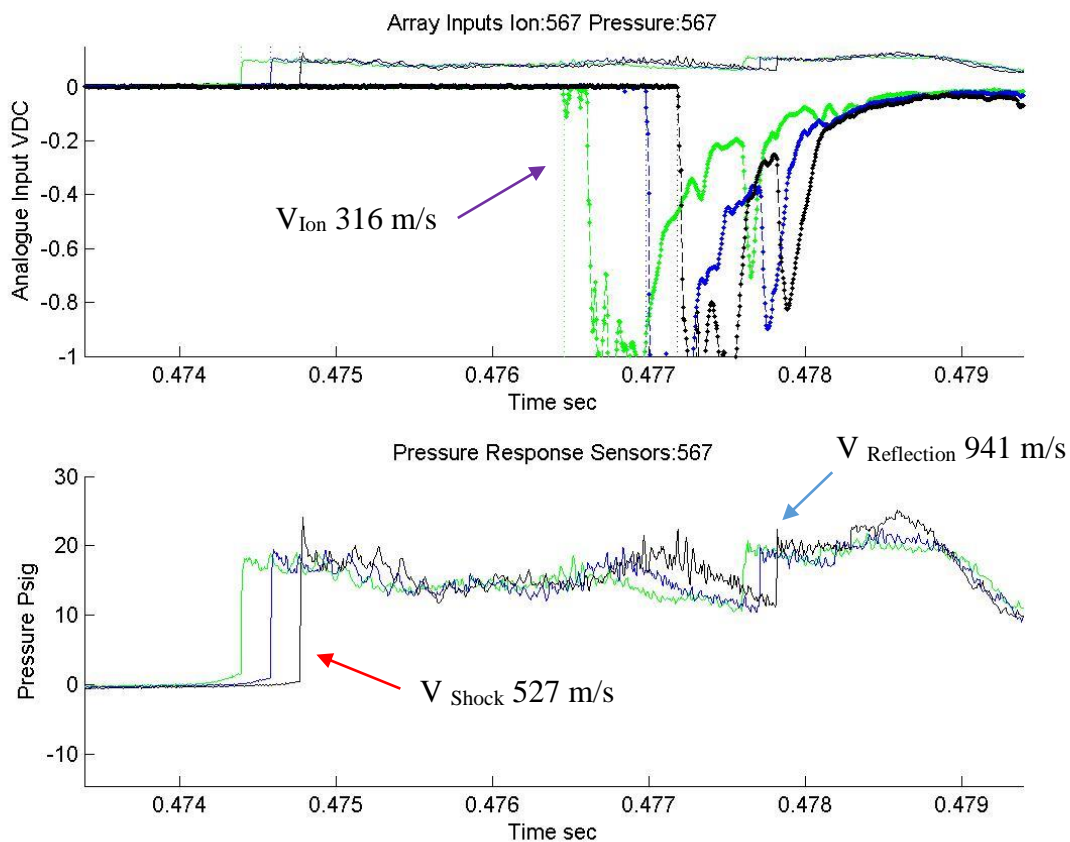


Figure 69 Hybrid Trial JICF03 ($\alpha 25^\circ \beta 135^\circ$) $M_{air} 0.0539 \text{ kg/s}$ MR3.85 $\Phi 1.307|1.008$ Station 567 paired

Looking at the above plots, three distinct trends can be observed about the velocity and pressure history. First, attained pressure is less than what would be expected from the normal shock relations with the first velocity of 527 m/s, Mach 1.524, and should yield 22.6 psi gauge pressure. The post shock pressure varies between 16 and 20 psi roughly, lower than predicted. The reason behind this pressure reduction is the perforated pressure surface upstream, displaying a blockage of 50.44% (with respect to 1.939" inner diameter) that allows a small amount of backflow from

the control volume. This corresponds well with findings from Cooper, Jewel and Shepherd that indicates a post shock pressure increase with increased blockage at the PDE's pressure surface²⁶.

4.4.2 Hybrid JICF Sweep

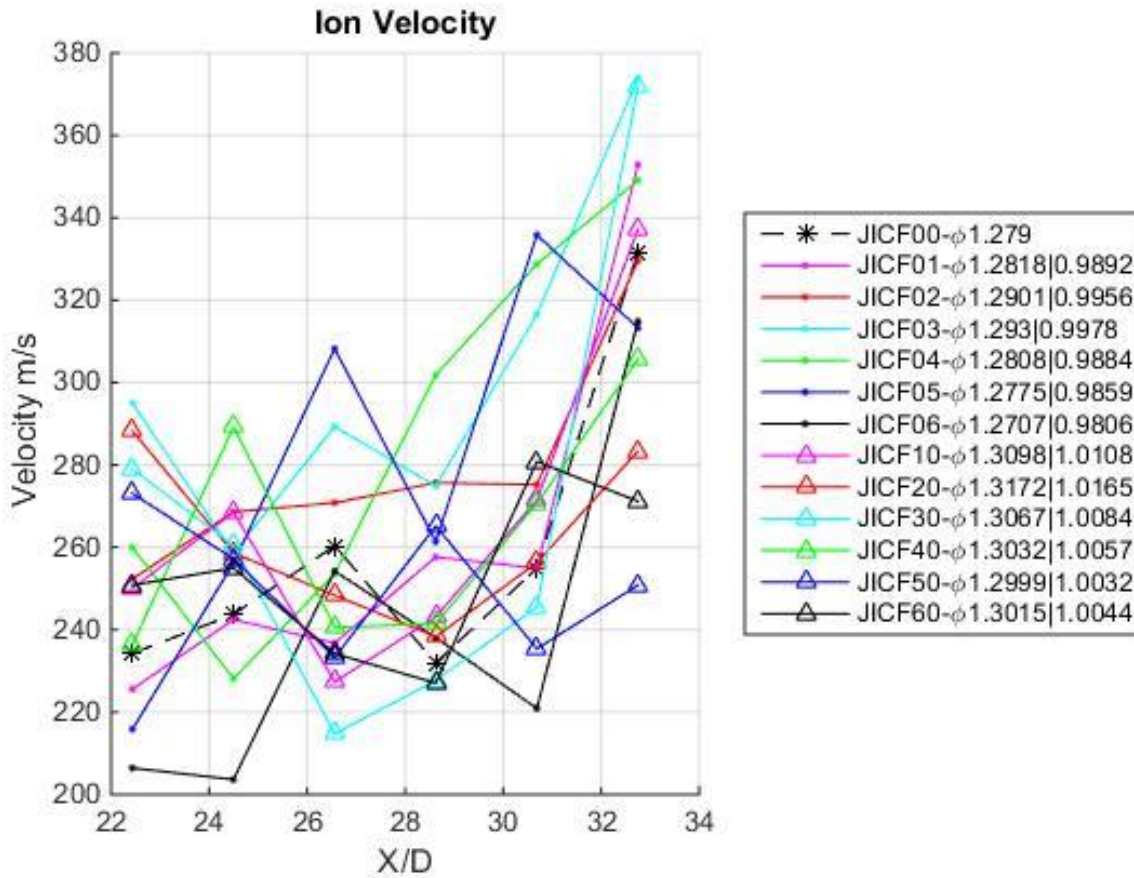


Figure 70 Hybrid Trial $M_{air} 0.0539\text{kg/s}$ MR3.85 Φ 1.28 Flame Velocity

As observed in phase #3, the trends above figure indicate a discernable effect on accelerating the flame front velocity. It must also be noted that orientation plays a role; however, the standard deviation of the data scatter hinders the ability to draw trends.

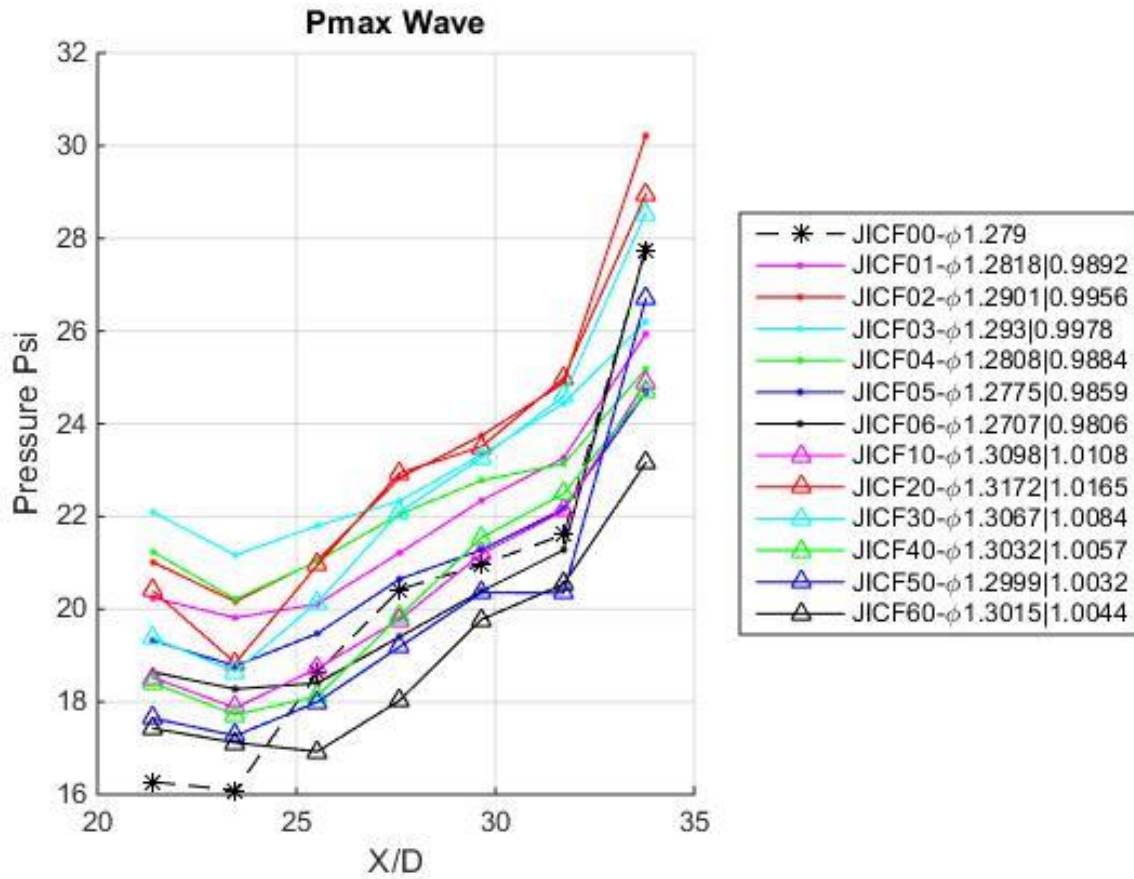


Figure 71 Hybrid Max Pressure $M_{air} 0.0539\text{kg/s}$ MR3.85 $\Phi 1.28$

The pressure trends indicate favorability to jet orientations of angle $\alpha 25^\circ$ and yaw $\beta 135^\circ$ and 180° . A slight trend, noticeable in the early stations, is a higher pressure increase for the front location of injection.

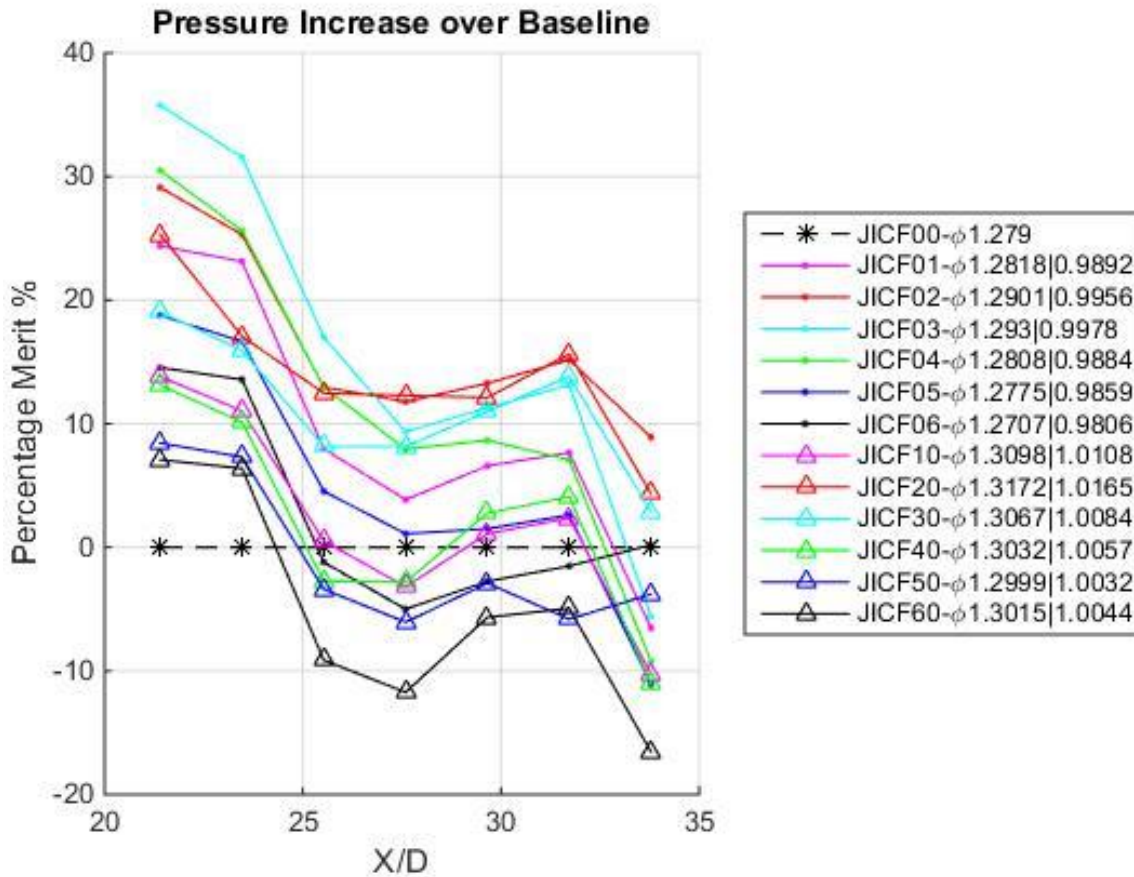


Figure 72 Hybrid Trial M_{air} 0.0539kg/s Φ 1.28 Pressure Improvement over baseline

Inspection of the increased pressure rise over the baseline helps to highlight the observed favorability. It is also interesting to note that the benefit falls off considerably as the front traverses down the tube even for the favorable orientations. Once again, the standard deviation is sufficiently large possibly skewing the results.

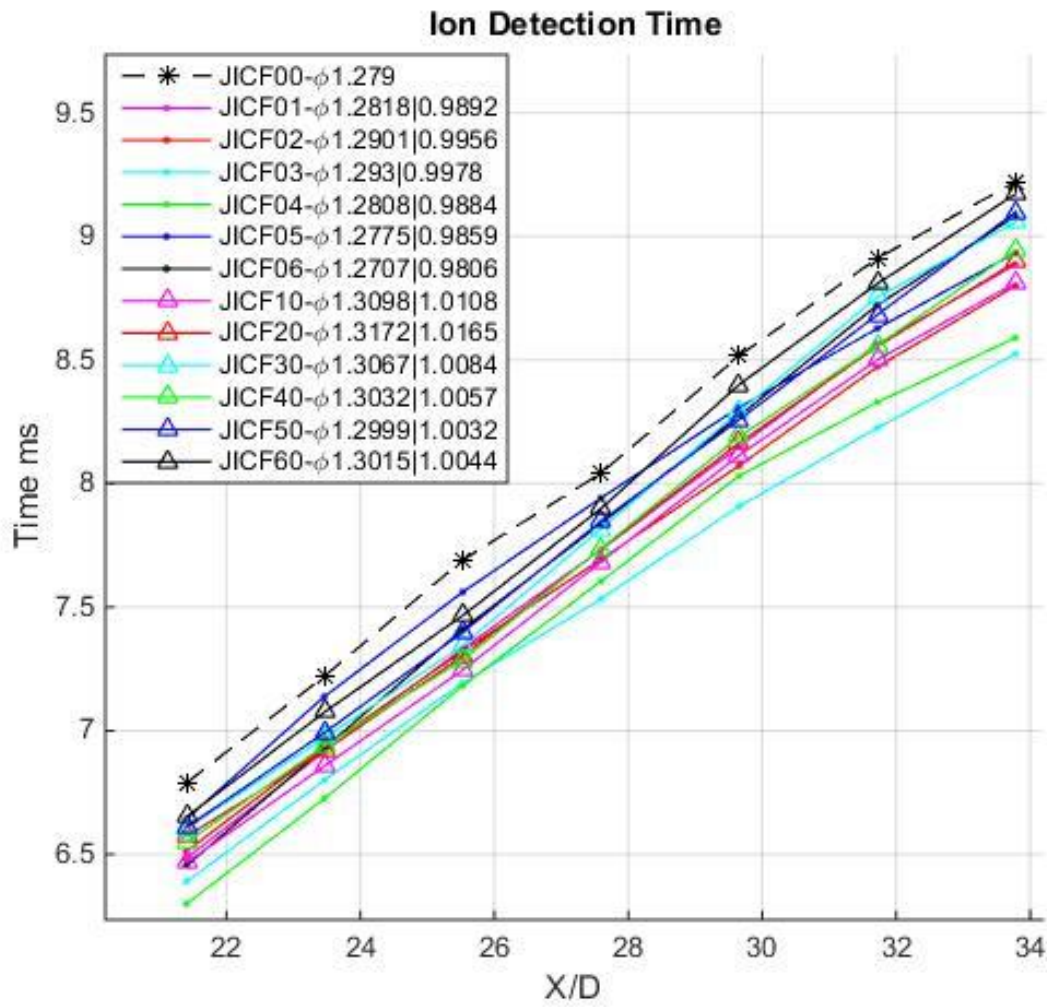


Figure 73 Hybrid Trial $M_{air} 0.0539\text{kg/s}$ $\Phi 1.28$ Ion Blowdown Time

The blowdown time in figure 73 indicates very clear favorability towards angled $\alpha 25^\circ$ and yawed $\beta 90^\circ$ to 180° jets in the forward injection location.

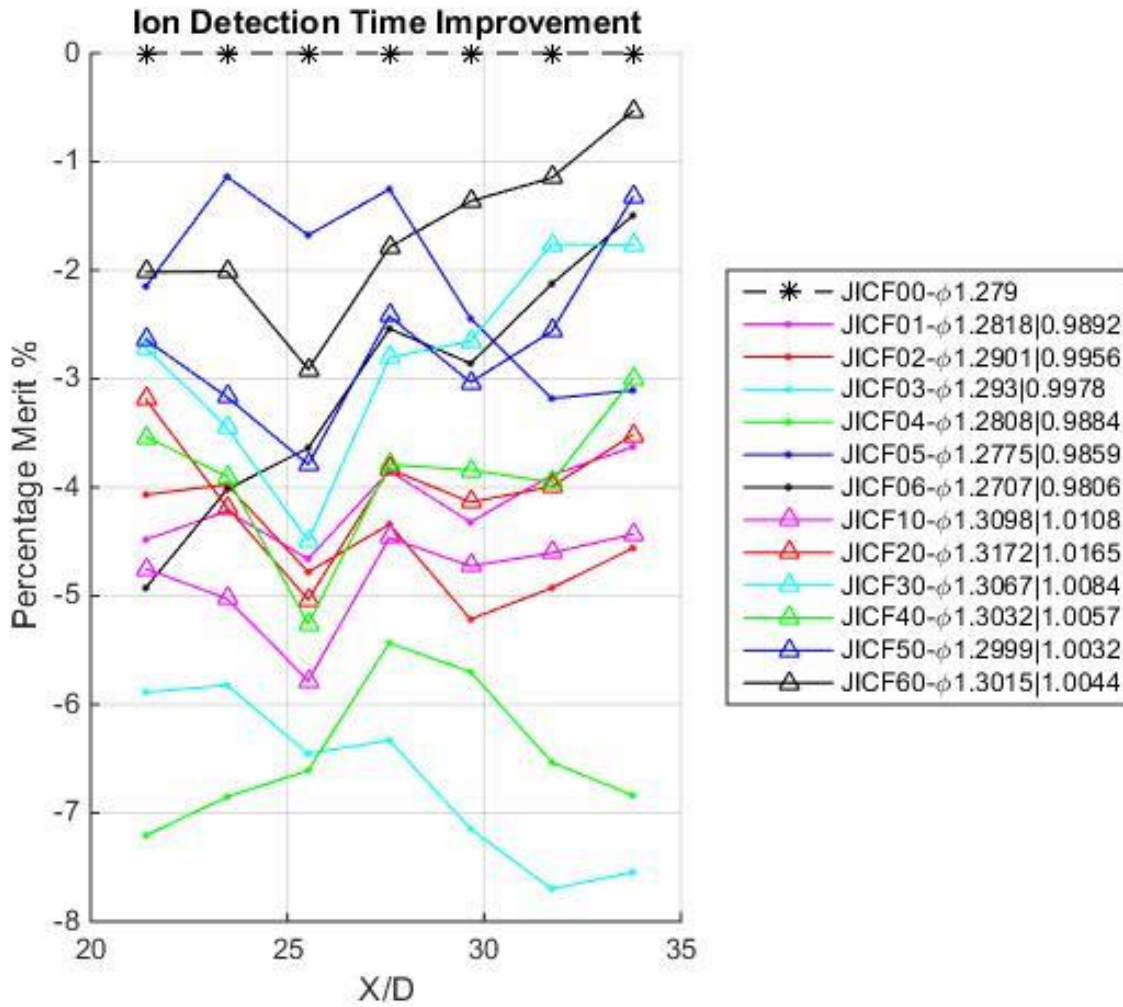


Figure 74 Hybrid Trial $M_{air} 0.0539\text{kg/s}$ 1.28 Ion Blowdown Improvement

The two most favorable cases JICF 03 and JICF 04, $\alpha 25^\circ \beta 90^\circ$ and 135° respectively, display the largest reductions in figure 74. The addition of the bluff body did not affect the favorability by much, and adjusted a slight bias from 90° to 135° ; however, just outside of the deviations.

4.5 Comparisons of Selected Physical and Fluidic Cases

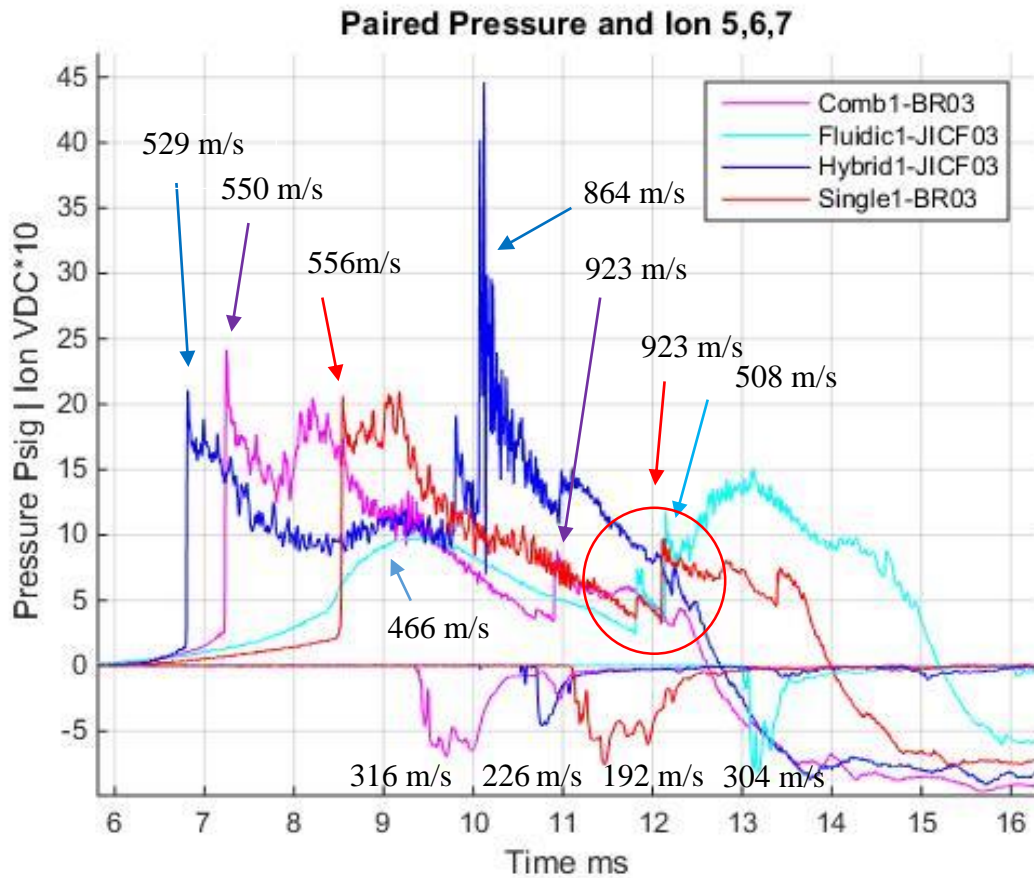


Figure 75 Pressure and Ion Data from 4 comparable configurations in station 7, velocities from stations 5, 6 and 7

The above figure displays the pressure and ion time history for station #7 with near stoichiometric fuel and air mixtures and time referenced to spark ignition. The Fluidic and Hybrid MR is 3.86 with a bulk air flow rate of 0.0539 kg/s for all cases. Several differences can easily be observed between the 4 configurations.

The JICF and single orifice are roughly comparable and interesting to note that the reflection displays the same profile; however, the differences in velocity is significant (Red Circle). The first pressure rise of the fluidic case is the beginning of the acoustic waves coalescing into a shock traveling at M 1.27-1.4 in stations 5 through 7. The time for the flame front to reach station 7 is nearly 2.19 ms longer for the fluidic case as compared with the single orifice. With this stated,

a significant section of the single orifice case is 22.5% smaller in cross-sectional area until the diagnostic section accounting for some of the time reduction.

Comparing the hybrid case and to the combine blockage the ion sensing of the hybrid lags behind by 1.126 ms; this is more a function of the area reduction for 50% of the DDT transition section as stated before. The initial peak pressure of the hybrid case is less than for its physical counterpart; however, the pressure rise of the secondary is significantly higher and yet precedes chemical reaction region which is not favorable. In general, both cases utilizing the bluff body display higher pressure and a reduction in time between the first detection of the pressure waves and ion sensing.

4.6 JICF Orientation Summary

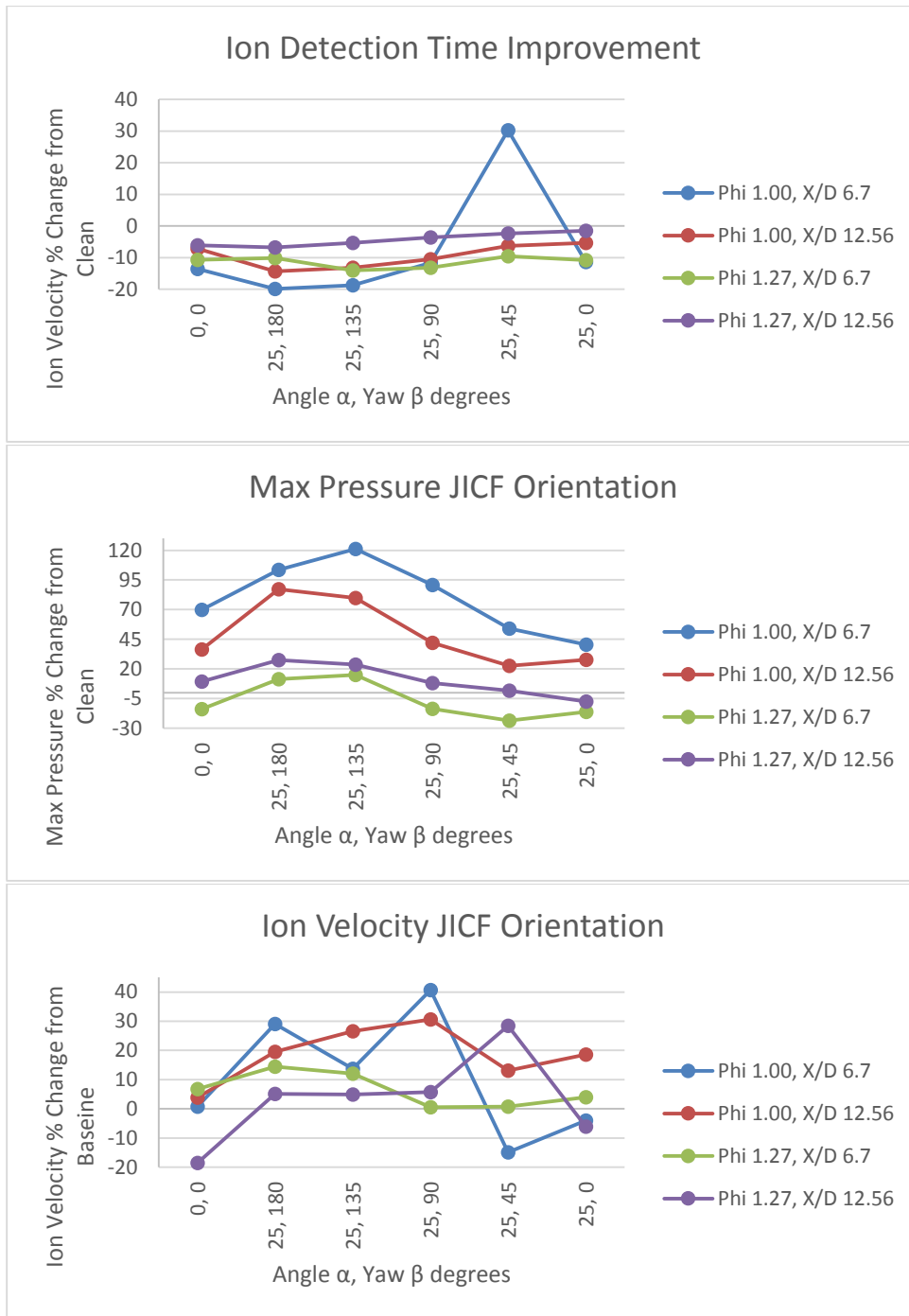


Figure 76 JICF Summarized Plots of Improvements by X/D 21.4, M_{air} 0.0539 kg/

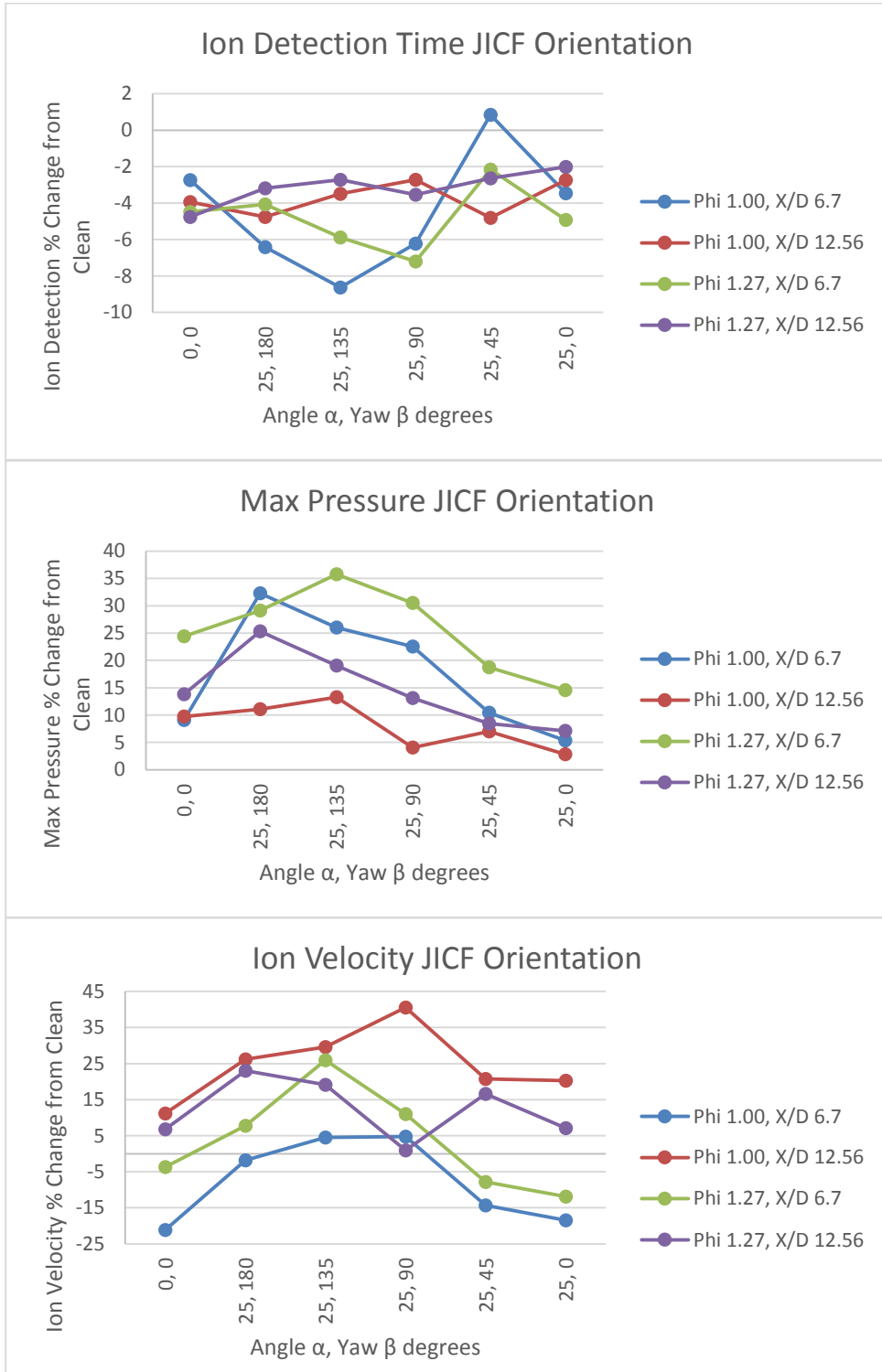


Figure 77 Hybrid Summarized Plots of Improvements by X/D 21.4, M_{air} 0.0539 kg/s

The importance of focusing on the first sensor station, station 1 X/D 21.4, is to observe the data without possible interference from the Ion Probes protrusion into the tube. From this information, the addition of a bluff body, as in the hybrid case does not result in a large shift of preference and further strengthens the previously drawn correlations. It is also important to note that the bluff body itself decreases the Ion Detection time by 28.06%, Increases Max Pressure by 6.43% and Ion Velocity by 31.41% for Φ 1.28 in phase #3 and 4 while phase #2 displayed an ion detection time decrease of 15%, and max pressure increase of 16% and flame velocity decrease of 7.5%. The overall effectiveness of the JICF degrades with the addition of the bluff body; however, this is in part due to the turbulence generation of the bluff body decreasing the difference from the baseline.

5 Conclusion

Rig verification indicated the success of achieving detonations using configurations examined by Tate and Gagnon using a valve pulse detonation combustor^{8, 30}. The impact of moving mixtures actually improved the attained ion velocities and pressures slightly while the porous thrust surface had little impact on performance. The greatest takeaway is that for cases with insufficient fuel and air supply total pressures, with a porous thrust surface, the use of frequent physical obstacles leading the DDT section serves to alleviate a significant amount of backflow during blowdown. Furthermore, frequent obstacles are effective at accelerating the deflagrated flame initially, but impede the later acceleration and transition to DDT. The later portions as examined, favor low blockage ratios and greater spacing. Paired with the development of biased streamlined bodies the performance can be significantly increased without imposing excess losses and reduce the supply pressures required.

Overall, the use of a fluid jet in crossflow displays a small mixed ability to increase the performance of a deflagrated flame; additionally, under several conditions the influence can become negative. The orientation of the favorable cases being angled 25° and yawed between 90° and 135° improved the baselines pressure and ion detection times significantly. However, the amount of diluting JICF air necessary is impractical accounting for a bulk mass flow increase of up to 28%, leaning the fuel air mixture, thus increasing the initiation energy required to achieve detonation. In general, the circular jet in crossflow with off normal orientation has merits; however, the performance of a single port falls short of the physical orifice configuration in all categories aside from pressure loss reductions. Furthermore, there exists a need for localized pressure surface to generate favorable gradients that a fluidic technique is unable to provide.

6 Future Work

6.1 Test Rig Improvements

Integration of the bulk air supply with the DAQ for future studies will significantly improve the capabilities of the tests and the quality of data. With the addition of a differential pressure strain gauge on the venturi, thermocouple to monitor the bulk air temperature at the inlet and outlet and power feedback from the VFD, it will further refine the ability to set the mass flow rate and measure the outlet air temperature leading into the test apparatus. Furthermore, using the PWM/A.I. interface on the VFD, the DAQ can also control the mass flow rate of air delivered, increasing the accuracy of the supply and reduce setup time between trials. The final addition to the low pressure bulk air supply would be an industrial resistive heater. This addition would allow active control of the bulk air supply temperature, leading to additional capabilities.

The sampling rate of the current DAQ is 1.25 MHz and divided among active analogue inputs. Employing a dedicated input board with simultaneous analogue inputs and a digital trigger, would improve the resolution. Additional benefits to simultaneous sampling, if sufficient in quantity, could further reduce test iterations or be used to increase the sample size significantly. In this study the sensor measurements were sampled 20-30 times each, in a 60 replication trial.

Fuel supply was only sufficient for mass flow rates of 0.08 kg/s and still transient. The use of a higher flow rate supply or an accumulator tank would increase the possibilities for more, short multicycle burst, higher bulk flow rates and further steady the fuel supply within the cycle. The drawback would be increased fuel usage as purging would be required or the addition of isolation valves. Utilizing liquid fuels driven by a fuel pump and actuated by a valve would be another solution and would expand capabilities.

The use of photo sensors instead of ion probes would improve the measurement accuracy of the test chamber as the probes rely on the chemical reaction to occur in the gap between the anode and cathode. Furthermore, the current ion probes are located on the sidewall of the combustion chamber and the flame front may not be planar and could bypass the sensor for several samples leading to decreased accuracy. This was observed in this study for many deflagration cases as the signal would come and go until sufficiently filled with the reaction region signifying a poor ability to locate the deflagration flame front.

For the weaker pressure waves and acoustic response observed in the study, a different type of pressure sensor is required. The PCB 111A24 dynamic pressure transducers are designed for strong shocks and have a useful range of 0-1000 psi. The tests conducted with the exception of the full stacks were on the order of 5% of the full range. This causes susceptibility of cross channel interference and errors in the readings.

Air supply in the cycle was found to be unfavorable to multicycle operation. The highest achieved cycle time was 18Hz in a 3 shot burst. This is in part due to the inadequate fuel supply and the response from the blower. During the combustion and blowdown phase of the cycle backflow was present. The perforated plate reduced the backflow significantly; however, further reductions are necessary. A properly designed air manifold would significantly improve backflow and shock attenuation.

GE conducted a study investigating multiple points of ignition at the same axial location. The result was shortening the time and distance for the flame kernel(s) to cover, and expand to the full diameter. This method could be utilized to further insure proper ignition and reduce the cycle time.

6.2 Suggested Areas of Investigation

The next successive study, aside from optimizing the addition of reactants and ignition, should focus on designing the required end flow structure, then how to use fluidics or physical obstacles to achieve it efficiently. This would be primarily an analytical study involving CFD and possible validation with visually-based measurements such as PIV or the use of a high speed camera.

- 1st: Fast Flame kernel Expansion
- 2nd: Deflagration Flame Acceleration
- 3rd: Optimize one of several DDT initiation events/mechanisms.
- 4th: Applied cooling schemes where needed

Another suggestion is an investigation into shock reflecting obstacles for the later DDT section, optimizing the physical geometry for a more favorable pressure gradient.

6.3 Fluid Jet Technique

This study has displayed the poor ability of a normal JICF to accelerate the deflagrated flame; however, by using multiple JICFs in a pattern it could serve to break up the coherent vortex structure and further increase the fluid strain rate while decreasing the JICF MR. The additional air should be limited to a practical value, and used sparingly.

7 References

- ¹Knox, B. (2011). The Fluidic Obstacle Technique: An Approach for Enhancing Deflagration-to-Detonation Transition in Pulsed Detonation Engines (Master's Thesis). *Buffalo State University*
- ²Knox, W., Forliti, J. Stevens, A., Hoke, L., Schauer, R. (2010). Unsteady Flame Speed Control and Deflagration-to-Detonation Transition Enhancement using Fluidic Obstacles, *48th Aerospace Sciences Meeting and Exhibit Conference*, (AIAA 2010-151)
- ³McGarry, J., Ahmed, K. (2015). Laminar Deflagrated Flame Interaction With a Fluidic Jet Flow for Deflagration-to-Detonation Flame Acceleration, *51st AIAA/SAE/ASEE Joint Propulsion Conference*, (AIAA 2015-4096).
- ⁴Richter, J. (2011). Accelerating Confined Premixed Flames Using a Traverse Slot Jet (Master's Thesis). *Buffalo State University*
- ⁵Myers, C. (2009). Initiation Mechanisms of Low-Loss Swept Ramp Obstacles for Deflagration To Detonation Transition in Pulse Detonation Combustors (Master's Thesis). *Naval Postgraduate School*
- ⁶Brophy, C., Dvorak, W., Dausen, D., and Myers, C. (2010). Detonation Initiation Improvements using Swept-Ramped Obstacles, *48th AIAA Aerospace Sciences Meeting and Exhibit Conference*, (AIAA 2010-1336)
- ⁷Milanovic, I., Zaman, K. (2003). Highly Inclined Jets in Cross-Flow, *41st Aerospace Sciences and Exhibit Conference*, (AIAA 2003-183)
- ⁸Tate, C. (2015). Investigation of Pulse Detonation Engines; The Effect of Variable Blockage Ration on the Deflagration to Detonation Transition (Master's Thesis). *Embry Riddle Aeronautical University*

- ⁹Vizcaino, J. (2013). Investigation of Pulse Detonation Engines; Theory, Design and Analysis (Master's Thesis). *Embry-Riddle Aeronautical University*
- ¹⁰Bussing, T., Papas, G. (1994). An Introduction to Pulse Detonation Engines, *32nd Aerospace Sciences Meeting and Exhibit Conference*, (AIAA 94-0263)
- ¹¹Braun, E., Belcazar, T., Wilson, D., Lu, F. (2011), Experimental Study of a High-Frequency Fluidic Valve Fuel Injector, *47th AIAA/ASME/SAE/ASEE Joint Propulsion Conference and Exhibit*, (AIAA 2011-5545)
- ¹²Chapman, D., Tangirala, V., Rasheed, A., Dean, A. (2006). Detonation Initiation in Moving Ethylene-Air Mixtures at Elevated Temperature and Pressure, *42nd AIAA/ASME/SAE/ASEE Joint Propulsion Conference and Exhibit*, (AIAA 2006-4793)
- ¹³Paxson, D., Perkins, D. (2004). Thermal Load Considerations for Detonative Combustion-Based Gas Turbine Engines, *40th AIAA/ASME/SAE/ASEE Joint Propulsion Conference and Exhibit*, (AIAA 2004-3396)
- ¹⁴Panicker, P. (2008). The Development and Testing of Pulsed Detonation Engine Ground Demonstrators, *University Arlington Texas*
- ¹⁵Ibrahim, I., Murugappin, S., Gutmark, E. (2005). Penetration, Mixing and Turbulent Structures of Circular and Non-Circular Jets in Cross Flow, *43rd Aerospace Sciences Meeting and Exhibit Conference*, (AIAA 2005-300)
- ¹⁶Shimo, M., Stephen, H. (2006). Multicyclic Detonation Initiation Studies in Valveless Pulsed Detonation Combustors, *42nd AIAA/ASME/SAE/ASEE Joint Propulsion Conference and Exhibit*, (AIAA 2006-4308)

- ¹⁷Schauer, F., Miser, C, Tucker, K. (2005). Detonation Initiation of Hydrocarbon-Air Mixtures in a Pulsed Detonation Engine, *43rd AIAA Aerospace Sciences Meeting and Exhibit*, (AIAA 2005-1343)
- ¹⁸Lee, S., Watts, J., Saretto, S., Pal, S., Conrad, C. Woodward, R., Santoro, R. (2004). Deflagration to Detonation Transition Process by Turbulence-Generating Obstacles in Pulse Detonation Engines, *Journal of Propulsion and Power*, 20(6)
- ¹⁹Rasheed, A., Furman A., and Dean A. (2009). Pressure Measurements and Attenuation in a Hybrid Multitube Pulse Detonation Turbine System, *Journal of Propulsion and Power*, 25(1), 150-161.
- ²⁰Brophy, C., Dvorak, W., Dausen, D., Myers, C. (2010). Detonation Initiation Improvements Using Swept-Ramp Obstacles, *48th Aerospace Sciences Meeting Including the New Horizons Forum and Aerospace Exposition*, (AIAA 2010-1336)
- ²¹Turns, S. (1993). *An Introduction to Combustion Concepts and Applications* (2nd ed., pp. 613). Fairfield, CT: McGraw-Hill Inc.
- ²²Anderson, S., Tonouchi, J., Lidstone, G., Lupkes, K., Alfonso, F. (2004). Performance Trends for a Product Scale Pulse Detonation Engine, *40th AIAA/ASME/SAE/ASEE Joint Propulsion Conference and Exhibit*, (AIAA 2004-3402)
- ²³Knox, B. (2011). The Fluidic Obstacle Technique: An Approach for Enhancing Deflagration-to-Detonation Transition in Pulsed Detonation Engines (Master's Thesis). *Buffalo State University*
- ²⁴McGarry, J., Ahmed, K. (2015). Laminar Deflagrated Flame Interaction with a Fluidic Jet Flow for Deflagration-to-Detonation Flame Acceleration, *51st AIAA/SAE/ASEE Joint Propulsion Conference*, (AIAA 2012-4096)

- ²⁵Steinberg, A., Driscoll, J., Ceccio, S. (2008). Turbulence-Flame Interaction – the Mechanisms of Flame Strain and Wrinkling, *44th AIAA/ASME/SAE/ASEE Joint Propulsion Conference*, (AIAA 2008-4572)
- ²⁶Cooper, M., Jewel, J., Shepherd J. (2003). The Effect of a Porous Thrust Surface on Detonation Tube Impulse, *39th AIAA/ASME/SAE/ASEE Joint Propulsion Conference*, (AIAA 2003-4822)
- ²⁷Chambers, J., McGarry J., Ahmed, K. (2016). Fluidic Jet Augmentation of a Deflagrated Turbulent Flame for Deflagration-to-Detonation, *54th AIAA Aerospace Sciences Meeting*, (AIAA 2016-0443)
- ²⁸Hoke, J., Bradley, R. (2006). The Impact of Detonation Initiation Techniques on Thrust in a Pulsed Detonation Engine, *44th AIAA Aerospace Sciences Meeting and Exhibit*, (AIAA 2006-1023)
- ²⁹Morozumi, T., Matsuoka, R., Sakamoto, R., Fujiwara, Y., Kasahara, J. (2013). Study on a Four-Cylinder Pulse Detonation Rocket Engine with a Coaxial High Frequency Rotary Valve, *51st AIAA Aerospace Sciences Meeting Including the New Horizons Forum and Aerospace Exposition*, (AIAA 2013-0279)
- ³⁰Gagnon, N. (2016). The Effect of Axial Spacing of Constant and Variable Blockages on the Deflagration to Detonation Transition in a Pulse Detonation Engine, *Embry Riddle Aeronautical University*
- ³¹Zieffle, J., Kleiser, L. (2006). Large-Eddie Simulation of a Round Jet in Crossflow, *36th AIAA Fluid Dynamics Conference and Exhibit*, (AIAA2006-3370)
- ³²Sun, G., Akbari, P., Gower, B., Muller, N. (2012). Thermodynamics of Wave Disk Engine, *48th AIAA/ASME/SAE/ASEE Joint Propulsion Conference*, (AIAA 2012-3704)
- ³³Heiser, W., Pratt, D. (2002). Thermodynamic Cycle Analysis of Pulse Detonation Engines, *Journal of Propulsion and Power*, vol. 18(1), pp 62-76.

A. Hardware Information

A.1 PX329

Omega: PX329-100A5V

SSN #: 082014I095

Pressure Range: 0-100 psia

Excitation: 9-30 Vdc

Temperature Range: -20 to +85 C

Connection: ¼-18 NPT Male

Balance: 0.012 Vdc


Sensitivity: 5.002 Vdc/100psia

Static Accuracy: 0.25% Full Span, ~ 0.25 psi

Table 9 PX329 Factory Calibration Information

Pressure	Unite Data
psia	Vdc
0.00	0.012
50.00	2.514
100.00	5.014
50.00	2.515
0.00	0.012
Excitation	28.000


A.2 PCB 111A24

Model Number 111A24		ICP® PRESSURE SENSOR		Revision: L ECN #: 40791																																												
Performance	ENGLISH	SI																																														
Measurement Range(for ±5V output) Useful Overrange(for ±10V output) Sensitivity(± 0.5 mV/psi) Maximum Pressure(static) Resolution Resonant Frequency Rise Time(Reflected) Low Frequency Response(5%) Non-Linearity	1 kpsi 2 kpsi 5.0 mV/psi 10 kpsi 20 mpsi ≥ 400 kHz ≤ 1.5 µ sec 0.005 Hz ≤ 2.0 % FS	6895 kPa 13,790 kPa 0.73 mV/kPa 68,950 kPa 0.14 kPa ≥ 400 kHz ≤ 1.5 µ sec 0.005 Hz ≤ 2.0 % FS	[1]																																													
Environmental				[2]																																												
Acceleration Sensitivity Temperature Range(Operating) Temperature Coefficient of Sensitivity Maximum Flash Temperature Maximum Vibration Maximum Shock	<0.002 psig/g -100 to +275 °F ≤ 0.2 %/°F 3000 °F 2000 g pk 20,000 g pk	<0.0014 kPa/(m/s ²) -73 to +135 °C ≤ 0.36 %/°C 1649 °C 19,614 m/s ² pk 196,140 m/s ² pk																																														
Electrical																																																
Output Polarity(Positive Pressure) Discharge Time Constant(at room temp) Excitation Voltage Constant Current Excitation Output Impedance Output Bias Voltage	Positive ≥ 100 sec 20 to 30 VDC 2 to 20 mA ≤ 100 Ohm 8 to 14 VDC	Positive ≥ 100 sec 20 to 30 VDC 2 to 20 mA ≤ 100 Ohm 8 to 14 VDC																																														
Physical																																																
Sensing Geometry Sensing Element Housing Material Diaphragm Sealing Electrical Connector Weight	Compression Quartz 17-4 Stainless Steel Invar Epoxy 10-32 Coaxial Jack 0.21 oz	Compression Quartz 17-4 Stainless Steel Invar Epoxy 10-32 Coaxial Jack 6 gm																																														
<p>OPTIONAL VERSIONS</p> <p>Optional versions have identical specifications and accessories as listed for the standard model except where noted below. More than one option may be used.</p> <table border="0"> <tr> <td>E - Enrronlon coating</td> <td>Enrronlon</td> <td>Enrronlon</td> <td>[4]</td> </tr> <tr> <td>Electrical Isolation</td> <td>10⁸ Ohm</td> <td>10⁸ Ohm</td> <td></td> </tr> <tr> <td>Supplied Accessory : Model 065A08 Isolation ring 0.250"OD x 0.218" ID x 0.027" thk anodized aluminum (3)</td> <td></td> <td></td> <td></td> </tr> <tr> <td>Supplied Accessory : Model 065A22 Isolation Seal, .250" OD x .218" ID x .015", Torton or Vespel (3)</td> <td></td> <td></td> <td></td> </tr> <tr> <td>H - Hermetic Seal</td> <td>Welded Hermetic</td> <td>Welded Hermetic</td> <td>[4]</td> </tr> <tr> <td>Sealing</td> <td></td> <td></td> <td></td> </tr> <tr> <td>J - Ground Isolated</td> <td></td> <td></td> <td>[4][5]</td> </tr> <tr> <td>N - Negative Output Polarity</td> <td></td> <td></td> <td>[4]</td> </tr> <tr> <td>S - Stainless Steel Diaphragm</td> <td>316L Stainless Steel</td> <td>316L Stainless Steel</td> <td>[4]</td> </tr> <tr> <td>Diaphragm</td> <td></td> <td></td> <td></td> </tr> <tr> <td>W - Water Resistant Cable</td> <td></td> <td></td> <td>[4]</td> </tr> </table>					E - Enrronlon coating	Enrronlon	Enrronlon	[4]	Electrical Isolation	10 ⁸ Ohm	10 ⁸ Ohm		Supplied Accessory : Model 065A08 Isolation ring 0.250"OD x 0.218" ID x 0.027" thk anodized aluminum (3)				Supplied Accessory : Model 065A22 Isolation Seal, .250" OD x .218" ID x .015", Torton or Vespel (3)				H - Hermetic Seal	Welded Hermetic	Welded Hermetic	[4]	Sealing				J - Ground Isolated			[4][5]	N - Negative Output Polarity			[4]	S - Stainless Steel Diaphragm	316L Stainless Steel	316L Stainless Steel	[4]	Diaphragm				W - Water Resistant Cable			[4]
E - Enrronlon coating	Enrronlon	Enrronlon	[4]																																													
Electrical Isolation	10 ⁸ Ohm	10 ⁸ Ohm																																														
Supplied Accessory : Model 065A08 Isolation ring 0.250"OD x 0.218" ID x 0.027" thk anodized aluminum (3)																																																
Supplied Accessory : Model 065A22 Isolation Seal, .250" OD x .218" ID x .015", Torton or Vespel (3)																																																
H - Hermetic Seal	Welded Hermetic	Welded Hermetic	[4]																																													
Sealing																																																
J - Ground Isolated			[4][5]																																													
N - Negative Output Polarity			[4]																																													
S - Stainless Steel Diaphragm	316L Stainless Steel	316L Stainless Steel	[4]																																													
Diaphragm																																																
W - Water Resistant Cable			[4]																																													
<p>NOTES:</p> <p>[1] For +10 volt output, minimum 24 VDC supply voltage required. Negative 10 volt output may be limited by output bias.</p> <p>[2] Zero-based, least-squares, straight line method.</p> <p>[3] See PCB Declaration of Conformance PS023 for details.</p> <p>[4] For sensor mounted in thread adaptor, see adaptor installation drawing for supplied accessories.</p> <p>[5] Used with optional mounting adaptor.</p>																																																
<p>SUPPLIED ACCESSORIES:</p> <p>Model 060A03 Clamp nut, 5/16-24-2A thd, 1/4" hex, stainless steel (1)</p> <p>Model 060A05 Clamp nut M7 x 0.75-5g thd (1)</p> <p>Model 065A02 Seal ring, sensor flush mount, 0.248" OD x 0.219" ID x 0.015" thk, brass (3)</p> <p>Model 065A05 Seal sleeve sensor recess mount 0.248" OD x 0.221" ID x 0.240" thk 17-4 (1)</p>																																																
Entered: AP	Engineer: MAJ	Sales: KWW	Approved: BAM	Spec Number:																																												
Date: 3/19/2013	Date: 3/19/2013	Date: 3/19/2013	Date: 3/19/2013	111-1240-80																																												
 <p>PCB PIEZOTRONICS™</p> <p>3425 Walden Avenue, Depew, NY 14043</p> <p>Phone: 716-684-0001 Fax: 716-684-0987 E-Mail: info@pcb.com</p>																																																

All specifications are at room temperature unless otherwise specified.
In the interest of constant product improvement, we reserve the right to change specifications without notice.
ICP® is a registered trademark of PCB Group, Inc.



A.3 PCB 482C05

Model Number 482C05		FOUR-CHANNEL, ICP® SENSOR SIGNAL CONDITIONER		Revision: J EON #: 43617
Performance		ENGLISH	SI	
Channels		4	4	
Sensor Input Type(s)		ICP®	ICP®	
Output Range(Maximum)		± 10 V	± 10 V	
Low Frequency Response(-5%)		<0.1 Hz	<0.1 Hz	[2][3]
High Frequency Response(-5%)		>1000 kHz	>1000 kHz	
Phase Response(at 1 kHz)		± 1°	± 1°	
Cross Talk(maximum)		-72 dB	-72 dB	
Fault/Bias Monitor/Meter(LED)		Open/Short/Overload	Open/Short/Overload	
Environmental				
Temperature Range(Operating)		+32 to +120 °F	0 to +50 °C	
Electrical				
Power Required(for supplied AC power adaptor)		AC Power	AC Power	
Power Required(direct input to unit)		DC power	DC power	
AC Power(47 to 63 Hz)		100 to 240 VAC	100 to 240 VAC	
AC Power		≤ 0.7 Amps	≤ 0.7 Amps	
Excitation Voltage(± 1 VDC)(To Sensor)		+26 VDC	+26 VDC	
DC Offset		<20 mV	<20 mV	
DC Power		+32 to 38 VDC	+32 to 38 VDC	
DC Power		<0.25 Amps	<0.25 Amps	[1]
Constant Current Excitation(To Sensor)		2 to 20 mA	2 to 20 mA	
Overload Threshold(± 1.0 Vpk)		± 10 Vpk	± 10 Vpk	
Discharge Time Constant(0 to 50%)		>5 sec	>5 sec	[2][3]
Broadband Electrical Noise(1 to 10,000 Hz)		3.5 µV/ms	3.5 µV/ms	[4]
Spectral Noise(1 Hz)		1.30 µV/√Hz	1.30 µV/√Hz	[4]
Spectral Noise(10 Hz)		0.10 µV/√Hz	0.10 µV/√Hz	[4]
Spectral Noise(100 Hz)		0.08 µV/√Hz	0.08 µV/√Hz	[4]
Spectral Noise(1 kHz)		0.07 µV/√Hz	0.07 µV/√Hz	[4]
Spectral Noise(10 kHz)		0.07 µV/√Hz	0.07 µV/√Hz	[4]
Physical				
Electrical Connector(ICP® Sensor Input)		BNC Jack	BNC Jack	
Electrical Connector(Output)		BNC Jack	BNC Jack	
Electrical Connector(DC Power Input)		5-socket DIN (female)	5-socket DIN (female)	
Size (Height x Width x Depth)		3.2 in x 8.0 in x 5.9 in	8.1 cm x 20 cm x 15 cm	
Weight		1.25 lb	567 gm	
		OPTIONAL VERSIONS		
		Optional versions have identical specifications and accessories as listed for the standard model except where noted below. More than one option may be used.		
		NOTES:		
		[1] User adjustable, factory set at 4 mA (± 0.5 mA). One control adjusts all channels.		
		[2] With ≥ 1M ohm input impedance of readout device.		
		[3] Un-buffered output, read out device input impedance affects discharge time constant and low frequency response of unit.		
		[4] Typical.		
		[5] See PCB Declaration of Conformance PS024 for details.		
		SUPPLIED ACCESSORIES:		
		Model 017AXX Power Cord		
		Model 489B04/NC Power Converter		
Entered: AP	Engineer: CPH	Sales: ML	Approved: JWH	Spec Number:
Date: 1/28/2015	Date: 1/28/2015	Date: 1/28/2015	Date: 1/28/2015	35061
		PCB PIEZOTRONICS ™		
3425 Walden Avenue, Depew, NY 14043		Phone: 716-684-0001		
		Fax: 716-684-0987		
		E-Mail: info@pcb.com		

All specifications are at room temperature unless otherwise specified.
In the interest of constant product improvement, we reserve the right to change specifications without notice.
ICP® is a registered trademark of PCB Group, Inc.



A.4 10Vdc Precision Power Supply

IC PMIC: AD582KNZ-ND 0.05% Tolerance

Transistor: 2N6040GOS-ND

Resistor: PPC200W-1CT-ND

Supply Voltage Capacitor: 0.47 μ f 400V 3% Panasonic Polypropylene Film Capacitor. Connected in parallel between the GND and the +V_{in}

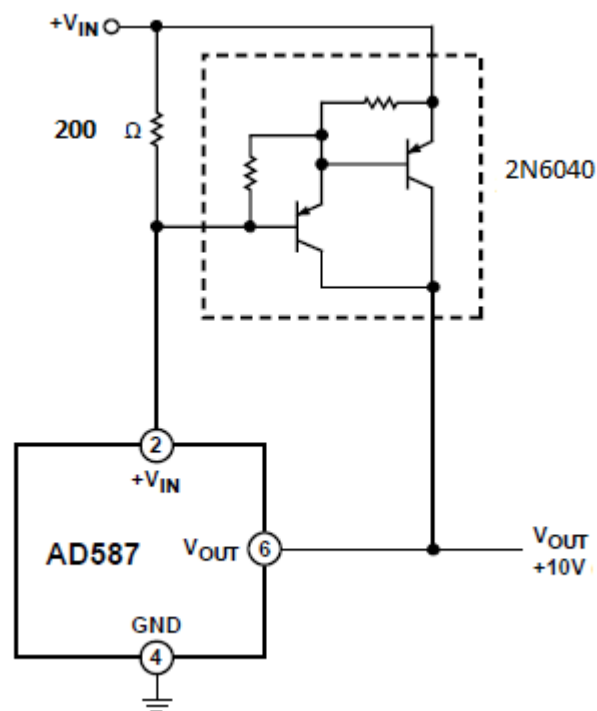


Figure 78 AD587 10VDC Precision Power Supply, Information provided by Analogue Devices

B. Condensed Test Information

B.1 Phase #1

Table 10 DDT Configurations M_{air} 0.0539, RE 25455 fill air

Case	DDT %	Ion Time ms		P_{max} Psi		Post Psi		Ion Velocity m/s		Φ
X/D	23-38	23.81	37.87	23.81	37.87	23.81	37.87	24.98	36.70	FI
Stack0	0	10.277	13.175	7.27	12.45	7.27	12.71	145	325	0.935
Stack1	0	5.272	6.049	199.22	79.72	65.70	28.61	779	684	1.058
Stack3	15	5.773	6.377	210.44	353.78	60.74	47.55	1011	1109	0.964
Stack4	0	7.392	8.071	90.48	337.06	41.30	50.22	617	1135	1.021
Stack5	10	8.166	9.009	74.18	177.26	33.23	51.81	725	924	0.956
Stack6	0	8.515	9.419	83.48	194.44	27.73	38.76	748	821	0.975
Stack0	0	8.403	10.828	16.53	24.76	16.53	21.14	183	358	1.193
Stack1	0	4.715	5.318	236.81	195.41	70.68	39.43	772	1078	1.212
Stack3	96.667	4.765	5.144	285.11	328.83	68.30	62.26	1512	1542	1.233
Stack4	100	6.332	6.805	151.92	615.23	60.61	64.85	906	2149	1.228
Stack5	100	6.782	7.388	110.44	766.46	50.07	65.39	1057	1427	1.212
Stack6	40	6.902	7.417	216.65	725.46	49.59	57.52	909	1981	1.190

B.2 Phase #2

Table 11 Phase 2 Orifice M_{air} 0.0539 kg/s

M_{air} 0.0539 kg/s		Ion Time ms		Pmax Pressure Psi		Ion Velocity m/s		Φ
X/D		23.58	35.95	23.58	35.95	24.61	34.92	FI
Comb	BR01	7.985	10.653	12.28	14.79	286	282	0.940
Comb	BR03	7.594	10.019	17.83	22.63	384	269	0.931
Comb	BR05	7.463	10.138	23.92	30.64	317	291	0.902
Single	BR00	10.030	13.341	9.05	8.68	278	251	0.983
Single	BR01	9.041	11.892	13.44	14.73	307	258	0.964
Single	BR03	8.788	11.520	18.84	21.69	289	268	0.925
Single	BR05	9.030	11.820	22.25	27.39	313	266	0.885
Comb	BR00	6.839	9.125	17.21	20.98	337	372	1.264
Comb	BR01	6.560	8.159	20.21	34.41	422	417	1.258
Comb	BR03	5.989	7.612	35.16	39.62	500	372	1.252
Comb	BR05	5.929	7.820	52.98	51.69	459	308	1.201
Single	BR00	8.036	10.681	14.81	17.77	364	277	1.271
Single	BR01	7.181	8.857	20.50	29.92	415	393	1.274
Single	BR03	6.646	8.513	41.97	47.83	426	341	1.246
Single	BR05	6.803	8.643	57.39	55.96	401	338	1.216

Table 12 Phase 2 Orifice M_{air} 0.0763 kg/s

M_{air} 0.0763 kg/s		Ion Time ms		P_{max} Pressure Psi		Ion Velocity m/s		Φ
X/D		23.58	35.95	23.58	35.95	24.61	34.92	FI
Comb	BR01	7.034	9.725	11.91	13.76	280	265	1.030
Comb	BR03	6.755	9.017	14.23	16.82	418	297	1.010
Comb	BR05	6.239	8.472	19.80	23.90	301	355	1.003
Single	BR00	6.587	9.081	21.22	26.51	355	323	0.948
Single	BR01	8.617	11.541	10.49	10.92	298	236	1.044
Single	BR03	7.752	10.239	14.24	15.77	381	350	1.025
Single	BR05	7.199	9.702	20.22	22.66	334	302	1.007
Comb	BR00	7.672	10.178	21.58	24.93	299	292	0.959
Comb	BR01	5.887	7.677	18.70	24.27	393	468	1.308
Comb	BR03	5.027	6.700	39.77	42.30	446	358	1.292
Comb	BR05	5.008	6.755	51.48	52.97	472	342	1.265
Single	BR00	7.044	9.212	17.63	21.18	418	284	1.311
Single	BR01	6.220	7.863	24.77	34.21	502	462	1.310
Single	BR03	5.759	7.465	47.25	49.60	436	358	1.300
Single	BR05	5.868	7.531	54.54	53.56	439	351	1.280

The above table displays pertinent information of interest for comparisons. Station 1, $X/D = 23.6$, is most beneficial in determine the blowdown time reduction from the transition geometry as it is the shortest length and furthermore interference from upstream perturbations will be minimized such as additional protrusion of ion probes.

B.3 Phase #3

Table 13 JICF M_{air} 0.0539 kg/s, Re 25400 fill air

Case	MR	Ion Time ms		P_{max} Psi		Ion Velocity m/s		Φ	
X/D		21.40	33.78	21.40	33.78	22.43	32.75	FI	Diluted
JICF00	0.000	12.353	15.390	6.24	8.19	119	370	0.940	0.940
JICF00	0.000	9.131	11.206	13.39	22.68	227	619	1.277	1.277
JICF00	0.000	9.496	12.274	14.02	18.42	134	428	1.233	1.233
JICF10	0.824	11.775	14.761	7.72	9.68	125	386	0.955	0.898
JICF10	1.301	11.596	14.411	7.86	10.15	138	439	0.967	0.880
JICF10	1.843	11.280	14.304	8.98	11.32	115	394	0.973	0.852
JICF10	2.449	11.049	14.017	9.05	11.80	127	425	0.979	0.825
JICF10	3.855	10.768	13.789	10.25	12.84	117	440	0.985	0.760
JICF20	0.824	11.309	14.063	8.87	11.23	145	381	0.971	0.913
JICF20	1.301	11.125	13.878	9.23	12.08	138	394	0.976	0.888
JICF20	1.843	10.802	13.541	10.29	13.45	140	411	0.979	0.858
JICF20	2.449	10.549	13.428	10.77	14.05	133	396	0.980	0.825
JICF20	3.855	10.396	13.240	12.72	16.77	143	378	0.982	0.758
JICF20	5.518	10.144	12.902	13.70	18.29	147	409	0.986	0.693
JICF30	1.301	11.069	13.920	9.16	12.24	143	408	0.985	0.895
JICF30	2.449	10.684	13.541	10.98	15.15	147	342	0.989	0.833

JICF30	3.855	10.410	13.186	12.47	16.68	144	417	0.994	0.767
JICF40	0.824	12.050	14.925	7.04	8.83	157	382	0.961	0.904
JICF40	1.301	11.692	14.497	7.74	10.16	150	408	0.972	0.884
JICF40	1.843	11.519	14.317	8.53	11.28	156	388	0.975	0.854
JICF40	2.449	11.355	14.302	8.17	10.29	143	455	0.966	0.814
JICF40	3.855	11.210	14.165	8.68	11.61	135	437	0.965	0.745
JICF50	3.855	11.354	14.463	8.27	10.92	149	440	0.978	0.755
JICF60	0.824	12.195	15.492	6.53	8.01	117	429	0.952	0.896
JICF60	1.301	12.201	15.445	6.58	8.64	124	415	0.952	0.866
JICF60	1.843	12.093	15.306	6.69	7.87	133	458	0.953	0.835
JICF60	2.449	12.123	15.384	6.80	8.45	136	557	0.954	0.803
JICF60	3.855	12.104	15.431	7.29	8.12	133	415	0.954	0.737
JICF10	3.855	9.031	11.753	16.31	23.73	163	420	1.275	0.984
JICF20	3.855	8.954	11.532	19.39	24.06	180	429	1.243	0.960
JICF30	3.855	8.971	11.562	18.48	27.12	172	499	1.249	0.964
JICF40	3.855	9.112	11.664	17.04	21.19	194	428	1.263	0.975

Table 14 JICF M_{air} 0.0764 kg/s, Re 35756 fill air

Case	MR	Ion Time ms		P _{max} Psi		Ion Velocity m/s		Φ		
		X/D		21.40	33.78	21.40	33.78	22.43	32.75	FI
JICF00	0.000		10.343	13.541	8.43	11.51	182	371	1.012	1.012
JICF10	0.408		10.106	13.244	8.47	11.89	177	307	1.020	0.976
JICF10	0.645		10.199	13.415	8.44	11.79	168	357	1.019	0.952
JICF10	0.914		10.006	13.180	8.70	12.11	196	291	1.024	0.931
JICF10	1.215		9.871	13.149	9.19	12.61	168	411	1.026	0.906
JICF10	1.911		9.614	12.983	9.48	13.33	148	438	1.029	0.851
JICF20	0.408		9.759	12.901	9.02	11.67	188	316	1.041	0.996
JICF20	0.645		9.807	12.859	9.40	13.08	231	332	1.042	0.973
JICF20	0.914		9.615	12.688	9.44	13.21	203	310	1.043	0.949
JICF20	1.215		9.376	12.510	9.71	13.80	210	314	1.044	0.922
JICF20	1.911		9.325	12.366	10.82	15.03	226	349	1.048	0.867
JICF20	2.736		9.052	12.090	11.52	15.71	223	334	1.047	0.806
JICF40	0.408		9.904	13.082	8.91	12.27	184	392	1.040	0.996
JICF40	0.645		9.982	13.028	9.06	12.16	238	352	1.041	0.972
JICF40	0.914		9.980	12.929	9.13	12.62	232	359	1.043	0.949
JICF40	1.215		9.746	12.777	9.39	12.99	213	350	1.044	0.922
JICF40	1.911		9.523	12.687	9.97	13.49	208	290	1.046	0.865
JICF60	0.408		10.163	13.420	8.53	11.44	219	424	1.031	0.987
JICF60	0.645		10.193	13.271	8.89	12.06	196	378	1.032	0.964
JICF60	0.914		10.091	13.240	8.72	11.64	222	361	1.034	0.940
JICF60	1.215		9.909	13.264	8.85	11.81	198	348	1.035	0.913
JICF60	1.911		10.095	13.329	9.00	11.86	188	301	1.035	0.856

Table 15 JICF M_{air} 0.0539 kg/s, Re 25400 fill air

Case	MR	Ion Time ms		P_{max} Psi		Ion Velocity m/s		Φ			
		X/D		21.40	33.78	21.40	33.78	22.43	32.75	FI	Diluted
JICF00	0			12.353	15.390	6.24	8.19	119	370	0.940	0.940
JICF00	0			9.437	12.044	15.29	21.03	178	451	1.277	1.277
JICF01	3.855			10.682	14.143	10.59	10.63	120	355	0.966	0.746
JICF02	3.855			9.892	12.783	12.70	13.72	153	389	0.994	0.767
JICF03	3.855			10.040	13.068	13.80	13.80	135	413	0.980	0.756
JICF04	3.855			10.914	13.594	11.90	13.86	167	348	0.977	0.754
JICF05	3.855			16.093	14.413	9.61	10.89	101	379	0.972	0.750
JICF06	3.855			10.949	14.523	8.75	9.54	114	458	0.969	0.748
JICF10	3.855			11.466	14.650	8.50	11.64	123	473	0.955	0.737
JICF20	3.855			10.578	13.425	11.67	16.24	142	394	0.989	0.763
JICF30	3.855			10.724	13.449	11.21	15.45	150	400	1.002	0.774
JICF40	3.855			11.055	14.102	8.85	12.07	155	436	0.986	0.761
JICF50	3.855			11.580	14.742	7.65	10.18	134	436	0.981	0.757
JICF60	3.855			11.694	14.949	7.97	9.98	141	469	0.987	0.762
JICF01	3.855			8.422	11.143	13.17	26.86	190	452	1.280	0.988
JICF02	3.855			8.484	10.882	17.04	31.28	204	446	1.285	0.992
JICF03	3.855			8.115	10.863	17.58	29.68	200	379	1.281	0.989
JICF04	3.855			8.194	11.012	13.19	30.68	179	390	1.272	0.982
JICF05	3.855			8.535	11.256	11.69	32.79	180	512	1.272	0.981
JICF06	3.855			8.421	11.450	12.82	24.81	185	402	1.265	0.977
JICF10	3.855			8.856	11.603	16.70	22.50	145	397	1.267	0.978
JICF20	3.855			8.798	11.383	19.50	23.70	187	410	1.276	0.985
JICF30	3.855			8.934	11.454	18.88	25.28	187	422	1.274	0.983
JICF40	3.855			9.095	11.711	16.51	21.01	188	413	1.264	0.976
JICF50	3.855			9.209	11.927	15.53	19.80	229	395	1.263	0.975
JICF60	3.855			9.292	12.240	14.13	18.71	167	416	1.256	0.969

Table 16 JICF M_{air} 0.0764 kg/s, Re 35756 fill air

Case	MR_{jet}	Ion Time ms		P_{max} Psi		Ion Velocity m/s		Φ			
		X/D		21.40	33.78	21.40	33.78	22.43	32.75	FI	Diluted
JICF00	0.000			8.253	11.066	14.18	20.05	252	358	1.293	1.293
JICF01	1.911			7.542	10.259	9.82	13.39	223	305	1.299	1.075
JICF02	1.911			7.353	9.838	9.91	16.53	278	317	1.302	1.077
JICF03	1.911			7.244	9.987	9.57	15.49	244	266	1.301	1.077
JICF04	1.911			7.359	9.966	11.63	13.17	223	269	1.303	1.077
JICF05	1.911			7.475	10.308	9.68	14.64	219	330	1.302	1.077
JICF06	1.911			7.451	10.178	11.48	13.11	231	278	1.293	1.070
JICF10	1.911			7.760	10.614	13.35	17.87	227	291	1.310	1.083
JICF20	1.911			7.637	10.306	13.40	21.31	272	260	1.314	1.087
JICF30	1.911			7.663	10.341	14.10	23.60	309	271	1.310	1.084
JICF40	1.911			7.922	10.526	13.68	19.98	304	270	1.309	1.083
JICF50	1.911			8.000	10.737	11.75	18.71	300	312	1.298	1.074
JICF60	1.911			7.927	10.788	14.37	18.25	231	334	1.314	1.087

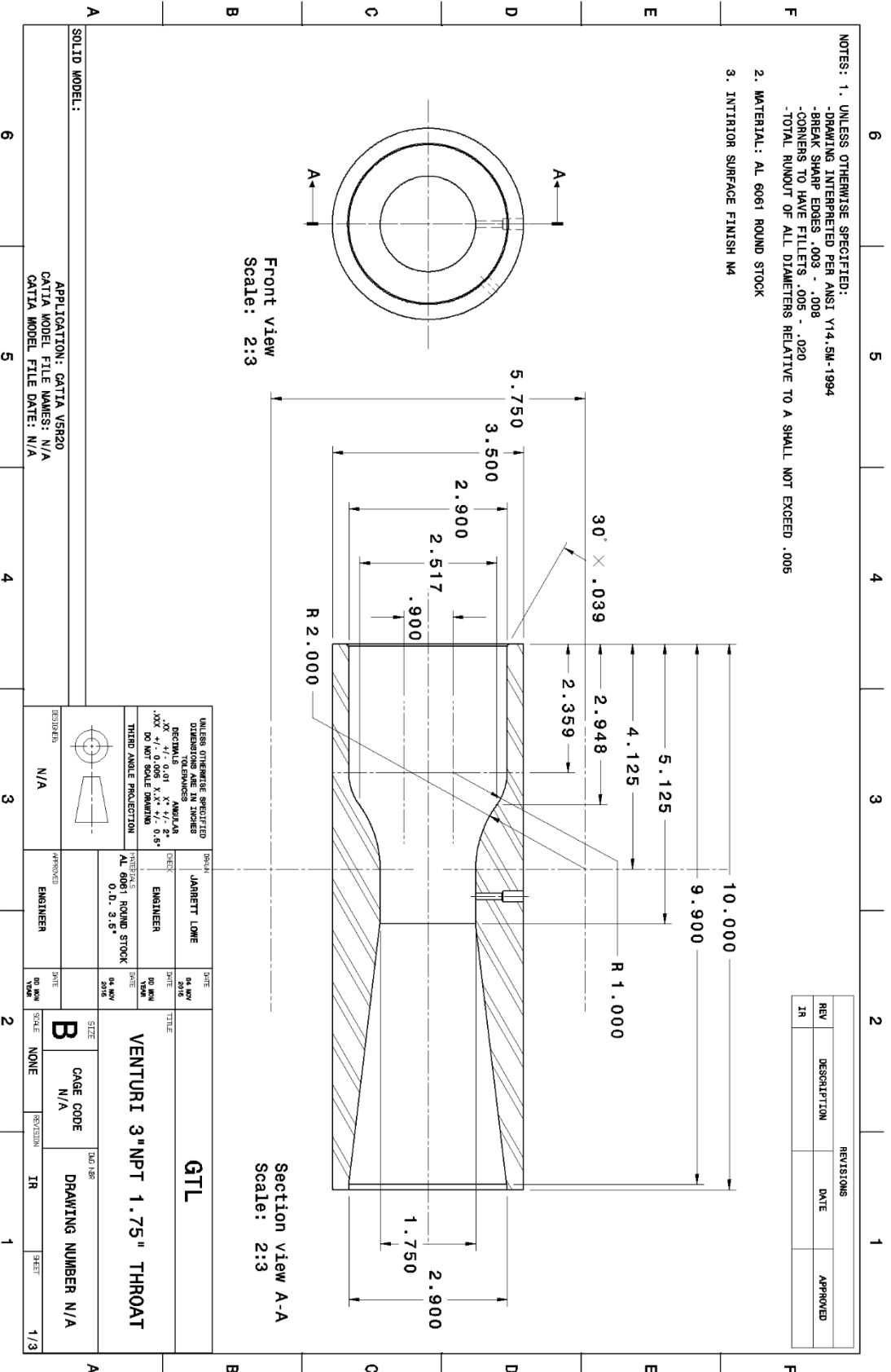
B.4 Phase #4

Table 17 Hybrid M_{air} 0.0539 kg/s, Re 25344 fill air

Case	MR	Ion Time ms		P_{max} Psi		Ion Velocity m/s		Φ	
		X/D		21.40	33.78	22.43	32.75	FI	Diluted
JICF00	0.000	8.161	11.196	12.49	14.44	187	313	1.000	1.000
JICF00	0.000	6.788	9.220	16.27	27.74	234	332	1.279	1.279
JICF01	2.452	7.719	10.934	13.90	20.46	161	317	1.015	0.854
JICF01	3.859	7.938	11.426	13.62	20.83	148	294	0.980	0.757
JICF02	2.452	7.673	10.630	14.47	26.49	205	310	1.016	0.856
JICF02	3.859	7.637	10.533	16.52	29.79	184	347	1.006	0.776
JICF03	2.452	7.640	10.683	14.69	26.75	166	411	1.015	0.854
JICF03	3.859	7.456	10.349	15.74	31.08	196	388	1.011	0.780
JICF04	2.452	7.707	10.799	14.65	24.89	165	265	1.011	0.851
JICF04	3.859	7.653	10.673	15.30	25.86	196	323	1.000	0.772
JICF05	2.452	8.187	11.314	13.23	17.31	151	307	1.006	0.847
JICF05	3.859	8.231	11.197	13.79	20.31	160	313	0.999	0.771
JICF06	2.452	7.822	11.254	12.66	18.40	159	242	0.999	0.841
JICF06	3.859	7.879	11.384	13.16	15.91	153	283	0.993	0.766
JICF10	2.452	8.057	11.186	13.00	15.02	203	243	0.993	0.836
JICF10	3.859	7.839	10.921	13.70	15.99	208	281	1.015	0.784
JICF20	2.452	7.852	10.874	13.26	17.24	226	259	0.987	0.831
JICF20	3.859	7.772	10.672	13.87	18.66	236	276	0.996	0.769
JICF30	2.452	7.988	11.088	12.73	16.81	247	262	0.988	0.832
JICF30	3.859	7.876	10.887	14.14	18.32	243	281	0.992	0.766
JICF40	2.452	8.129	11.101	12.54	15.64	283	244	0.982	0.827
JICF40	3.859	7.939	11.060	12.99	16.58	263	253	0.990	0.764
JICF50	2.452	7.770	10.830	12.85	17.67	217	276	1.041	0.876
JICF50	3.859	7.769	10.869	13.36	17.91	226	253	1.045	0.806
JICF60	2.452	8.050	11.222	12.24	14.62	208	290	1.024	0.862
JICF60	3.859	7.938	11.120	12.84	14.60	225	267	1.035	0.799
JICF01	2.452	6.529	8.975	18.65	32.45	240	313	1.279	1.076
JICF01	3.859	6.484	8.886	20.24	25.93	226	353	1.282	0.989
JICF02	2.452	6.633	9.027	20.81	29.26	254	304	1.286	1.083
JICF02	3.859	6.512	8.800	21.01	30.22	252	330	1.290	0.996
JICF03	2.452	6.529	9.024	19.44	29.08	229	343	1.289	1.085
JICF03	3.859	6.389	8.524	22.09	26.20	295	374	1.293	0.998
JICF04	2.452	6.430	8.849	19.64	25.75	223	332	1.276	1.074
JICF04	3.859	6.299	8.590	21.23	25.18	260	349	1.281	0.988
JICF05	2.452	6.663	9.167	18.04	27.11	222	293	1.273	1.072
JICF05	3.859	6.643	8.934	19.32	24.68	216	313	1.278	0.986
JICF06	2.452	6.540	9.110	17.26	31.29	224	251	1.269	1.069
JICF06	3.859	6.454	9.082	18.64	27.80	206	315	1.271	0.981
JICF10	2.452	6.551	8.927	17.90	24.88	252	282	1.305	1.099
JICF10	3.859	6.466	8.811	18.52	24.90	250	337	1.310	1.011
JICF20	2.452	6.565	8.908	19.53	26.14	252	291	1.301	1.095
JICF20	3.859	6.572	8.896	20.39	28.95	288	283	1.317	1.017
JICF30	2.452	6.659	8.981	18.86	26.63	288	284	1.297	1.092
JICF30	3.859	6.604	9.057	19.37	28.54	279	372	1.307	1.008

JICF40	2.452	6.556	8.931	18.30	24.53	266	271	1.296	1.091
JICF40	3.859	6.548	8.944	18.41	24.68	236	306	1.303	1.006
JICF50	2.452	6.628	9.053	17.36	24.91	282	268	1.298	1.093
JICF50	3.859	6.609	9.098	17.64	26.69	273	251	1.300	1.003
JICF60	2.452	6.702	9.159	17.18	24.47	260	284	1.299	1.093
JICF60	3.859	6.651	9.171	17.42	23.16	251	271	1.302	1.004

C. Part Drawings



NOTES: 1. UNLESS OTHERWISE SPECIFIED:
 -DRAWING INTERPRETED PER ANSI Y14.5M-1994
 -BREAK SHARP EDGES .003 - .008
 -CORNERS TO HAVE FILLETS .005 - .020
 -TOTAL RUNOUT OF ALL DIAMETERS RELATIVE TO A SHALL NOT EXCEED .005

- 2. MATERIAL: AL 6061 ROUND STOCK
- 3. INTERIOR SURFACE FINISH M4

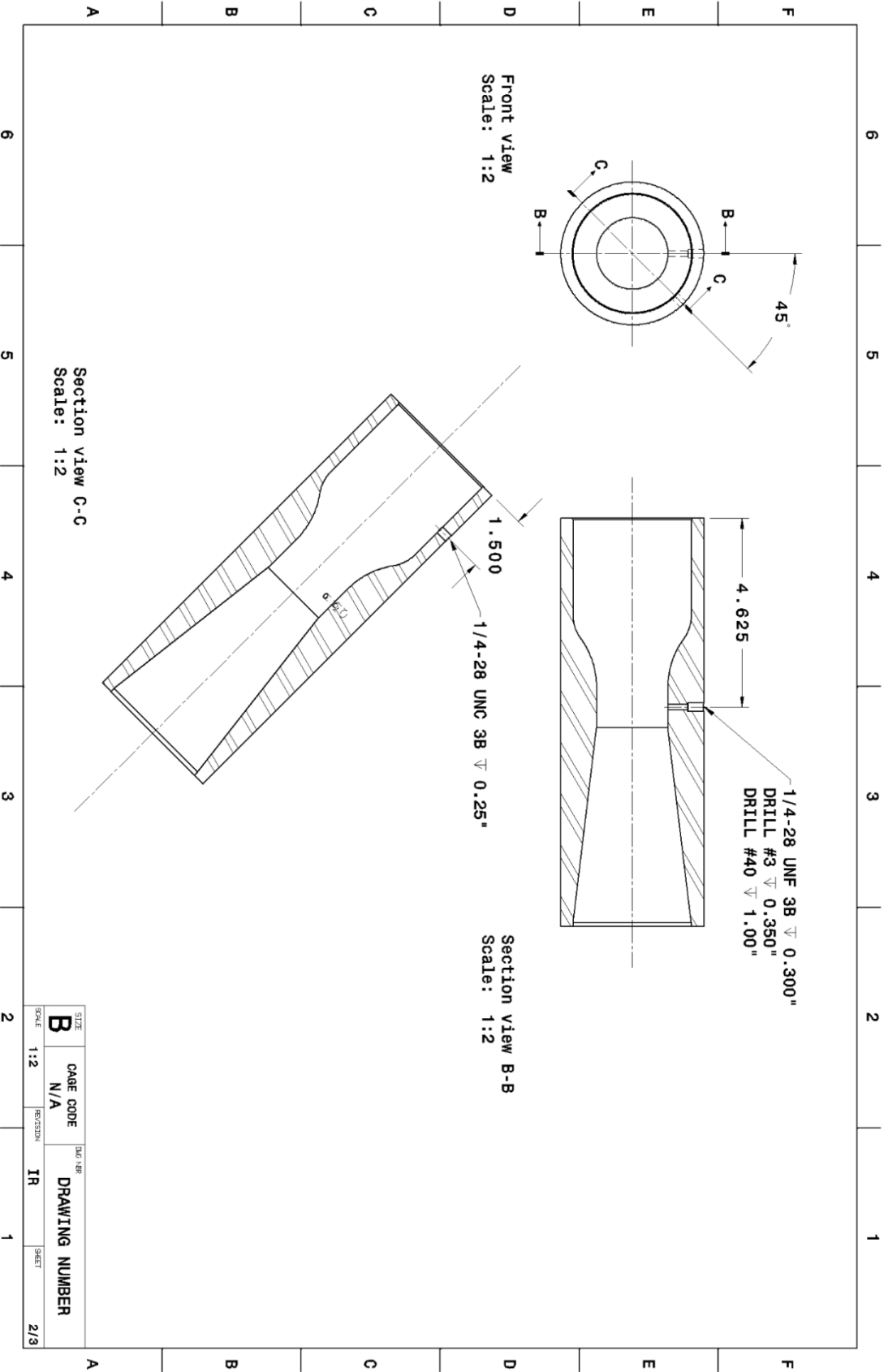
REVISIONS		
REV	DESCRIPTION	DATE
1R		

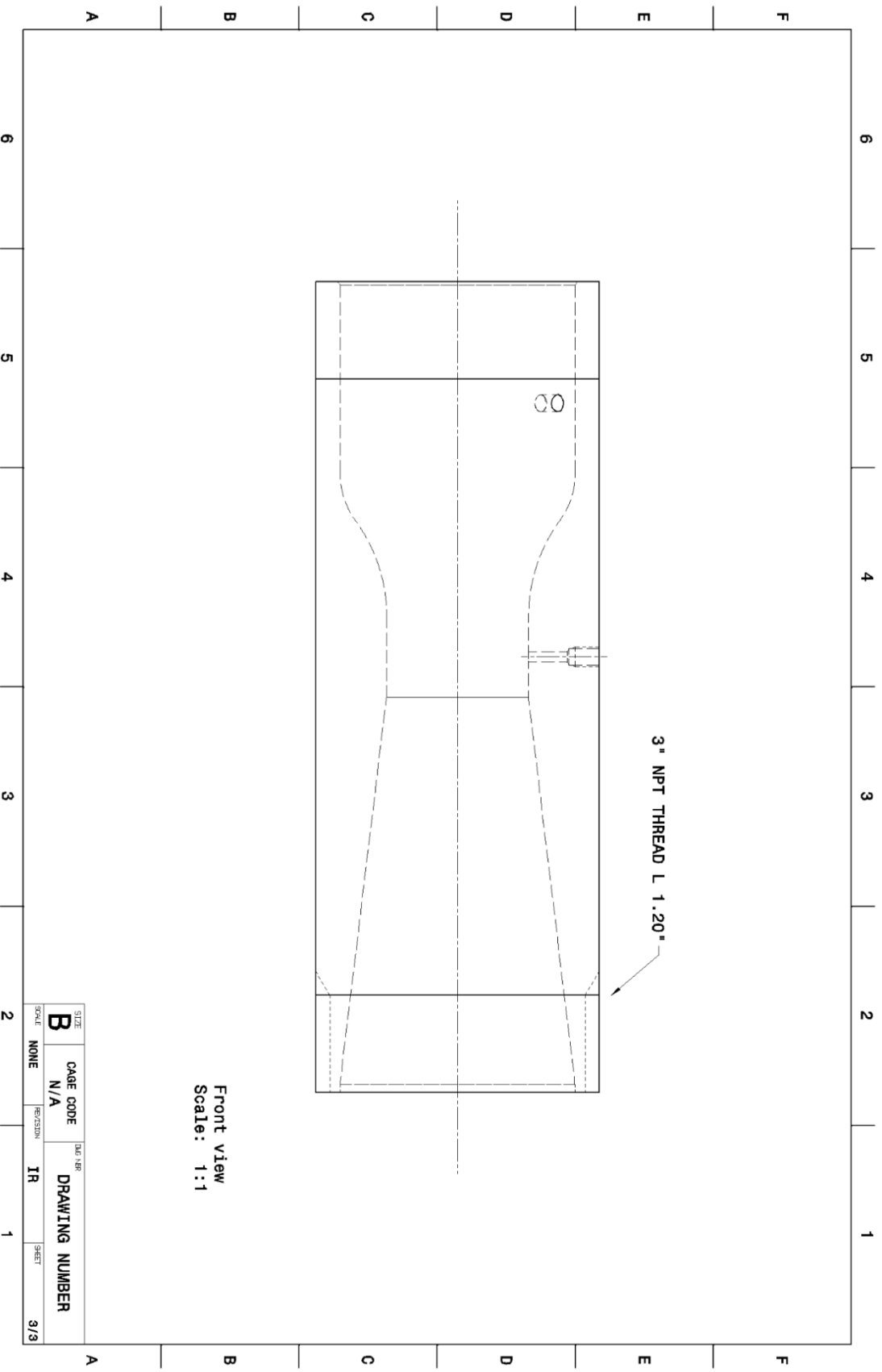
UNLESS OTHERWISE SPECIFIED DIMENSIONS ARE IN INCHES	
DECIMALS	ANGLES
.XX ± 0.01	X° ± 5'
.XXX ± 0.005	X.X° ± 0.5°
DO NOT SCALE DIMENSIONS	
THIRD ANGLE PROJECTION	

DRAWN	JARRETT LOWE	DATE	04 NOV 2016
CHECK	ENGINEER	DATE	
APPROVED	ENGINEER	DATE	
MATERIALS AL 6061 ROUND STOCK O.D. 3.15"			

TITLE		GTL	
VENTURI 3" NPT 1.75" THROAT			
SIZE	CAGE CODE	Dwg 138	
B	N/A	DRAWING NUMBER N/A	

SOLID MODEL:		APPLICATION: CATIA V5R20	
		CATIA MODEL FILE NAMES: N/A	
		CATIA MODEL FILE DATE: N/A	
DESIGNER	N/A	APPROVED	ENGINEER
DATE		DATE	
04 NOV 2016		04 NOV 2016	
SCALE	NONE	REVISION	IR
1/3			



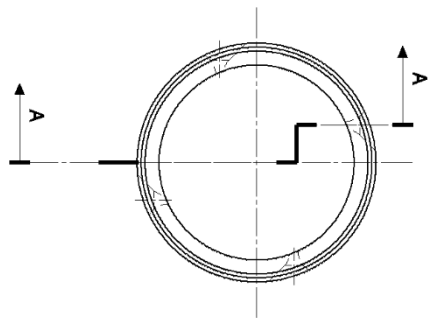


Front view
Scale: 1:1

SIZE	CAGE CODE	DATE	DRAWING NUMBER
B	N/A	IR	9/3
SCALE	REVISION	SHEET	
NONE			

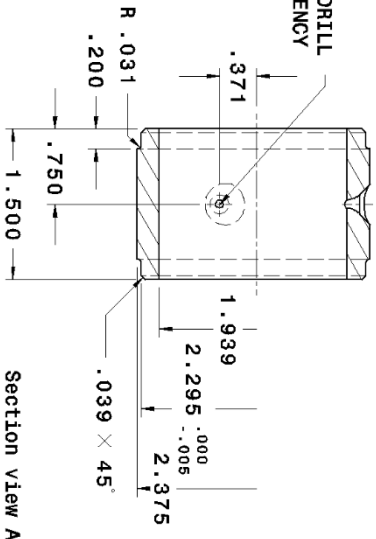
NOTES:

- UNLESS OTHERWISE SPECIFIED:
 - DRAWING INTERPRETED PER ANSI Y14.5M-1994
 - BREAK SHARP EDGES .003 - .008
 - CORNERS TO HAVE FILLETS .005 - .020
 - TOTAL RUNOUT OF ALL DIAMETERS RELATIVE TO A SHALL NOT EXCEED .005
- MATERIAL: SS304 SCH80 2.00" PIPE

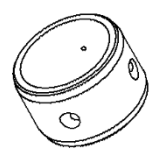


Front view
Scale: 1:1

4 X 5/64-RADIUS CENTERDRILL
90° COUNTERSINK TO TANGENCY



Section view A-A
Scale: 1:1



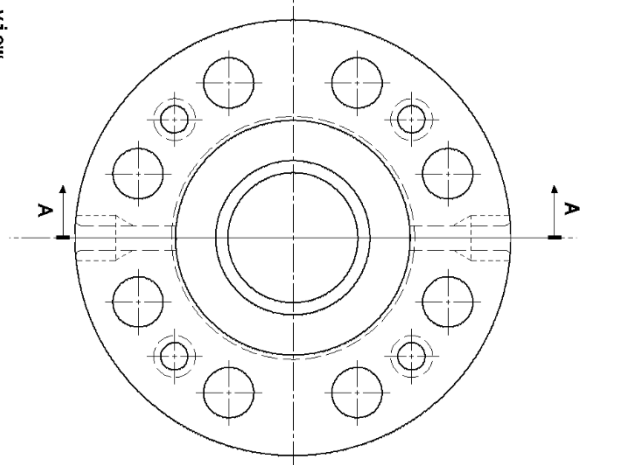
REVISIONS		
REV	DESCRIPTION	DATE
1R		

UNLESS OTHERWISE SPECIFIED DIMENSIONS ARE IN INCHES DECIMALS FRACTIONS TOLERANCES XXX ± 0.01 X.X ± 0.005 DO NOT SCALE DIMENSIONS THIRD ANGLE PROJECTION		DRAWN JARRETT LOWE		DATE 04 NOV 2016
CHECK ENGINEER		APPROVED ENGINEER		DATE 04 NOV 2016
MATERIAL AL 6061 ROUND STOCK O.D. 2.5"		TITLE 4 X PORT ANGLED 22.5° YAWED 90° THROAT Ø 0.081		DATE 04 NOV 2016
DESIGNER N/A		SIZE B		SCALE NONE
APPLICATION: CATIA V5R20 CATIA MODEL FILE NAMES: N/A CATIA MODEL FILE DATE: N/A		CAGE CODE N/A		DRAWING NUMBER N/A
SOLID MODEL:		REV/VERSION IR		SHEET 1/3

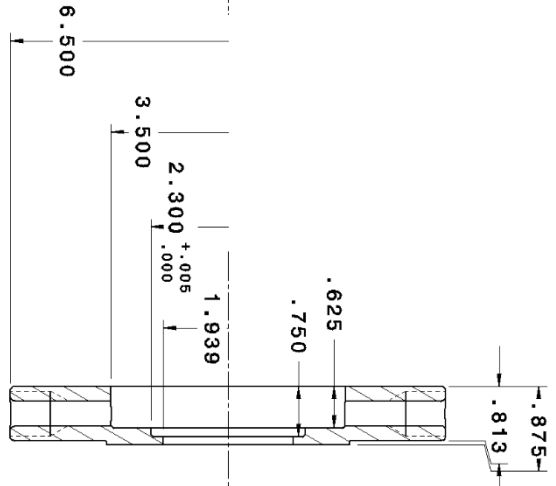
6 5 4 3 2 1

NOTES: 1. UNLESS OTHERWISE SPECIFIED:
 -DRAWING INTERPRETED PER ANSI Y14.5M-1994
 -BREAK SHARP EDGES .003 - .008
 -CORNERS TO HAVE FILLETS .005 - .020
 -TOTAL RUNOUT OF ALL DIAMETERS RELATIVE TO A SHALL NOT EXCEED .005

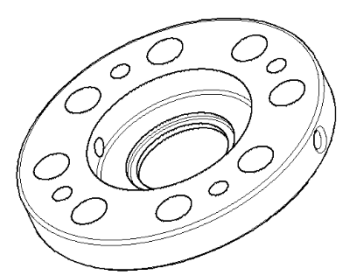
2. MATERIAL: KERKAU A182 F304/304L 2" ANSI 300 86425 B16.5



Front view
 Scale: 2:3



Section view A-A
 Scale: 2:3

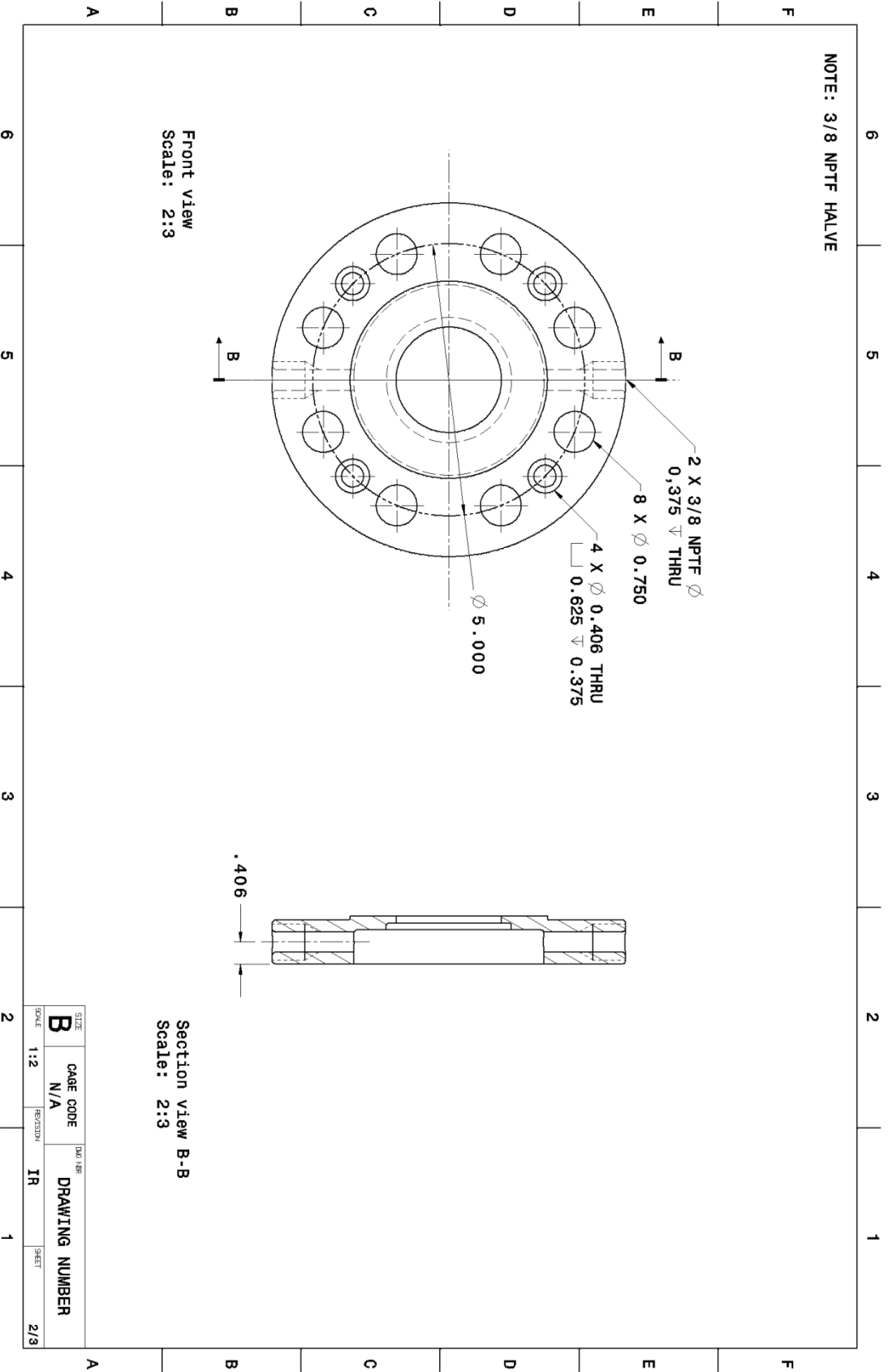


Isometric View
 Scale: 1:2

REVISIONS		
REV	DESCRIPTION	DATE
1R		

SOLID MODEL:		APPLICATION: CATIA V5R20	
		CATIA MODEL FILE NAMES: N/A	
		CATIA MODEL FILE DATE: N/A	
UNLESS OTHERWISE SPECIFIED DIMENSIONS ARE IN INCHES		DRAWN: JARRETT LOWE	
DECIMALS		DATE: 04 NOV 2016	
.005		CHECK: ENGINEER	
.001		DATE: 04 NOV 2016	
.0005		DESIGNED: AL 6061 ROUND STOCK	
.0002		DATE: 04 NOV 2016	
.0001		TITLE: FUEL MANIFOLD HALVES	
.00005		SIZE: B	
.00002		CAGE CODE: N/A	
.00001		DRAWING NUMBER: N/A	
THIRD ANGLE PROJECTION		SCALE: NONE	
APPROVED: ENGINEER		REVISION: IR	
DATE: 04 NOV 2016		SHEET: 1/3	

A 6 5 4 3 2 1



SIZE	CAGE CODE	DAU 188	DRAWING NUMBER
B	N/A		
SCALE	REV/STATION	IR	SHEET
1:2			2/3

